TEM and STEM/EELS Studies of Diamond-Like Carbon (DLC) Films and Diamond Films

Zur Erlangung des akademischen Grades
Doktor der Ingenieurwissenschaften
der Fakultät für Maschinenbau
Karlsruher Institut für Technologie (KIT)

genehmigte
Dissertation
von

M.Eng. Xinyi Zhang

aus
Suzhou (China)

Tag der mündlichen Prüfung: 12. 11. 2014
Hauptreferent: Prof. Dr. Peter Gumbsch
Koreferent: Prof. Dr. Dagmar Gerthsen
Koreferent: Priv.-Doz. Dr. rer. nat. habil. Reinhard Schneider

Abstract

This thesis is concerned with microstructural and chemical investigations of thin layers of diamond and diamond-like carbon (DLC) which were performed by transmission electron microscopy (TEM) in combination with electron energy loss spectroscopy (EELS).

DLC films consist of amorphous carbon (a-C), and are composed of carbon atoms of sp^2- and sp^3-hybridization, denoted as sp^2-C and sp^3-C, respectively, arranged in a random network. The properties of DLC films such as high hardness and wear resistance as well as low coefficient of friction (COF) are mainly related to the ratio between sp^2- and sp^3-hybridized carbon atoms, which is thus of great interest. EELS combined with scanning TEM (STEM) is the only technique that allows quantification of the sp^2/sp^3-ratio by analyzing the energy loss near-edge structure (ELNES) of the C-K ionization edge at high spatial resolution. Therefore, it was applied to determine the fraction of sp^2-hybridized carbon atoms of different DLC films, grown under hydrogen-containing atmosphere (a-C:H) as well as hydrogen-free (ta-C). It could be shown that the sp^2-C fraction of a-C:H material amounts to about 70 %, whereas for ta-C it is 50 %. The DLC films were also utilized to optimize EELS processing and, hence, the accuracy of sp^2-C quantification. Moreover, the damaging influence of focused-ion-beam-based TEM specimen preparation is demonstrated and possibilities for correction are presented, essentially improving the reliability of EELS quantification.

Microcrystalline diamond is the second carbon material studied by STEM/EELS in this work. Diamond can be polished against diamond powder with a surprisingly low COF and a highly anisotropic wear rate. Two mechanisms were suggested as possible origin for the low wear resistance: A phase transformation of crystalline diamond into amorphous carbon and passivation of dangling bonds in a water-containing atmosphere. The direct comparison between unworn and worn diamond regions clearly shows a tribo-induced phase transition from crystalline diamond to amorphous carbon. The fraction of 60 % sp^2-hybridized carbon atoms in the a-C layer agrees well with the theoretical prediction. An interface roughness of ~ 1 nm indicates a crystalline-amorphous phase transformation that is induced by an atom-by-atom process. The abrupt thickness change of the a-C layer on top of grains with different crystallographic orientations demonstrates that the phase transformation process is highly anisotropic.

Zusammenfassung

Die vorliegende Arbeit beschreibt mikrostrukturelle und chemische Untersuchungen dünner Schichten aus Diamant und diamantartigem Kohlenstoff (DLC), welche mit Transmissionselektronenmikroskopie (TEM) in Kombination mit Elektronenenergieverlust-spektroskopie (EELS) durchgeführt wurden.

DLC-Filme bestehen aus amorphem Kohlenstoff und enthalten sp^2- und sp^3-hybridisierte Kohlenstoffatome. Eigenschaften von DLC-Filmen wie hohe Verschleißfestigkeit sowie geringer Reibungskoeffizient sind hauptsächlich korreliert mit dem Verhältnis zwischen sp^2- und sp^3-hybridisierten C-Atomen, das deswegen von großem Interesse ist. EELS kombiniert mit Raster-TEM (STEM) ist die einzige Technik, welche die Quantifizierung des sp^2/sp^3-Verhältnisses anhand der Analyse kantennaher Feinstrukturen (ELNES) der C-K-Ionisationskante mit hoher Ortsauflösung erlaubt. Deswegen wurde sie zur Bestimmung der Anteile von sp^2-hybridierten C-Atomen in unterschiedlichen DLC-Filmen eingesetzt, die unter wasserstoffhaltiger Atmosphäre (a-C:H) und ohne Wasserstoff (ta-C) abgeschieden wurden. Es konnte gezeigt werden, dass der sp^2-C Gehalt von a-C:H etwa 70 % und von ta-C lediglich 50 % beträgt. Auf Basis der DLC-Filme konnte die Aufbereitung von EELS Spektren und damit die Genauigkeit der Bestimmung des sp^2-C Gehaltes optimiert werden. Ebenso wurde die schädigende Wirkung von Ga^+-Ionen bei der TEM Probenpräparation aufgezeigt und die Möglichkeit zu deren Korrektur vorgestellt.

Mikrokristalliner Diamant ist das zweite im Rahmen dieser Arbeit mittels STEM/EELS untersuchte Material. Diamant weist erstaunlich geringe Reibungskoeffizienten sowie ein anisotropes Verschleißverhalten auf. Zwei Mechanismen wurden als mögliche Ursache für diese Eigenschaften vorgeschlagen: ein Phasenübergang von kristallinem Diamant zu amorphem Kohlenstoff und die Passivierung freier Bindungen unter wasserhaltiger Atmosphäre. Der direkte Vergleich unbelastetem und tribologisch belastetem Diamant zeigt klar einen tribologisch induzierten Phasenübergang von kristallinem Diamant zu a-C. Der Anteil von sp^2-C in der a-C Schicht beträgt 60 % in Übereinstimmung mit der theoretischen Vorhersage. Die Rauigkeit an Grenzfläche zwischen Diamant und der a-C Schicht von nur etwa 1 nm deutet auf einen atomaren Prozess bei der Phasenumwandlung hin. Die Anisotropie des Phasenübergangs erschließt sich aus der abrupten Dickenänderung der a-C Schicht auf Körnern mit unterschiedlicher kristallographischer Orientierung.

Contents

Acronyms

BF	bright field
BFP	back-focal-plane
COF	coefficient of friction
CVD	chemical vapor deposition
DC	direct current
DDSCS	double differential scattering cross-section
DF	dark field
DIBS	dual-ion beam sputtering
DLC	diamond-like carbon
DOS	density of states
EDXS	energy-dispersive X-ray spectroscopy
EELS	electron energy loss spectroscopy
ELNES	energy loss near-edge fine structure
EXAFS	extended X-ray absorption fine structure
FCVA	filtered cathodic vacuum arc
FEG	field emission gun
FFT	fast Fourier transformation
FIB	focused ion beam
FT-IR	Fourier-transform infrared spectroscopy
FWHM	full width at half maximum
GIF	GATAN imaging energy filter
GOS	generalized oscillator strength
HAADF	high-angle annular dark-field
HOPG	highly ordered pyrolytic graphite
HPHT	high pressure and high temperature
HWHM	half width at half maximum
IBAM	ion-beam-assisted magnetron

MAC	magic angle condition
MAEELS	Magic angle electron energy loss spectroscopy
MAS-NMR	magic-angle spinning nuclear magnetic resonance
MCD	microcrystalline diamond
MSIB	mass-selected ion beam
MW	microwave
NCD	nanocrystalline diamond
NEXAFS	near-edge X-ray absorption fine structure spectroscopy
NMR	nuclear magnetic resonance
NRA	nuclear reaction analysis
PACVD	plasma-assisted chemical vapor deposition
PECVD	plasma-enhanced chemical vapor deposition
PLD	pulsed-laser deposition
PVD	physical vapor deposition
RF	radio frequency
SAED	selected-area electron diffraction
SEM	scanning electron microscopy
STEM	scanning transmission electron microscopy
TEM	transmission electron microscopy
ToF-SIMS	time-of-flight secondary-ion mass spectrometry
UNCD	ultra-nanocrystalline diamond
XANES	X-ray absorption near edge structure
XAS	X-ray absorption spectroscopy
XPS	X-ray photoelectron spectroscopy
ZA	zone axis
ZLP	zero-loss peak

Symbols

A	constant
α	convergence semi-angle
a-C	amorphous carbon
a-C:H	hydrogenated amorphous carbon
Ar	argon
B	boron
β	collection semi-angle
C	carbon
c	speed of light
$c_{A,\ B}$	concentration of constitute (A, B) in the material
ΔE	integration window
E	energy loss
E_0	energy of incident electron
E_c	critical excitation energy of the single core electron
$E_{i,\ i+1,\ intial,\ final}$	energy of states
E_m	mean energy loss
E_{PL}	maximum energy loss of the plasmon peak
f	final state function
$f\,(E,\ q)$	generalized oscillator strength
γ	relativistic factor
Ga	gallium
h	Planck's constant
$I_{(\mathrm{a,\ b},\ \pi^*,\ \sigma^*,\ \Delta \mathrm{E})}$	integrated intensity (of a certain portion of an EELS spectrum)
i	initial state function
I-ratio	intensity ratio
I_0	integrated intensity of the zero-loss peak

$I_{1,...,n}$	integrated intensity of the 1st, ..., nth plasmon peak
I_B	background intensity
$I_{\Delta E}$	integrated intensity over the integration energy window ΔE
I_{π^*}	integrated intensity of the π^* peak
I_{σ^*}	integrated intensity of the σ^* peak
I_{total}	total intensity accepted by the spectrometer
$\boldsymbol{k}$	primary momentum of an incident electron
$\boldsymbol{k'}$	transmitted momentum of an incident electron
k, k', k''	partial cross-section ratio
λ	plasmon mean free path
$M(E)$	matrix element
m_e	electron rest mass
N	nitrogen
N	number of particles
n	number of plasmon
$n_{a,b}$	anti-bonding orbital density of components a and b
$N(E)$	density of states function
π	π atomic orbital
π^*	π^* anti-bonding orbital
	transitions from 1*s* oribitals to anti-bonding π orbitals
$\boldsymbol{q}$	momentum transfer of an incident electron
θ_E	characteristic scattering angle
R	intensity ratio or sp^2 %
$\boldsymbol{r}$	position coordinates of the atomic electrons
r	constant
R_b	intensity ratio or sp^2 % for sample bulk
R_d	intensity ratio or sp^2 % for FIB induced damaged layer
$\sigma_{(a,b)}$	inelastic scattering cross-section (of a certain type of excitation)
σ	σ atomic orbital
σ^*	σ^* anti-bonding orbital
	transitions from 1*s* oribitals to anti-bonding σ orbitals
sp^2 %	atomic fraction of sp^2-hybridized carbon atoms

sp^2-C	sp^2-hybridized carbon atoms
sp^3 %	atomic fraction of sp^3-hybridized carbon atoms
sp^3-C	sp^3-hybridized carbon atoms
T	sample thickness or relative thickness
t	sample thickness
ta-C	tetrahedral amorphous carbon
T_b	thickness or relative thickness for sample bulk
T_d	thickness or relative thickness for FIB induced damaged layer
Ω	solid angle
ω_p	plasma frequency
x	complex factors in equations
Z	atomic number

1 Introduction

Thin layers of diamond and diamond-like carbon (DLC) films have become a limelight in many fields in industry due to their valuable properties.

DLC films are basically amorphous carbon, and thus they are composed of carbon atoms of both sp^2- and sp^3-hybridizations arranged in a random network. As an intuitive comprehension, the properties of DLC films could be a combination of those of graphite (purely sp^2-hybridized) and diamond (purely sp^3-hybridized). DLC films with a high sp^2-content could be rather graphitic, whereas the properties of sp^3-rich DLC films could approach to those of diamond. Hydrogen and other doping materials are often intentionally contained in some DLC films, and can exert a strong influence on the DLC's properties. The controllable high hardness/wear resistance and low coefficient of friction (COF) make DLC films promising as tribological coatings and it is hence of great interest to study the bonding configuration, i.e., the ratio between sp^2- and sp^3-hybridized carbon atoms in the different DLC films. Furthermore, since quantification of the sp^2/sp^3-ratio is preferred to be done at high spatial resolution, dedicated electron-microscopical techniques are needed for further in-depth studies.

Diamond is an attractive material and displays many extreme properties, such as the highest hardness, Young's modulus, and thermal conductivity. Despite being at the limit of mechanical properties, diamond crystals can be machined by polishing against diamond powder, which is a technique well established centuries ago. The mechanism behind this process has long been debated, whereupon the transformation of the hard crystalline diamond surface into a soft amorphous phase, atmospheric effects, and the cleavage of small pieces of crystalline diamond are considered. Moreover, it is surprising that the wear rate of diamond is highly anisotropic. That is to say that there are so-called hard and soft directions on a specific diamond crystallographic surface, in which the diamond can be polished with different wear rates. This anisotropic wear of diamond is an important aspect that needs to be explained in the study of diamond wear mechanisms. Moreover, diamond films can also be used as a tribological coating yielding a low COF, which has been attributed to either a crystal/amorphous phase transformation or a passivation of surface dangling bonds by H/OH atoms or groups in an ambient atmosphere. In order to study the friction and wear of diamond, it is desired to gain a nanometer-scale insight by direct comparison between unworn and worn diamond regions.

For such an insight even down to the atomic scale, transmission electron microscopy (TEM) in combination with techniques for chemical analyses can generally be applied. Such imaging techniques, like conventional and high-resolution TEM, enable microstructural analyses of materials, whereas their crystal structure can directly be characterized by different methods of electron diffraction. In state-of-the-art instruments even atomic resolution can be obtained during chemical analyses in the scanning TEM (STEM) mode with an extremely fine electron probe focused on the specimen. (see, e.g., Browning et al. (2012); Pennycook and Jesson (1991)) Analytical techniques such as energy-dispersive X-ray spectroscopy (EDXS) and electron energy loss spectroscopy (EELS) can easily be combined with STEM. The accessibility of TEM has been further improved by the advanced focused-ion-beam (FIB) method, which assists TEM sample preparation and enables the selection of a specific site of a specimen for subsequent TEM/STEM investigation.

Like EDXS, EELS carried out in a transmission electron microscope is a technique capable to analyze the chemical composition of the analyzed specimen volume at high spatial resolution, but is the only method to also elucidate the electronic structure and chemical bonding of the detected elements. In general, EELS measures the energy-loss distribution of the inelastically scattered electrons. Those electrons which encounter inelastic scattering events, can lose characteristic energies and meanwhile excite electrons of the atoms of the solid matter to higher energy states. Thereby, specific plasmon signals in the low-loss region (0 – 50 eV) and characteristic ionization edges at higher losses (typically above 50 eV and higher) are generated in EELS spectra that can be utilized to identify and quantify elements in the sample. Furthermore, EELS is essentially sensitive to light elements such as, e.g., carbon because the so-called ionization cross-section, being the most important parameter for describing the inelastic scattering probability, increases with decreasing atomic number. Moreover, due to the high energy resolution of the order of 1 eV and better, fine structures of ionization edges, particularly in the energy range between the ionization threshold energy and approximately 30 eV beyond, can be seen in EELS spectra and give spatially resolved information about the specific chemical bonding. These energy loss near-edge fine structures (ELNES) are attributed to excitations of inner-shell electrons into unoccupied states of the conduction band. In the literature, a huge number of examples of chemical-bond analyses through ELNES studies can be found, where in many cases they were performed by recording of ELNES details of a characteristic ionization edge from reference materials and using them in a fingerprint manner for analyzing the bonding character of that element in the unknown compound (see, e.g., Bouchet and Colliex (2003); Brydson et al. (1991); Diociaiuti (2005); Gass et al. (2010); Mao et al. (2014); Schmid (1995)).

For carbon modifications, usually transitions from 1*s* to π^* and 1*s* to σ^* states can be well resolved in the C-K ELNES, also allowing the quantification of the sp^2/sp^3-ratio. From this point of view, diamond-like carbon is a perfect candidate to apply ELNES studies for quantification of the sp^2/sp^3-ratio. In this context, thin DLC films are also suited to demonstrate the applicability of that EELS quantification technique and to find means for improving its accuracy.

Although EELS offers hints of the H-content within carbon layers as energy-loss intensities between the π^* and σ^* ionization edges (Fink et al., 1983; Silvaf et al., 1996), at present H-quantification by EELS is not possible for several reasons. Firstly, the accurate assignment of the energy-loss signals in this region, which could also be superimposed on the higher-lying shoulder of the π^* resonance or molecular transitions, is unclear, (Batson, 1993; Browning et al., 1991; Papworth et al., 2000; Pickard et al., 1995; Titantah & Lamoen, 2005). Secondly, some minor absorption maxima between the π^* and σ^* signals could only be detected occasionally (Fink et al., 1983) and in most cases they are invisible for EELS because of the electron-radiation damage and the limited energy resolution, being poorer than the width of those minor excitations. However, according to equivalent X-ray absorption spectroscopy (XAS) data, corresponding near-edge X-ray absorption fine structure spectroscopy (NEXAFS), also known as X-ray absorption near-edge fine structures (XANES) can show detailed features between 286 eV and 289 eV attributable to C-H bonds (Alexander et al., 2008; Bressler et al., 1997; Buijnsters et al., 2009). Nevertheless, a full knowledge of various C-H bonding excitation cross-sections is still lacking, which complicates corresponding analyses.

The present thesis reports on results of microstructural and microchemical investigations of diamond-like carbon (DLC) and diamond films, which were deposited on steel substrates by plasma-enhanced chemical vapor deposition (PECVD) (known also as plasma-assisted chemical vapor deposition, abbreviated as PACVD). Ring elements made of such DLC/diamond-steel material systems are used as wear-resistant construction components in mechanical devices, showing quite different friction and wear properties in dependence on the specific parameters for film growth as well as mechanical load and environment during testing. From this point of view, combined TEM and STEM/EELS studies are well suited to get a deeper insight into structural and chemical bonding phenomena of the analyzed DLC/diamond films. In this context, not only the applicability of STEM/EELS should be proved, but also its accuracy in the quantification of the sp^2/sp^3-C ratio of the PECVD-deposited carbon films.

Accordingly, this work contains six chapters with the following contents. After this introduction, a brief overview is given in chapter 2 regarding the element carbon and the three carbon materials considered in this work, including DLC films, diamond films, and graphite. Among them, the DLC and diamond films are in focus of the subsequently reported TEM and STEM/EELS observations, where graphite is used as a reference for ELNES quantification of sp^2/sp^3-C. Chapter 3 describes the fundamentals and our experimental optimizations of the TEM-related techniques (including TEM sample preparation), TEM, STEM, and EELS. The structural and chemical properties of two types of DLC films, which are characterized by TEM and EELS, are described in detail in chapter 4. Most importantly, practical aspects of ELNES quantification of the sp^2/sp^3-ratio are discussed in the course of these studies. Chapter 5 deals with the tribology of diamond films. Unworn and worn diamond films are directly compared with respect to their microstructural and microchemical properties by electron-microscopic techniques and discussed with respect to diamond wear mechanisms in literature. Here, detailed STEM/EELS analyses document their efficiency for identifying local changes of the chemical-bond character of carbon-based materials. The obtained findings are applied to establish a model which describes some wear mechanisms of diamond. A short summary of typical experimental data and of corresponding information obtained for both the DLC and diamond films is presented in chapter 6.

2 Diamond-like carbon, diamond, and graphite

2.1 The element carbon

The element carbon is widely distributed in numerous forms in nature and in man-made products. Its capability of bonding with many elements, including itself, in different manners makes carbon an extraordinary element. For example, there are nearly ten million carbon-based compounds in organic chemistry. In particular, two carbon allotropes can be found in nature, namely diamond and graphite, showing significantly different properties. More carbon allotropes have been created in the laboratory, for example C_{20}, C_{60}, carbon nanotubes, and carbon-onion particles, known as members of the fullerene family. Recently, carbon nanofoam has been produced, which is unexpectedly magnetic (Rode et al., 2004). Graphene, being a single layer of carbon atoms, is the two-dimensional (2D) material, which is amazingly both an object for the study of relativistic quantum mechanics and a material with promising application in the macroworld (Geim & Novoselov, 2007). Nevertheless, there are even more carbon allotropes that have been predicted in theory, but waiting to get realized. For instance, a number of crystalline carbon allotropes predicted by *ab initio* calculations were reviewed by Wu et al. (2012). In the case of amorphous carbon phases, DLC films are of great interest in scientific research and have already opened up a huge number of industrial applications.

A carbon atom has six electrons. The electron configuration of a single carbon atom, i.e. a carbon atom in ground state, is $1s^2 2s^2 2p^2$. The s orbitals ($1s$ and $2s$) are spherical and non-directional, whereas the $2p$ orbital is 8-shaped and symmetrical about its axis according to wave-function calculations. This configuration with only two electrons available to form covalent bonds is altered when the carbon atom is bonded with other atoms. Since the energy difference between the $2s$ orbital and the $2p$ orbital is small, one of the two electrons in the $2s$ orbital can be readily excited to the $2p$ orbital. Based on this excitation process, which essentially provides the carbon atom with four unpaired electrons, there are three forms of atomic hybrid configurations for carbon to bond with other atoms: sp^3-, sp^2- and sp-hybridization.

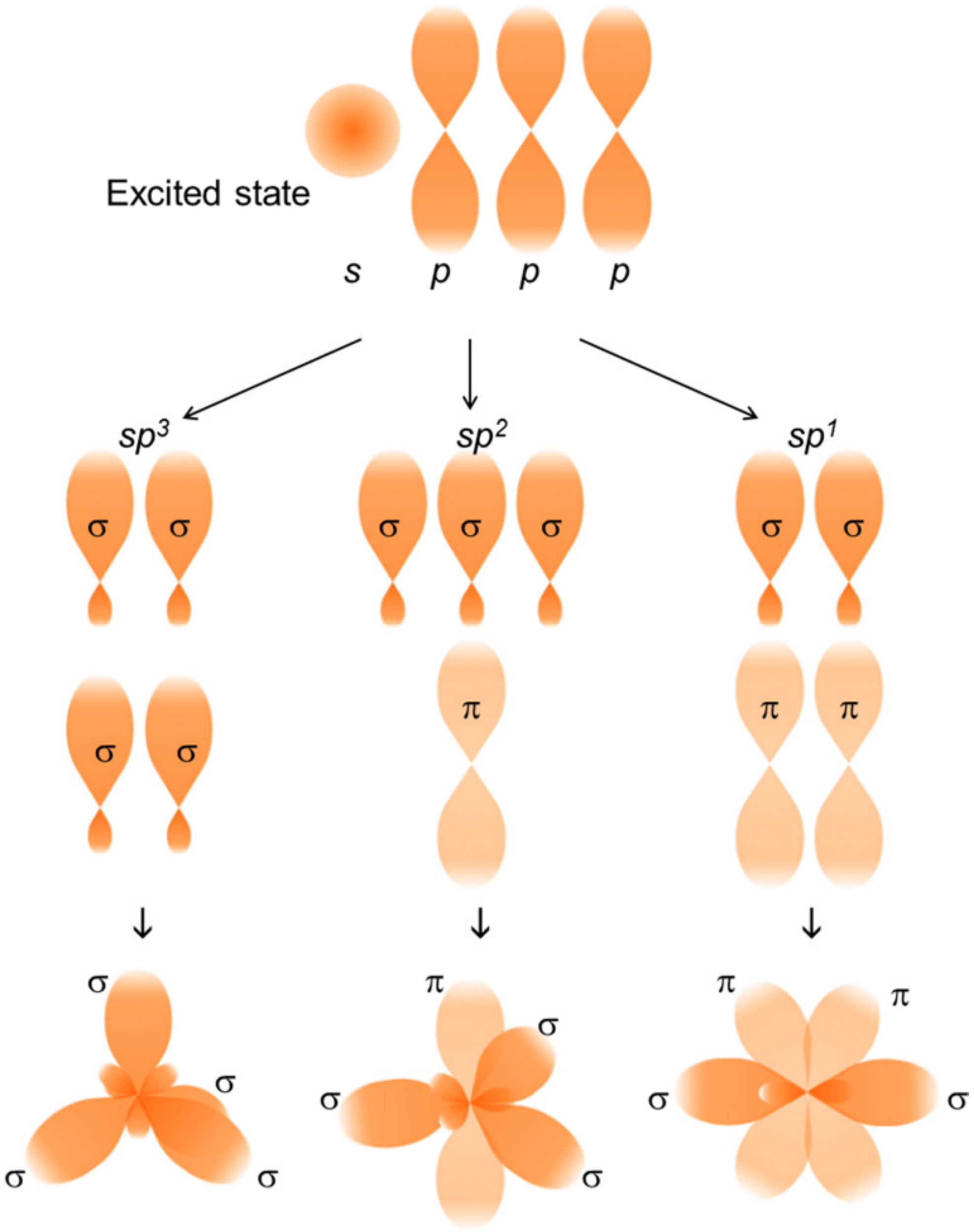

Fig. 2.1.1 A schematic drawing of the orbitals in *sp*^{3}-, *sp*^{2}-, and *sp*-hybridization, respectively, for carbon.

Fig. 2.1.1 is a schematic drawing showing the formation of the three forms of hybridizations from an imaginary excited state, the complexity in the shapes of 2*s* and 2*p* orbitals in carbon is largely omitted. By *sp*^{3}-hybridization, the *s* orbital and the three *p* orbitals are hybridized into four identical σ orbitals, where each of them is concentrated on one side and has a small portion on the opposite side. These four σ orbitals of equivalent energy can form four σ bonds with a tetrahedral symmetry, when they undergo end-on overlaps with orbitals of other atoms. The sp^2-hybridization forms three σ orbitals with a trigonal in-plane geometry by mixing of the 2*s* orbital and two of the 2*p* orbitals, leaving one unchanged 2*p* orbital perpendicular to the plane. The three equivalent σ orbitals are ready to form three σ bonds with other atoms and the 2*p* orbital can make a π bond. As only one 2*s* orbital and one 2*p* orbital are mixed to form two σ bonds in line and two π bonds with other atoms, it is called the *sp*-hybridization, which can be found, e.g., in acetylene and polyacetylene.

sp^3-hybridized C-atoms (sp^3-C) are the basis of diamond, while graphite and the fullerene family consist essentially of sp^2-hybridized C-atoms (sp^2-C). Diamond is the hardest material and carbon nanotubes are the strongest fibers, whereas graphite is very soft due to the weak interlayer bonding forces, van der waals forces, which hold the layers together. In the case of DLC, which contains both sp^2-C and sp^3-C in the amorphous structure, it is appealing to find the desired performance for different applications by controlling its specific configuration.

2.2 Diamond-like carbon

2.2.1 Structure

Fig. 2.2.1 shows the famous phase diagram of the amorphous carbon-hydrogen system, in which DLCs are classified as a function of the ratio of sp^2/sp^3-hybridized carbon as well as the content of H. Amorphous carbon films are commonly abbreviated as “a-C” films, whereas carbon films with predominant sp^3-hybridization of tetrahedral configuration are denoted as “ta-C” films, being representatives of “tetrahedral amorphous carbon” films. According to the phase diagram of Fig. 2.2.1, DLCs with more than 50 % of sp^3-C can be regarded as ta-C. For DLCs containing additional elements, e.g., H, Ar, and other non-metallic/metallic modifying elements, the abbreviation can be followed by a colon and the symbol of the element, for example, ta-C:H, meaning hydrogenated tetrahedral amorphous carbon. On the one hand, a trace amount of hydrogen, typically 3 atom %, can still be incorporated in the films even for DLCs intended to be free of H, possibly due to the residual gases in the deposition chamber. But on the other hand, there are also carbon films with an artificially produced high hydrogen content in the range of 40 – 60 atom %. Such a-C:H films are called polymeric and in that case the carbon atoms are largely linked in a chain formation with cross-links between the chains. Nevertheless, there are no clear boundaries or definitions between DLCs of different types.

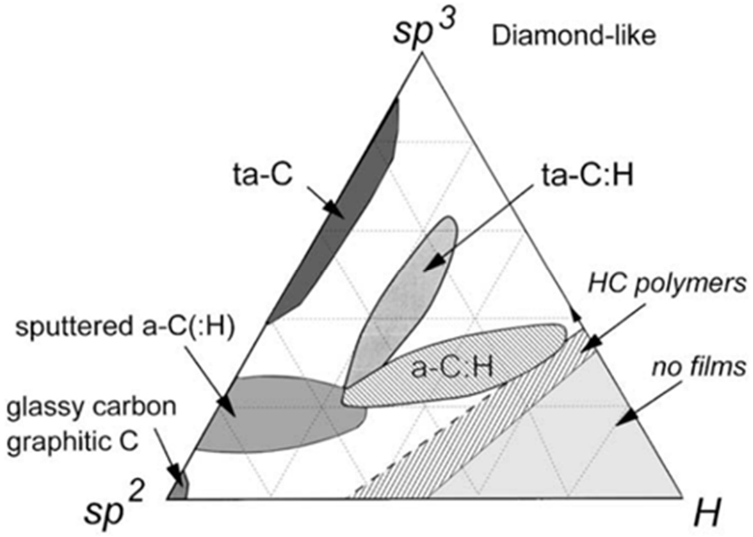

Fig. 2.2.1 Ternary phase diagram of chemical bonding in the amorphous C-H system (Robertson, 2002)

2.2.2 Properties and applications

The properties of DLCs are strongly related to the ternary phase diagram given above. It has been reported that in general, as the content of sp^3-C increases, mechanical, chemical, electrical, and optical properties of the film could all show a trend from these of graphite to those of diamond. The role of H-content is also important but more complicated. It is quite natural that H degrades the density and hardness of DLC films, which is just the opposite effect relative to sp^3-hybridized C-C bonds. However, hydrogen can effectively stabilize the sp^3-sites. It has been found that in a-C:H, all sp^3-sites are hydrogenated and many sp^2-sites are not, meaning that more sp^3-hybridized carbon atoms will be accompanied by more H in the film (Donnet et al., 1999; Tamor et al., 1991). Table 2.1 lists typical properties of a variety of DLCs and compares them to those of diamond and graphite. The ta-C film rich in sp^3-bonds and free of H is close to diamond in density and hardness. With similar content of H, ta-C:H and a-C:H (1) films, the former shows higher density and hardness than the latter, corresponding to a higher sp^3-content. However, for the two a-C:H films, i.e. (1) and (2), the one with higher sp^3-content, namely the film a-C:H(2), is softer and less dense, resulting from its higher H-content.

Table 2.1 Comparison of structure and properties of typical DLCs to those of diamond and graphite, after Robertson (2002).

	sp^3 (%)	H (%)	Density (g/cm^3)	Hardness (GPa)	Reference
Diamond	100	0	3.515	100	(Field, 1993)
ta-C	80 – 88	0	3.1	80	(Fallon et al., 1993; McKenzie, 1996; Pharr et al., 1996)
ta-C:H	70	30	2.4	50	(Weiler et al., 1996)
a-C:H(1)	40	30 – 40	1.6 – 2.2	10 – 20	(Koidl et al., 1990)
a-C:H(2)	60	40 – 50	1.2 – 1.6	<10	(Koidl et al., 1990)
Graphite	0	0	2.267		(Kelly, 1981)

A brief overview of DLCs' tribological properties related to their crystal structure as well as other extrinsic aspects is as follows.

DLC has shown very good performance as a tribo-coating in various applications and has been studied extensively in laboratory. The friction and wear properties of DLCs are not only controlled by materials properties themselves, but are also affected by the tribological conditions, e.g. substrate, counterpart, type of contact, contact pressure, velocity, temperature, and environment.

Generally, all DLCs have the advantage of a low COF, which ranges from 10^{-2} to 10^{-1}, primarily due to their amorphous structure and closely related to the sp^2-fractions. With regards to the wear rate, DLCs with a high sp^3-content can possess an extremely low wear rate. In addition, many researchers have observed that hydrogen is responsible for the low friction of DLC under inert or vacuum conditions (Miyake et al., 1987; Yun et al., 1997; Zaidi et al., 1994). In order to study the role of hydrogen in tribological properties, a series of DLCs was designed by Erdemir et al. (1999) to contain increasing H-content by varying the H/C ratio of the source gas from 1 to 4, i.e. acetylene, ethylene, ethane and methane, but keeping other parameters of preparation and tribo-testing largely constant. As a result, reductions in COF and in wear rate were clearly demonstrated and the best

COF (0.014) was achieved with a DLC film derived from pure methane. It was shown that the COF can be improved by introducing 50 % H_2 in the methane (Erdemir et al., 1999). However, the observed evolution cannot be fully associated with the hydrogen content in the film. The Raman study of a related work showed that the DLCs were more graphitic as the H_2 increased in the gas mixture (Erdemir et al., 2000). Therefore, the tribological performance is believed to be intrinsically related to the combined effect of both the fractions of H and the sp^2-hybridized carbon atoms in the DLC films.

The environment is one of the most crucial extrinsic factors for the tribological properties of DLC, which affects the tribochemical conditions. For a-C:H, low COFs have been frequently observed in vacuum or inert gas environments, while in ambient atmosphere with the presence of oxygen and water vapor, the COFs were generally higher (Enke et al., 1980; Gangopadhyay et al., 1994). Donnet et al. (1998) studied the respective influence of oxygen and water vapor on the DLC tribology. By a progressive introduction of water vapor / oxygen into the ultrahigh vacuum (UHV) tribometer, the steady-state COF was recorded. It was found that a relative humidity above 2 % could drastically increase the COF from below 0.01 to ~ 0.1, while oxygen showed hardly any influence. For ta-C or ta-C:H, the behavior is different. It has been reported that the COF is larger in vacuum, but decreasing in humid environment (Racine et al., 2001; Voevodin et al., 1996).

By some researchers the mechanism behind the low COF of DLCs was attributed to the passivation of the film surface by the H incorporated inside the film or H-/OH-containing molecules in the environment. Alternatively, based on the finding of a transfer film or an sp^2-rich structure at the surface of the DLC after tribo-testings, a tribo-induced sp^3–sp^2 phase transition has been regarded as the main reason for the low COF. By looking into the running-in behavior of DLC, which is a rapid decrease of the COF during the first stage of tribo-testing, Pastewka et al. (2008) observed the sp^3–sp^2 phase transition in both the experimental work and the molecular dynamics simulation.

Since DLCs outstand in their friction and wear performance, combining their good chemical resistance and electrical insulation, they are nowadays widely used as tribo-coatings, e.g., in engine parts and cutting tools in traditional industry. In the field of space technology and storage media (Schlatter, 2002), where liquid lubricants are not possible, DLC coatings that are self-lubricating are of great interest. Biological applications as implantation parts as, e.g., orthopedic joints have been developed (Hauert, 2004; Sheeja et al., 2001).

2.2.3 Deposition and analysis techniques

Ion-beam deposition was the technique that produced the first DLC film (Aisenberg, 1971), whose optical and electrical properties were measured to be close to that of diamond. For example, it was their transparency and high resistivity, thus leading to the name, i.e. diamond-like carbon. Further microstructure analyses by X-ray and electron beam diffraction confirmed the containing of sp^3-hybridized carbon in a similarly deposited DLC (Spencer et al., 1976). In the past decades, besides ion-beam deposition, a variety of techniques have been developed to produce DLCs, such as mass-selected ion beam (MSIB), sputtering, cathodic arc, pulsed-laser deposition (PLD), and chemical vapor deposition (CVD). CVD is recently the most developed laboratory technique with wide options to activate the carbon-containing precursor gas by dissociation and ionization, leading to the gas phase reactions and finally the film deposition onto a substrate. Some popular activation methods in CVD involve hot filament or plasma (PECVD) driven by direct current (DC), radio frequency (RF), or microwave (MW) (Thornton, 1983).

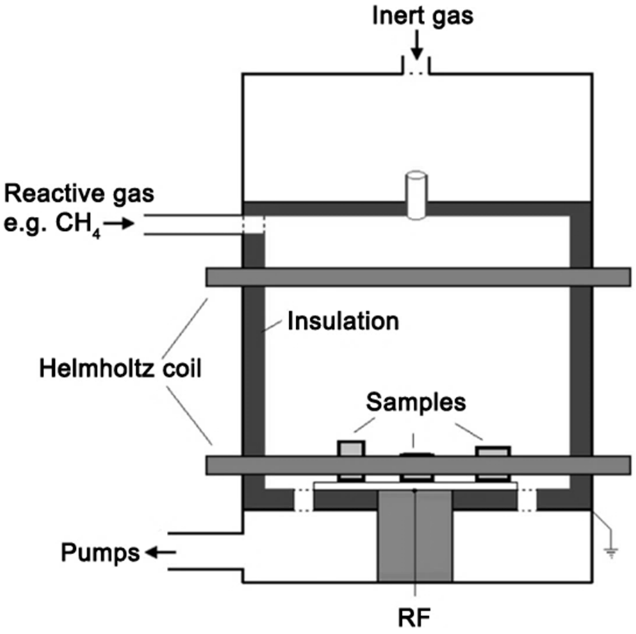

Fig. 2.2.2 Scheme of a RF-PECVD apparatus with a novel reactor design with extendable usable volume, after Meier et al. (2007).

A PECVD chamber is normally configured with a cathode plate and an anode plate, with the substrate attached to the cathode to maximize the ion bombardment. A plasma is created between the two electrodes. Gaseous hydrocarbon mixed with inert gas is commonly used as precursor. Fig. 2.2.2 shows a RF-PECVD apparatus designed by Meier et al. (2007), where the chamber is divided into two parts: one for the inert gas (the upper part) and the other for the reactive gas (the lower part) with a connection in between. The surface of the inert gas sub-chamber is earthed and serves as the counter electrode, while the walls of the reactive gas sub-chamber are made of an insulator and the substrate is the only active electrode. With this design, the active gas is not only barricaded to diffuse into the upper chamber wall, but also significantly reduces the deposition on the insulating wall of the lower chamber. The Helmholtz coils further inhibit the contamination of the floating walls in the reactive gas chamber. As a result, the cleanliness of the rig is improved and the deposition process is more efficient and reliable.

The particular film structure is closely related to the energy of the species impacting onto the substrate. With impact energy too low to sufficiently decompose the carbonaceous gas source, $=CH_2$ groups are predominant in the films. The C-C sp^3-bonds reach a maximum at intermediate energy and decrease as the energy gets higher due to the preferential formation of graphite-like C with disordered sp^2-like bonds (A. Erdemir, Donnet, C., 2001). A number of parameters can play a role on the impact energy, for example the power of the plasma, the gas pressure, the fraction of the inert gas, and the bias-voltage of the substrate, which could be indirectly controlled by other parameters in some apparatus. The H-content, another key parameter for DLC, is possibly affected by the C/H ratio in the source precursor (A. Erdemir, 2001; Erdemir et al., 1999).

Hydrogen-free tetrahedral amorphous carbon (ta-C) films are of high interest because of their high content of sp^3-hybridized C-atoms, resulting in properties more close to those of diamond. The preparation of ta-C films generally involves either energetic C^+-ions in an ion/plasma beam or C-atoms bombarded by other energetic ion species (Schwan et al., 1996). Techniques such as the MSIB (Lifshitz, 1996) and filtered cathodic vacuum arc (FCVA) (Fallon et al., 1993) are usually attributed to the former mechanism, where the energy of the C^+-ions is a key parameter for the properties of ta-C. For example, Fallon et al. (1993) studied the dependence of the fraction of sp^3-C and other properties such as density and compressive stress on the C^+-ion energy in FCVA and found the most diamond-like properties at about 140 eV. During the film growth, incident C^+-ions are implanted into the surface atomic layer and lead to a locally increased higher density. Without the use of C^+-ions, dual-ion beam sputtering (DIBS) and ion-beam-assisted magnetron (IBAM) are also able to produce ta-C (Rossi et al., 1995), where the energy is carried by Ar^+- or Xe^+-ions.

Various analytical techniques are utilized to determine the sp^2/sp^3-ratio of carbon allotropes. Raman spectroscopy, NEXAFS, and EELS are commonly used for this purpose. Combined with TEM, EELS is able to analyze the sp^2/sp^3-ratio of a specific small region in the DLC film. Hydrogen is a difficult element to be measured with high enough accuracy, and effective methods like, e.g., nuclear reaction analysis (NRA) and nuclear magnetic resonance (NMR) usually involve special nuclear or proton facilities with corresponding large efforts. Fourier-transform infrared spectroscopy (FT-IR), NEXAFS, and EELS are the few techniques available to analyze C-H bonds, yet the assignments of various types of C-H bonds are still a topic under study. Some researchers studied the density of DLC as an indicator of H-content, yet the film density is also a function of the bond configuration which requires a better understanding (Saikubo et al., 2008).

2.3 Diamond

2.3.1 Structure

C-atoms in diamond are bonded exclusively by sp^3-bonds, forming a tetrahedral network. The C-C distance is 0.154 nm. Fig. 2.3.1 depicts the cubic unit cell of the diamond structure, which may be thought of consisting of two inter-penetrating face-centered cubic (*fcc*) lattices with one shifted from the other by a translation of $\frac{a}{4}\,(111)$ along the diagonal across the unit cell, where $a = 0.357\,nm$ is the lattice constant of diamond. The diamond structure is also adopted by other elements of the IV group, e.g. germanium and silicon. For two different basis elements, e.g. gallium and arsenic or indium and phosphorus, such a structure of two *fcc* lattices is called the zinc-blende type.

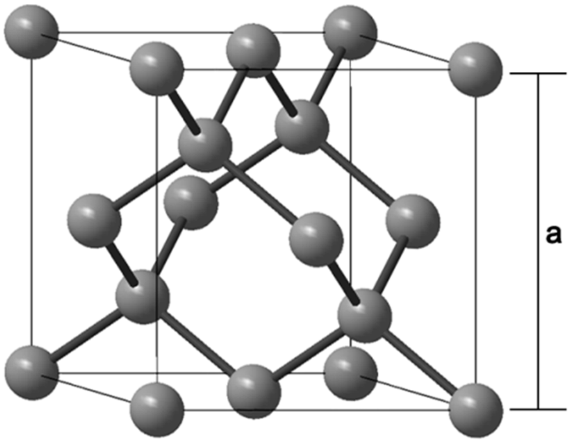

Fig. 2.3.1 Crystallographic unit cell (unit cube) of the diamond structure.

2.3.2 Properties and applications

Diamond has very unique mechanical properties, particularly a high hardness and high Young's modulus (10000 HV and 1050 GPa, respectively). As the hardest material on earth, diamond defines the hardest end on Mohs' scale with a hardness of 10 and is applied to test the Vickers hardness of other materials. Diamond particles are widely used in cutting and polishing tools. It is noteworthy that diamond is yet relatively brittle and cleaves most likely along the <111> plane (Buckley, 1981). Diamond is chemically inert and remains stable up to ~ 800 °C in oxygen (i.e. the ignition point) or in water (Gogotsi, Kraft, et al., 1998). Diamond's optical, thermal, and electrical properties are also exceptional. For instance, with a wide band gap of ~ 5.45 eV, pure diamond is usually defined as an insulator (band gap greater than 4 eV) but is also often mentioned as a wide-bandgap semiconductor in literature; doped diamond is capable to serve as a good semiconductor.

In the form of coatings, diamond's application potential becomes even greater in mechanical applications and other functional materials, e.g. optical, electronic, and tribology domains, but it is limited by the relatively high costs mainly attributed to the slow production rate. The tribological properties of diamond films will be reviewed in detail in subchapter 5.1.

2.3.3 Synthesis techniques

It is believed that most natural diamonds were formed in the mantle of the earth more than 500 million years ago and delivered a long distance to the earth's surface by volcanic eruptions. The extreme conditions required for diamond formation, i.e. high pressure (~ 15 GPa) and high temperature (~ 2000 °C), occur in the kimberlite and lamproite zones 150 – 450 kilometers from the surface of the earth, which are geologically called "diamond stability zones". Ever since the discovery that diamond is made up of carbon in the 18th century, attempts have been made to synthesize diamond from carbonaceous materials by imitating the nature's work, i.e. the high pressure and high temperature (HPHT) method as the earliest synthesis technique (Bundy et al., 1955). Further improvements such as the use of certain molten metals serving as solvent catalyst have been studied to reduce costs and improve the quality of the grown diamonds. Complex apparatus for gem quality diamond production were reviewed by Choudhary and Bellare (2000). Recently, it was reported that a single crystal diamond with a diameter of ~ 2.5 mm, being rarely large, was produced by an FeCoNi-catalytic HPHT synthesis (Zhang et al., 2008). Despite the size limitation, the HPHT diamonds are widely used in cutting tools and grindings.

Diamond films grown by CVD techniques exploit a new field of applications of this renowned material. Unlike HPHT, which mainly involves an equilibrium transformation process, CVD can be conducted under pressures 6 orders of magnitude lower, where diamond is thermodynamically metastable. Wide options of precursors and divers activated CVD techniques allow the resultant diamond films to take different forms, either single-crystalline or polycrystalline diamond films with different grain sizes. CVD synthesis of diamond is recently reviewed by Schwander and Partes (2011). The parameter window for diamond deposition is very narrow compared to that of a-C:H.

A simplified review of deposition of different diamond films, focusing on various precursors used and the corresponding growth mechanisms, is given as follows. Hydrocarbons such as C_2H_2 (Gicquel et al., 2001) and CH_4 (Avigal et al., 1997) diluted with H_2 can be used as precursors for CVD synthesis of diamond films, resulting in a structure from microcrystalline diamond (MCD) to nanocrystalline diamond (NCD) (O. A. Williams et al., 2008). The CH_4 content is typically lower than 3 %, depending on the different CVD rigs. A generally accepted mechanism is that dissociated C-containing groups are adsorbed on the substrate surface, forming sp^2- and sp^3-hybridized carbon clusters, among which those of sp^2-hybridized amorphous and graphitic carbon structures are preferentially etched away by activated H atoms (May, 2000). In addition, H atoms stabilize the growing diamond by termination of the dangling bonds. Consequently, only diamond clusters remain to grow. Moreover, the growth of crystalline diamond is epitaxial because re-nucleation of new diamond grains is also suppressed in this case. Therefore, a high H_2 content in the precursor enables the high quality of diamond. But, the growth rate is extremely low, which in principle leads to high costs of such films. An addition of less than 1 % of oxygen in any form, e.g., O_2, CO, or alcohol, has a similar effect of etching the sp^2-hybridized carbon clusters (Muranaka et al., 1990). Since re-nucleation is suppressed, only a small portion of those small grains evolved from the initial nuclei can survive and continue to grow as the film gets thicker, while the growth of others small grains are inhibited. Therefore, the eventual grain size, ranging from nanocrystalline to microcrystalline, is dependent on the film thickness. (Kobashi, 2005; O. A. Williams et al., 2008)

The fabrication of ultra-nanocrystalline diamond (UNCD) is a quite different picture, where inert gas, e.g., Ar_2 (Sumant et al., 2005), N_2 (Sharma et al., 2012), or CO_2 (De Barros Bouchet et al., 2012) is used to dilute the hydrocarbon precursors instead of H_2. During the film growth sp^2-bonds are etched slowly and the growth at sp^3-sites is interrupted effectively. The diamond grain sizes can be as low as 3 – 5 nm regardless of the film thickness, and the grain boundaries are expected to contain sp^2-C.

2.4 Graphite as a reference material for electron energy loss spectroscopy

C-atoms in graphite are purely sp^2-hybridized. Graphite has a layered structure, which is held together by weak Van der Waals forces. As shown in Fig. 2.4.1, within the layer the carbon atoms are arranged in a regular hexagonal lattice and the C-C distance is 0.142 nm, which is closer than that in diamond. The distance between adjacent basal planes is 0.335 nm.

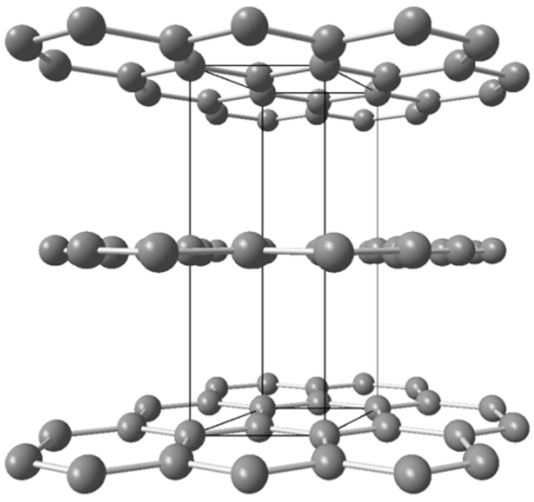

Fig. 2.4.1 Crystallographic structure of hexagonal graphite with solid black lines indicating the unit cell.

This special anisotropic feature of the graphite structure, i.e. with strong in-plane C-C bonds and weak inter-plane bonds, leads to anisotropic materials properties, e.g., in the mechanical, electrical, and thermal materials behavior. Specifically, the mechanical properties of graphite are generally regarded as “soft”. Its basal planes are surprisingly easy to get isolated, making the fascinating 2D graphene (Geim & Novoselov, 2007). As a good electric conductor the electricity is mainly conducted along the planes of the layer, resulting from the electrons in the delocalized π orbitals which are free to move within the space between two adjacent layers.

The determination of the sp^2-C fraction in carbon materials by quantitative EELS requires a standard material with pure sp^2-C as reference, and graphite is in general preferred for this purpose. It is nowadays very easy to get a graphite TEM specimen with perfect structure and free of damage. Highly ordered pyrolytic graphite (HOPG) of high quality is commercially available, whose perfect structure can be well conserved by cleavage (Geim & Novoselov, 2007) from various sorts of damaging that could occur in other TEM sample preparation techniques. For the acquisition of EELS spectra, the problematic anisotropy of graphite can be nicely solved by working at the so-called magic angle condition (MAC). This issue will be discussed in more detail in sections 3.4.4 – 3.4.5. In some work it has also been shown that C_{60} could serve as a good reference material for the quantification of the sp^2-fraction by EELS due to its spherically averaged structure by nature (Papworth et al., 2000). However, the use of C_{60} is complicated because of its sensitivity to radiation damage, which leads to a fading of the π-resonance intensities in low-loss EELS spectra (Egerton & Takeuchi, 1999), and therefore C_{60} is a risky choice as a reference material.

Since the friction and wear of diamond and DLC layers are of great interest in this work, it is good to mention that the well-known lubricating property of graphite is commonly attributed to the intrinsic low shear resistance due to its layered structure in form of sp^2-hybridized C. More detailed, it has been shown that the lubricant effect of graphite only occurs in H-containing atmosphere, whereas under dry or vacuum conditions the graphite could wear away as dust and appear high friction (Savage, 1948). Dienwiebel et al. (2004) observed superlubricity of graphite which is attributed to small graphite flakes transferred to the tip of a friction force microscope. The wear mechanism of graphite could be considered a clue for the friction and wear mechanism of DLCs where sp^2-C plays an important role as well.

3 Analytical transmission electron microscopy

In this chapter a brief introduction is given in the fundamentals of analytical transmission electron microscopy, which means the combined use of imaging TEM techniques and electron diffraction together with spectroscopic methods like EELS and EDXS. In the following presentation the latter is excluded, since only EELS allows the determination of the sp^2/sp^3-ratio of carbon-containing specimens which is the focus of the experimental work reported in chapters 4 and 5. For more detailed information regarding analytical TEM, particularly the fundamentals of EELS, interested readers are here referred to corresponding reviews and textbooks like, e.g., those of D. B. Williams and Carter (1996), Egerton (2009), Brydson (2001), or Schneider (2011), respectively. Since TEM sample preparation is a very important prerequisite, essentially determining whether the subsequent analyses will result in a success or failure, this topic is treated at the beginning of this chapter.

3.1 Sample preparation for transmission electron microscopy

3.1.1 Conventional sample preparation

Conventional TEM sample preparation involves the combined use of mechanical means for thinning like grinding as well as polishing and Ar^+-ion millings as final step to obtain electron-transparent specimens. In principle, for a specimen consisting of a substrate with a deposited layer on top there are two types of preparation depending on the view of observation. That is, during TEM inspection the specimen surface can either be orientated in perpendicular direction (plane-view specimen) or parallel (cross-section specimen) to the incident electron beam. For cross-section view of thin films, the diagram in Fig. 3.1.1 depicts the corresponding technique of classical sandwich preparation.

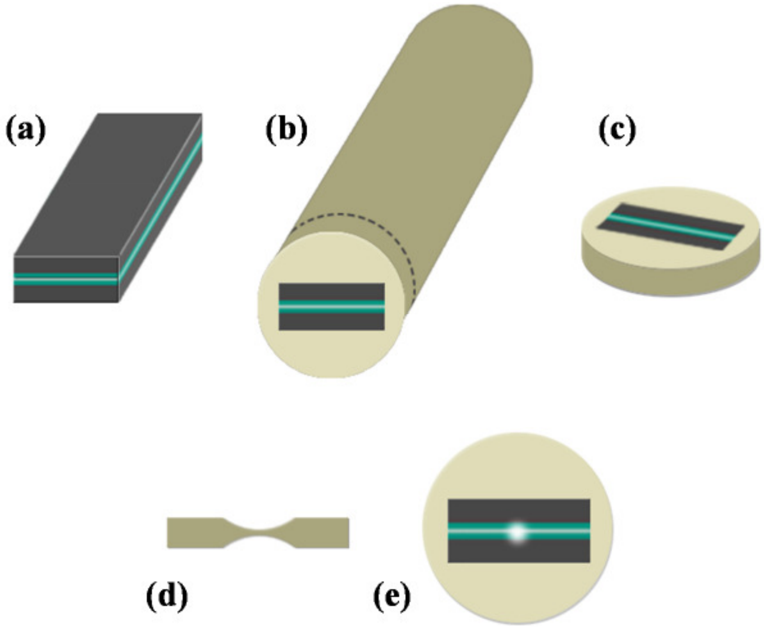

Fig. 3.1.1 Scheme for the preparation of a conventional sandwich TEM specimen: (a) sandwich; (b) sandwich embedded in a 3-mm-diameter cylinder; (c) a specimen slice cut from the cylinder and polished down to ~ 50 µm thickness; (d) side view of the specimen after dimpling; (e) the final specimen after Ar^+-ion beam thinning.

A sandwich is made from two pieces of a specimen with the two coated surfaces glued against each other (Fig. 3.1.1(a)), followed by embedding in a 3-mm-diameter hollow cylinder (Fig. 3.1.1(b)). A specimen slice is then sawed from the cylinder and polished down to ~ 50 µm thickness with smooth surfaces (Fig. 3.1.1(c)), which will be later dimpled from both sides until the central specimen region is as thin as 2 ~ 3 µm (Fig. 3.1.1(d)). Further thinning with Ar^+-ions at 3 keV produces a hole in the middle, around which the electron-transparent areas are present for TEM investigation (Fig. 3.1.1(e)). For preparing cross-section TEM specimens of the diamond and DLC specimens under investigation in this work, an advanced Ar^+-ion milling technique, namely the so-called single-vector technique (Dieterle et al., 2011), was applied to get large thin areas. At the final stage, the Ar^+-ion energy is reduced to 1 keV and polishing is carried out for 5 min to reduce possible damage.

3.1.2 Focused-ion-beam (FIB) assisted sample preparation

Focused ion beam (FIB) is an effective tool for TEM cross-sectional sample preparation (see, e.g., Giannuzzi (2005)). The capability to prepare site-specific at the sub-micrometer level is the most endorsed advantage of this technique over the conventional mechanical thinning combined with Ar^+-ion milling.

Most of the diamond and DLC specimens studied in this work were prepared for TEM by FIB. Conventional TEM cross-section sample preparation was seldom applied, but particularly to compare the effects of specific sample preparation, i.e. conventional or FIB-assisted, onto the occurrence of damage of the carbon layers caused thereof. For FIB preparation, at first the specimen surface was coated with an Au protective layer in an external sputter apparatus, followed by the deposition of a Pt layer from an appropriate metal-organic compound ($C_9H_{16}Pt$) by Ga^+-ions in the FIB. Cross-section lamellae were prepared using a standard “lift-out” procedure with a 30 keV Ga^+-beam, the energy of which was reduced to 5 keV during the final milling stage.

The “lift-out method” is a well-established FIB technique in TEM sample preparation: with an energetic Ga^+-ion beam, the TEM lamella is milled directly at a selected object site. Before the last cut, a delicate micromanipulator is already bonded to the lamella by welding its tip to the lamella with deposited Pt. The lamella can then be lifted out and transferred onto a copper TEM specimen supporter by the micromanipulator. After bonding to the supporter through Pt deposition, the lamella can be cut free from the micromanipulator. Finally, the lamella is thinned to the wanted thickness. To be on the safe side, the lamella usually contains one or two bars with larger thickness to improve the mechanical stability, forming two or three windows of electron-transparent areas with ~ 3 µm in width.

Great caution must be taken to reduce any Ga^+-ion beam damage for such FIB-fabricated TEM cross-sectional specimens. The damage can occur on both side surfaces of the TEM lamella as well as the specimen surface and is harmful for various studies. Firstly, the formation of an amorphized damaged layer covering the side surfaces may blur the contrast of corresponding TEM images, especially in the case of atomic-resolution HRTEM imaging. In addition, such a damaged layer certainly leads to errors in determining the true microstructure and chemical bonding, i.e., the sp^2/sp^3-ratio of DLC layers. Worse yet, due to the amorphous structure of DLC, any artifacts of amorphization caused by the specific TEM sample-preparation procedure are difficult to distinguish. It is also noteworthy that the surface of the original specimen is of great interest for tribology behavior analysis.

In order to protect the specimen prior to sectioning, a Pt/C layer was deposited on top of the specimen by the FIB at low energy for preserving the original surface from the Ga^+-ion milling. Hard materials like DLC and diamond, which require a long time of milling, need Pt/C protective layers thicker than 1 µm to ensure adequate protection.

It is necessary to prevent the carbon-containing specimens from any implantation effect during the Pt/C deposition and also from pollution by carbon of that Pt/C protective layer. For this purpose, a gold layer with a thickness of ~ 100 nm was deposited on the specimen by an external sputter coater, prior to the FIB treatments. Fig. 3.1.2(a) shows a FIB lamella of a diamond film with only a protective Pt/C layer. The lamella was taken out of a diamond film after tribological testing. An amorphous tribo-induced layer, being several tens of nm thick, can clearly be seen on top of this diamond film (details will be discussed in Chapter 5). However, the interface between the Pt/C layer and the a-C layer is blurry. Dark dots in the near surface region of diamond were later confirmed as Pt particles by their lattice distances (not shown here), whose dark image contrast is due to the higher atomic number compared to carbon. Fig. 3.1.2(b) shows another FIB lamella of the diamond film under the double protection of an Au layer and a Pt/C layer, where the interface region between the Au and the a-C layers was kept clean.

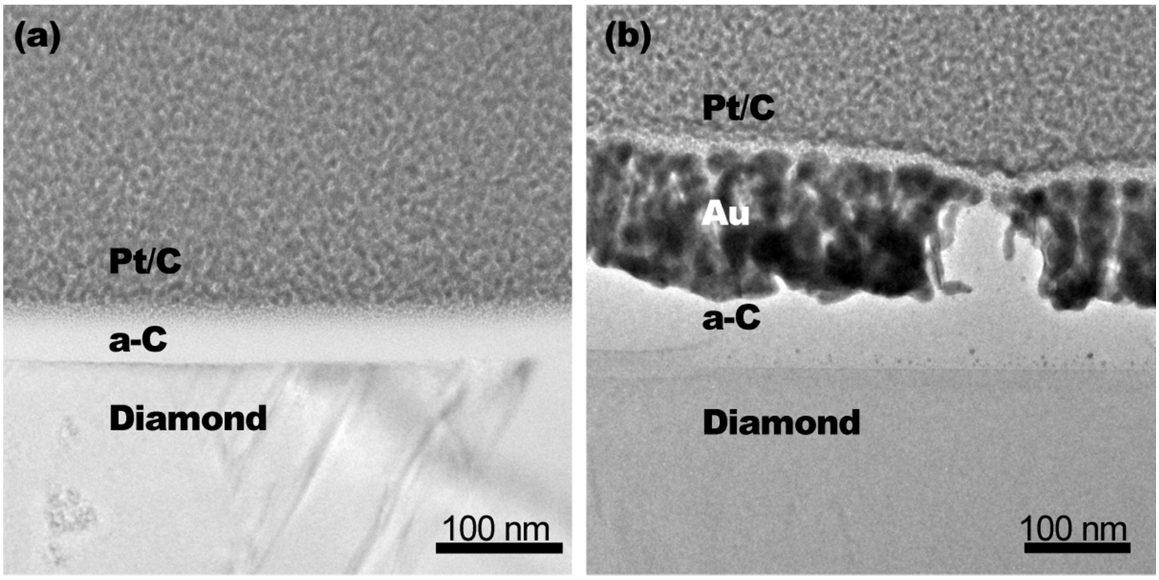

Fig. 3.1.2 Surface region of FIB lamellae (a) without / (b) with the protection of an Au layer deposited in an external physical vapor deposition (PVD) coater in addition to the Pt/C layer deposited by the FIB.

Additionally, the FIB thinning procedure is generally divided into two stages: first thinning by higher energy Ga^+-ions to obtain a high removal efficiency and later reducing the Ga^+-ion energy to minimize the damage for final polishing. The formation of an amorphized layer on the side walls of the specimen due to the Ga^+-ion bombardment is explicitly verified for crystalline Si (Kato et al., 1999). Sophisticated manipulation of FIB allows further cutting of a bar from a prepared cross-sectional TEM lamella to investigate the lamella’s profile, as is illustrated in Fig. 3.1.3. For crystalline Si, damaged amorphous layer could be easily distinguished from the original crystalline structure in TEM. The Ga^+-ion energy was revealed as an important parameter for the depth of such amorphization zones, and the thickness of the amorphous layer was reduced from 22 nm to 2.5 nm by decreasing the Ga^+-ion energy from 30 keV to 5 keV.

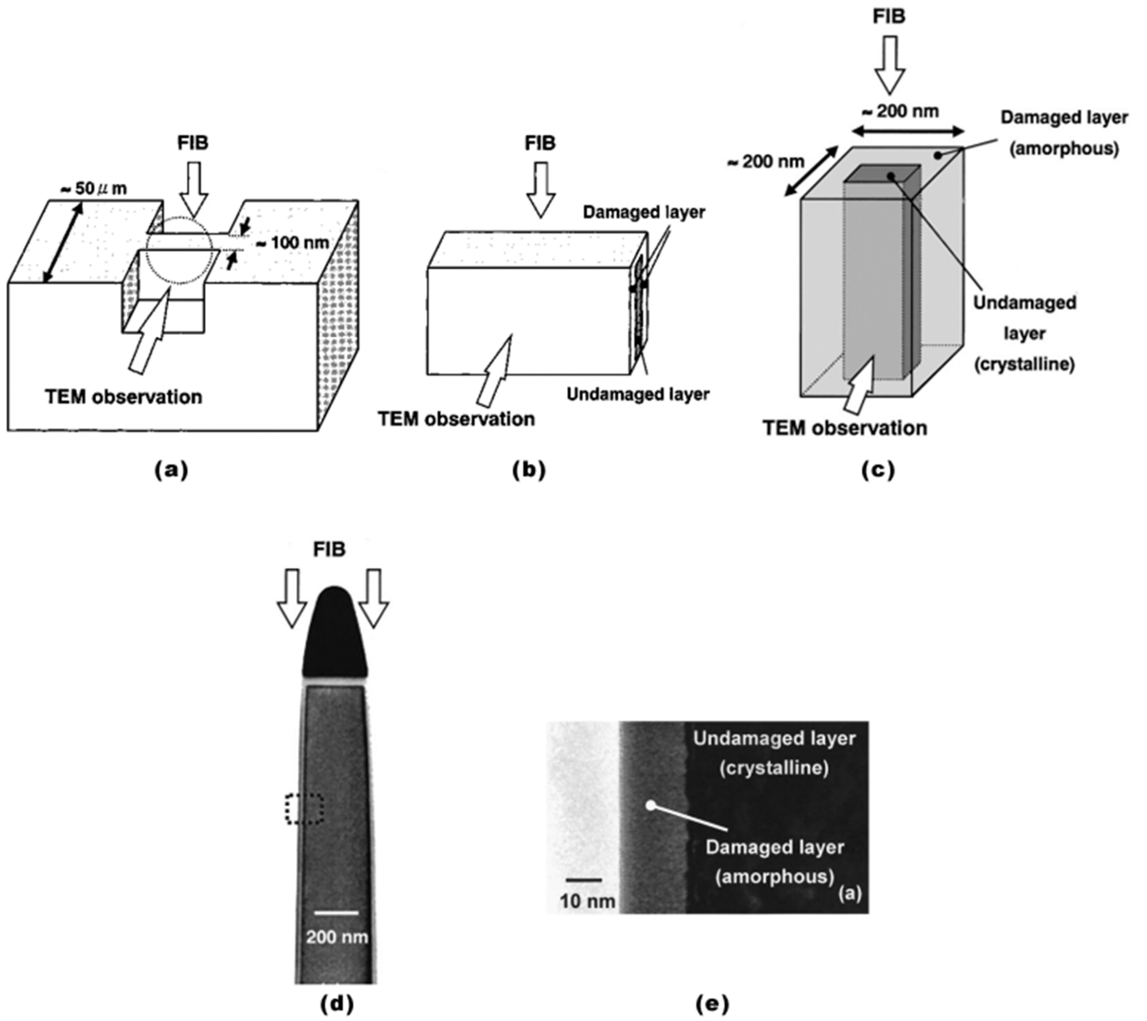

Fig. 3.1.3 (a-c) Methodology for TEM study of FIB-induced amorphization on crystalline materials; (d, e) TEM images showing the amorphous FIB-damaged layer on crystalline Si. (Kato et al., 1999)

3.2 Transmission electron microscopy

It is generally accepted that a transmission electron microscopy (TEM) can be well compared with a light microscope with respect to both its setup and the way of image formation. Therefore, a TEM is optically composed of three main components, namely the illumination system, the objective lens as the most important part for image generation, and the imaging system. In more detail, the conventional illumination system is set up by an electron gun and at least two condenser lenses, providing an electron beam as the “light source”. Here, the electron gun produces electrons that are accelerated up to a desired energy by means of a multi-stage anode subsequently following on the optical axis. The resulting electron beam is then focused to a ray with the desired diameter by the action of the condenser lenses (Sigle, 2005; D. B. Williams & Carter, 1996).

Usually, in a modern TEM there are more subassemblies as technology develops. For example, in a state-of-the-art Titan microscope of FEI company the illumination system has six lenses, including a gun lens, three condenser lenses, a minicondenser, and the upper objective lens, which is taken into account because the specimen is located in between the upper and lower pole piece of the objective (see Fig. 3.2.1). With all the lenses excited and well-aligned, good illumination conditions can be achieved for TEM as well as HRTEM (cf. Fig. 3.2.1(a)), where the beam is kept near-parallel even in spreading or condensing mode. In probe mode, the beam convergence is controlled by the beam diameter at condenser lens C3 (seen by comparing Fig. 3.2.1(b, c)). Either a cross-over is formed between the C2 and C3 lenses or not, a similar ray-path after C3 can still be achieved (seen in Fig. 3.2.1(c, d)). With the cross-over formed, C2 is strongly excited and the variation range of convergence angle is large (Fig. 3.2.1(c)), namely “large range”. Compared to this real cross-over case, in Fig. 3.2.1(d) C2 and C3 are adjusted to form a virtual cross-over further away from C3. In the latter mode C2 is almost off and preferentially contributes little spherical aberration to that of the objective lens, namely “normal range”. The minicondenser is off in Fig. 3.2.1(b, c and d), where C3 forms a nearly parallel beam for the upper objective lens and a probe with relatively large convergence angle that can be focused onto the specimen. This is called nanoprobe mode, because the focused probe has a small diameter, which is beneficial for STEM imaging where the obtainable lateral resolution is directly controlled by the probe diameter. On the contrary, for microprobe mode, where the minicondenser is on (cf. Fig. 3.2.1(e)), the beam is focused by C3 on the front focal plane of the minicondenser, making a parallel beam between the minicondenser and the upper objective lens with a small diameter. Afterwards, the beam is focused by the upper objective lens on the specimen, resulting in a small convergence angle. In this mode, the convergence angle could be five times smaller than in nanoprobe mode, but the beam diameter is larger, which gives its name microprobe mode. The extreme case in this mode with the smallest beam convergence angle of 0.5 mrad is optically similar to the condensing TEM mode (FEI-Company).

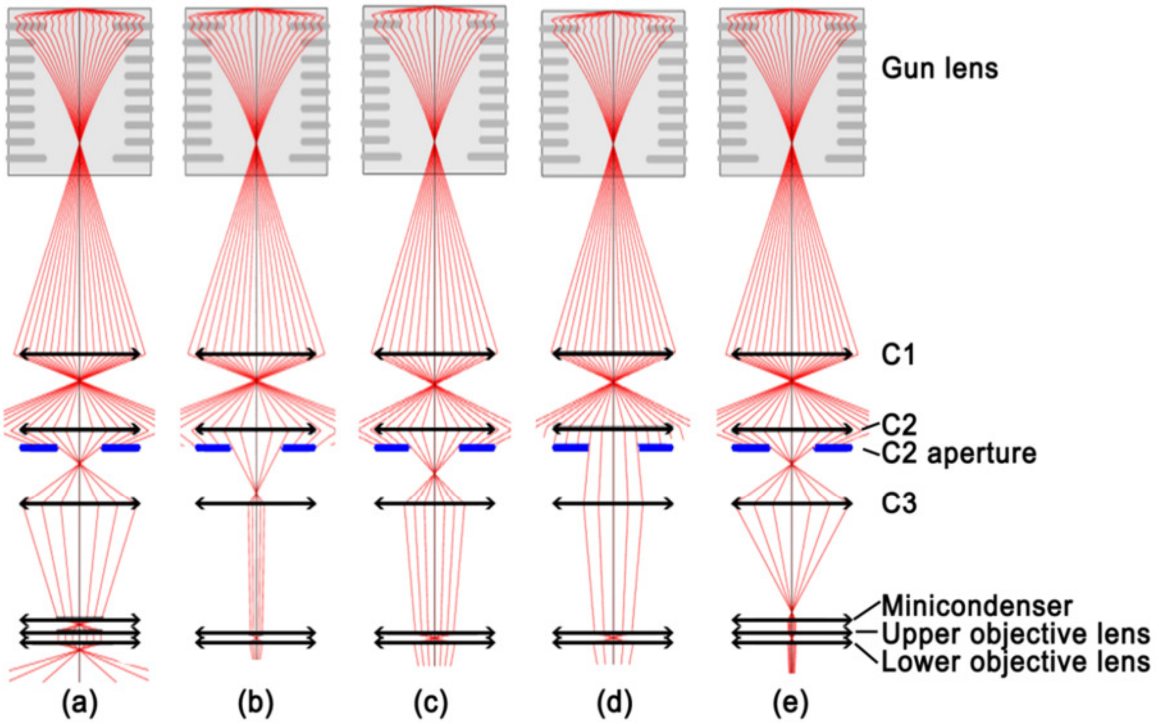

Fig. 3.2.1 Optical modes of a Titan microscope. (a) TEM mode with minicondenser on; (b) nanoprobe mode with small convergence angle under "large-range" setting; (c) nanoprobe mode with large convergence angle under "large-range" setting; (d) nanoprobe mode with large convergence angle under "normal-range" setting; (e) microprobe mode under "large-range" setting. (FEI-Company)

Fig. 3.2.2 shows the ray paths after the specimen in a transmission electron microscope operated in diffraction and imaging modes, respectively (for further details, see D. B. Williams and Carter (1996), Egerton (2009), etc.). The first lens after the specimen, the objective lens is considered the heart of an electron microscope. The objective lens generates the primary diffraction pattern and the first intermediate image in defined planes, i.e. the objective back-focal-plane (BFP) and the so-called first intermediate image plane. The magnification of the first intermediate image is between 50 and 100 times. In the first intermediate image plane the selected-area aperture can be positioned, while the objective aperture is set in the BFP. For crystalline samples, the size and position of the objective aperture defines the specific kind of image contrast. In more detail, for diffraction-contrast TEM imaging a bright-field (BF) image is obtained when the unscattered beam, i.e. the (000 beam), is selected, whereas a dark-field (DF) image can be formed by the selection of a certain diffracted beam. In the case of HRTEM imaging, many diffracted beams pass the BFP by the choice of a large aperture centered relative to the optical axis, thereby allowing their interference and forming of a phase-contrast image.

The further magnifying imaging system usually consists of three or four intermediate lenses and a projector lens at the end. The object plane for the first intermediate lens, also known as the diffraction lens, can be adjusted to be the BFP (Fig. 3.2.2(a)) or the first image plane (Fig. 3.2.2(b)) of the objective lens, giving a diffraction pattern or image as object for latter lenses to magnify. Each lens in this system contributes about 20 times of magnification, with the last projector lens fixing its final magnification and consequently its image plane at the viewing screen.

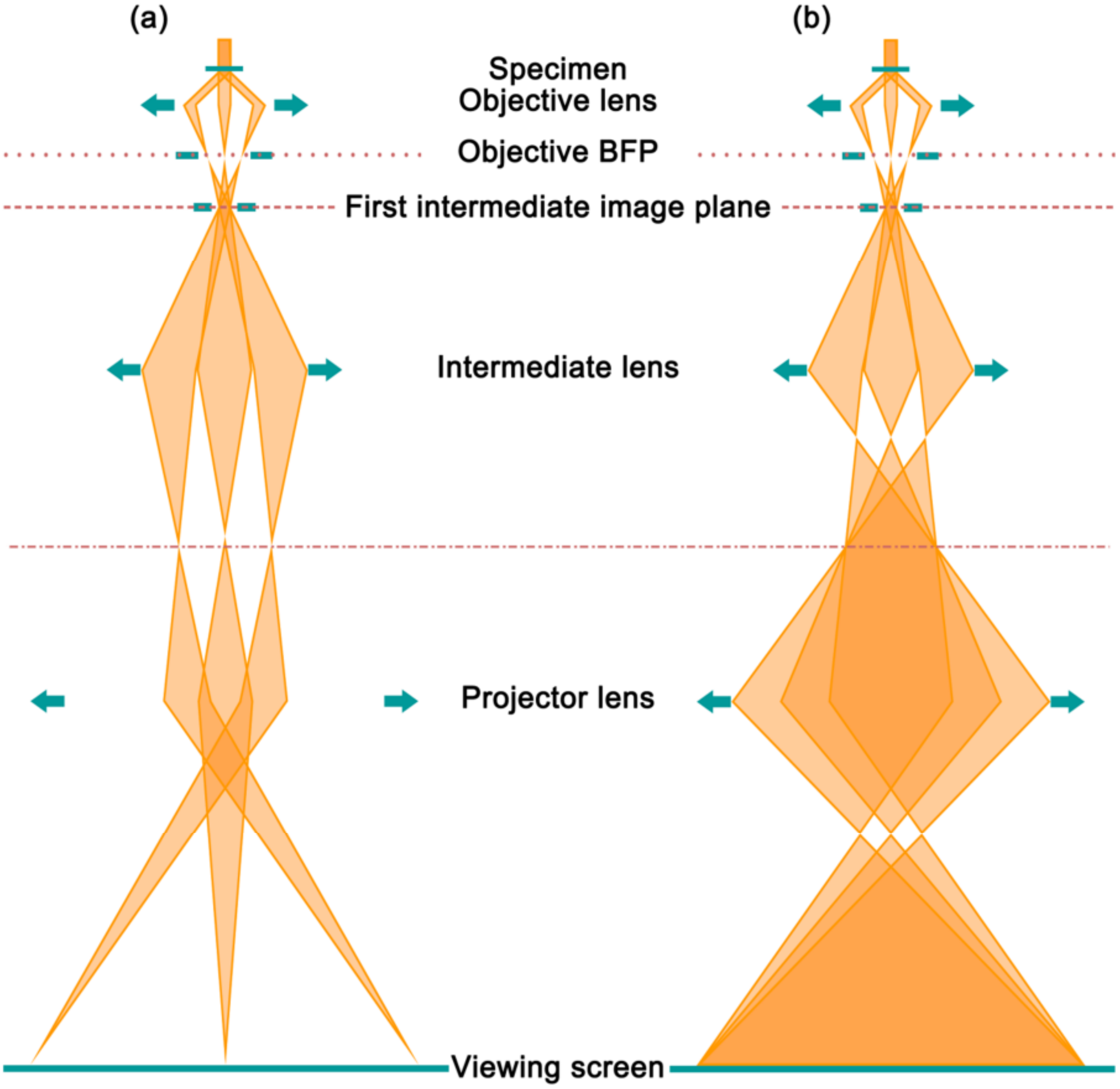

Fig. 3.2.2 Schemes of TEM ray paths in (a) the diffraction mode and (b) imaging mode.

3.3 Scanning transmission electron microscopy (STEM)

By operating the TEM illumination system in probe mode (already described in the previous section), a convergent beam of electrons can be focused on the specimen, whose position is controlled by a pair of x-y scan coils that scan the electron probe across the sampled area. Under these conditions the microscope is run in the so-called scanning TEM (STEM) mode, where, unlike to TEM, no electron lenses are used for image formation. STEM images are obtained by means of a particular interaction signal that can be gathered by a suited electron detector. Hence, the transmitted electrons collected by a scintillator on the optical axis, multiplied and displayed as a function of the probe position yield a BF STEM image. It can be shown that for crystalline materials STEM BF images exhibit an image contrast being comparable to that of conventional TEM diffraction-contrast images (see, e.g. Bethge and Heydenreich (1987)).

Similarly, a DF STEM image can be generated when a scintillator in form of a ring is used as detector, therefore preventing the (000) beam to contribute to the measured signal. For a ring with a relatively large inner diameter a high-angle range of scattered electrons is covered, resulting in a high-angle annular dark-field (HAADF) image. An HAADF image is formed by Rutherford scattered electrons, the intensity of which strongly depends on the mean atomic number of the transmitted volume. With other words, under well-defined angle conditions HAADF images show distinct material (Z-) contrast, where the intensity of each image pixel is roughly proportional to the second power of atomic number, Z^2. (Lebeau & Stemmer, 2008) Such an image, to a first approximation, can be treated as a convolution between the probe-intensity function and the object function, where the width of the former, i.e. the probe size, dominates the image resolution. (Browning et al., 2012)

In the case of HAADF STEM imaging, however, the post-specimen lenses are no longer used for image magnification, but to allow the electrons of a desired range of scattering angles to match with different detectors, i.e. the HAADF detector or the entrance aperture of an EELS spectrometer, by controlling the camera length. Specifically, this is of great importance for quantitative EELS at magic angle conditions (see details in sections 3.4.4 – 3.4.5).

STEM is compatible with many TEM analytical techniques requiring a focused electron beam, such as EDXS, nano- as well as microdiffraction, and EELS (Utsunomiya et al., 2011). Ever since the pioneering work of Crewe et al. (1971) who installed an EELS spectrometer in a STEM, EELS can be obtained with atomic resolution by simultaneous *Z*-contrast imaging (Browning et al., 1997). Furthermore, maps of elemental and chemical-bonding details are attainable by selecting a specific part of core-loss spectra (Muller et al., 1993), which can be compared with the energy-filtered TEM (EFTEM) technique, but, in contrast produces images in a sequential manner.

3.4 Electron energy loss spectroscopy (EELS)

3.4.1 Fundamentals

As a high-energy electron beam hits a thin specimen, most of the electrons penetrate the specimen and are involved in an elastic or inelastic scattering event, besides those being directly transmitted without any interaction. In the positive charge field of the nuclei the elastically scattered electrons change their direction of motion more or less (Rutherford scattering), but their energy remains essentially unchanged. These elastic scattering events strongly depend on such parameters like primary electron energy, density of the transmitted material, and its mean atomic number, thereby being the main reason for contrast generation in conventional TEM imaging. In addition, there are inelastically scattered primary electrons, which have lost energy by the interaction with electrons bound to atoms in the sample. This primary inelastic scattering process is very complex and causes such secondary processes like the generation of characteristic X-rays or the emission of Auger electrons (cf. Fig. 3.4.1). The inelastically scattered electrons themselves are primarily very informative and their energy loss and/or angular distribution can be measured by EELS. In general, an EELS spectrum allows identifying the chemical elements within the transmitted specimen volume qualitatively as well as quantitatively, and in addition its electronic properties and the specimen thickness.

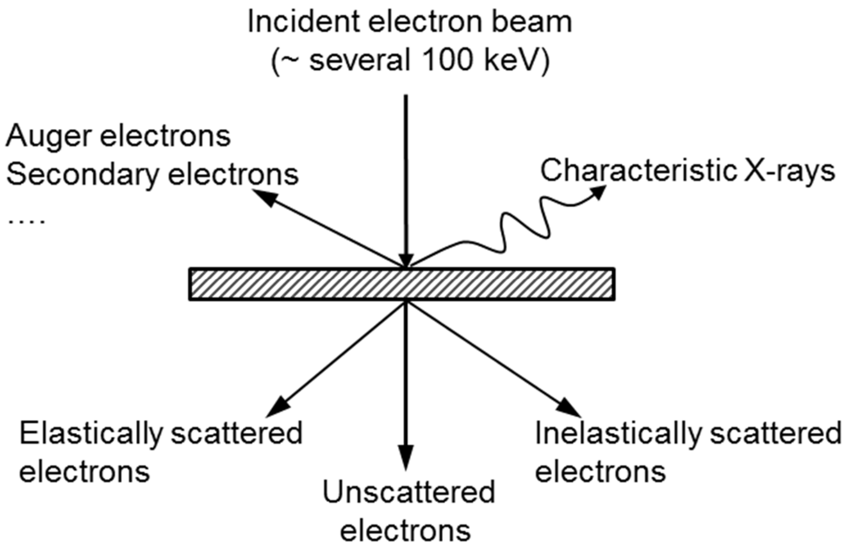

Fig. 3.4.1 Scheme of possible interactions of the incident electron beam and a thin specimen.

Without going into much detail, it should be noted that the probability for inelastic scattering of an electron in a solid angle Ω and with an energy loss between E_i and E_{i+1} is given by (see, e.g., Egerton (1996) and Verbeeck et al. (2006)):

$$J(E_i) = \int_{E_i}^{E_{i+1}} M(E)N(E)dE\,. \qquad 3.1$$

In this formula, E is the energy loss suffered by the primary electron, and $N(E)$ is the density of states (DOS) function of the excited atom, determining whether a certain final state $|f\rangle$ with an excitation energy E is occupied or not. According to Verbeeck et al. (2006) the so-called matrix element $M(E)$ is defined by

$$M(E) = \int_{\Omega} \frac{d^2\sigma}{d\Omega dE} d\Omega \propto \int_{\Omega} \frac{1}{q^2 E} \frac{df}{dE} d\Omega, \qquad 3.2$$

with

$$f(E,q) = \sum_{|f\rangle} \frac{E}{q^2} \left| \left\langle i \middle| \sum_j^N e^{i\boldsymbol{q}\cdot\boldsymbol{r}_j} \middle| f \right\rangle \right|^2 \delta\left(E_{initial} - E_{final} - E\right), \quad 3.3$$

where $d^2\sigma/d\Omega dE$ is the double differential scattering cross-section (DDSCS), and $f(E,q)$ is the generalized oscillator strength (GOS) for exciting an initial N-particle state with an energy $E_{initial}$ $\langle i|$ to all possible final states $|f\rangle$ with an energy E_{final}, the momentum transfer $\boldsymbol{q}$ and position coordinates of the atomic electrons $\boldsymbol{r}_j$. In principle, an EELS spectrum represents the double differential scattering cross-section integrated over the scattering angle range which is defined by the maximum collection angle of the spectrometer, solely yielding the energy-differential cross-section, $d\sigma/dE$. It can be shown that this energy-differential cross-section increases with decreasing atomic number Z (Egerton, 1996). This is the reason why particularly light elements like boron, carbon, nitrogen, and oxygen are detectable with high efficiency by EELS, even lithium (Z = 3) and beryllium (Z = 4) can easily be detected; under special circumstances, i.e. a TEM with a gas inlet chamber, the gaseous species hydrogen and helium are also verifiable.

From this point of view, EELS is a powerful addition to EDXS, because the latter is more sensitive to detect elements with intermediate or high atomic numbers. This is attributed to the fact that the fluorescence efficiency for the excitation of characteristic X-rays rises with increasing Z. Thus, both EELS and EDXS combined with TEM/STEM are the most promising analytical techniques with atomic resolution, but EELS is the only technique also giving information about the chemical bonding state of a detected element because of its extremely high energy resolution of the order of 1 eV and better.

In the following, typical features visible in both the low-loss and high-energy loss regions of an EELS spectrum will be exemplified by corresponding spectra recorded from different carbon modifications, namely graphite, diamond, and a-C:H. In this context, some explanations regarding the physical background of the different inelastic excitation processes will also be given.

Zero-loss peak (ZLP)

Fig. 3.4.2 shows a series of EELS low-loss spectra obtained from different allotropes of carbon, including natural diamond particles (supported by a holey amorphous carbon film on a copper grid TEM specimen supporter), highly ordered pyrolytic graphite (HOPG), and an a-C:H specimen (TEM lamellae of HOPG and a-C:H prepared by FIB). The majority of electrons traverse the specimen without losing any energy, i.e. either they transmit it without any interaction or they are elastically scattered. This type of electrons forms the so-called zero-loss peak (ZLP), which would ideally have no width and appear as a delta function. However in practice, depending on the used electron source the generated primary electrons possess a corresponding energy distribution (typically 0.3 eV for a cold field emission gun (FEG) and about 0.7 eV for a thermally assisted FEG), which results in a finite width of the ZLP and the full width at its half maximum (FWHM) indicates the energy resolution obtainable with the spectrometer system. Moreover, on the ZLP's high-energy tail there could also occur signal intensities due to phonon scattering in addition to the contribution of elastically scattered electrons. Unfortunately, since phonon excitations cause losses of some 10 meV, usually the resulting peaks cannot be seen owing to the above-mentioned limited energy resolution. Of course, besides the energy width of primary electrons the spread of the ZLP is also strongly associated with the electron-optical properties of the EELS spectrometer, particularly its aberrations, and its actual alignment. For the low-loss spectra shown in Fig. 3.4.2, which were recorded by means of an imaging energy filter of the type Gatan Tridiem model 865 HR installed at an FEI Titan 80-300 at 80 kV, the FWHM of the zero-loss peak amounts to 0.6 – 0.7 eV, depending on the experimental stability.

Low-loss region

The region of the spectrum beyond the ZLP up to ~ 50 eV is known as the low-loss region. Here, the energy losses are essentially due to the interactions with outer-shell atomic electrons.

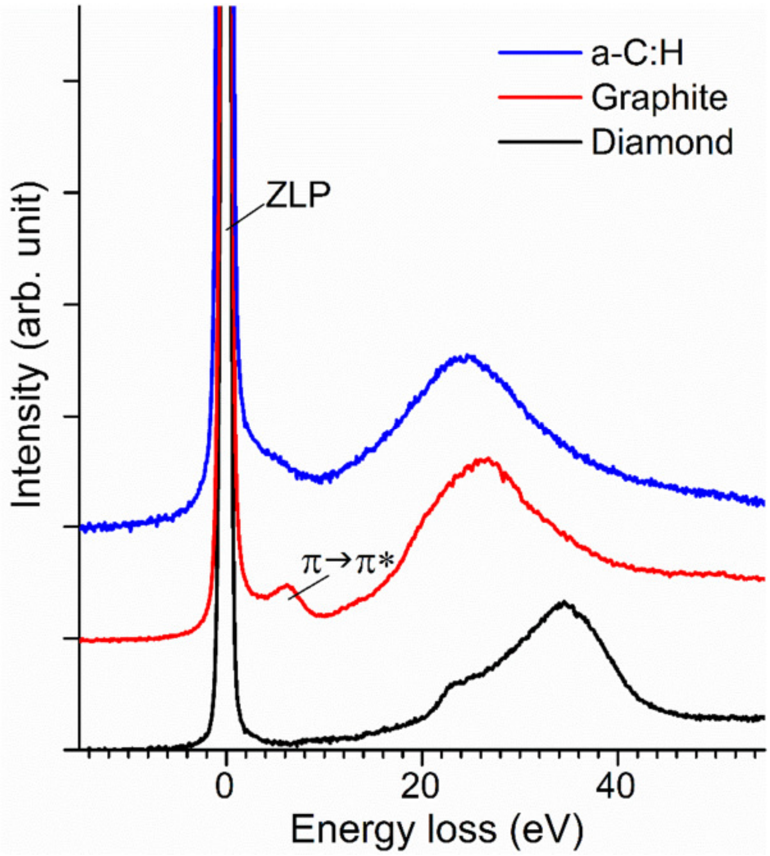

Fig. 3.4.2 EELS low-loss spectra obtained from natural diamond, HOPG, and hydrogenated amorphous carbon.

The lower part (below 15 eV) of the low-loss region is considered to be related to the excitation of electrons in the molecular orbitals. For example, the spectrum of graphite in Fig. 3.4.2 clearly shows a peak at 6.2 eV, which is associated with the transition from π to π* states. This peak disappears for diamond and amorphous carbon, and is regarded as a fingerprint for graphitic carbon (Joy et al., 1986).

Nevertheless, in a low-loss spectrum the signal intensities with energy losses higher than 15 eV essentially involve the "plasmon wake" of valence electrons in a semiconductor or insulator, or conduction electrons in a metal. In such an event, the energy loss of the incident electron, E_{PL}, equals or multiplies the energy carried by the plasmon,

$$(h/2\pi) \cdot \omega_p \, , \qquad 3.4$$

where h is Planck's constant and ω_P is the plasma frequency, which is typically of the order of ~ 10^6 rad/s for most metals, corresponding to E_{PL} around 20 eV. It is known that ω_P is closely related to two factors, namely the density of valence states and the density of the mass. A shift of E_{PL} is indicative of a change in concentration or bonding configuration (Joy et al., 1986). For example, various mechanical and physical properties of Ti-based alloys and soot particles can be evaluated from the particular plasmon energy E_{PL} (Howe & Oleshko, 2004). However, for different materials these values of E_{PL} are too close to identify an unknown element, although E_{PL} is sensitive to the states of those valence/conduction electrons. On the other hand, E_{PL} is expected to show a dependency on the mass density of the material. The use of E_{PL} as a measure of mass density works quite well for the BN system with *h*-BN (sp^2-bonded) and *c*-BN (sp^3-bonded), but is complicated for a-C films with a considerable hydrogen amount incorporated. (Schmid, 1995) For ta-C, Joly-Pottuz et al. (2007) and Xu et al. (1996) have derived empirical relationships for the measurement of hardness, density, and sp^3/sp^2-ratio through E_{PL}. In Fig. 3.4.2 the plasmon peak is seen located at 34.5 eV for diamond with a shoulder at 23.1 eV, but shifted to 26.8 eV for graphite and 24.7 eV for a-C:H. The shapes of E_{PL} for graphite and diamond are close to those in literature, but the positions are slightly different, e.g. for diamond, E_{PL} is at 33.0 eV with a shoulder at 23.2 eV in Schmid (1995) and at 33.8 eV with a shoulder at 24 eV in Berger et al. (1988).

Moreover, the low-loss region is meaningful in measuring the specimen thickness. According to Poisson statistics, the integrated intensity of any plasmon peak, I_n, is given by

$$I_n = P_n \cdot I_{total} = \left(\frac{1}{n!}\right) \cdot \left(\frac{t}{\lambda}\right)^n \cdot e^{-\frac{t}{\lambda}} \cdot I_{total}\,, \qquad 3.5$$

where P_n is the probability of an electron exciting n plasmons, I_{total} is the total intensity accepted by the spectrometer and λ is the plasmon mean free path. Particularly, the integral of the ZLP, I_0, is

$$I_0 = P_0 \cdot I_{total} = e^{-\frac{t}{\lambda}} \cdot I_{total} \cdot \qquad 3.6$$

The relative thickness, t/λ, can thus be easily obtained as

$$\frac{t}{\lambda} = \frac{P_1}{P_0} = \frac{I_1}{I_0}, \qquad 3.7$$

which is the ratio of the integrated intensity of the first plasmon peak I_1 to that of the ZLP I_0.

Last but not least, I_n can be expressed as,

$$I_n = \left(\frac{1}{n!}\right) \cdot \left(\frac{t}{\lambda}\right)^n \cdot I_0\,, \qquad 3.8$$

which takes the advantage of omitting I_{total}, and could be used to remove the plural scattering in the core-loss spectrum by deconvolution (Egerton, 1996).

Core-loss region

The energy-loss electrons having excited core-shell electrons in the specimen shape the core-loss region, which starts above 50 eV energy loss and extends up to approximately 2 – 3 keV. The high energy end of the spectrum depends on the measurable signal intensity that generally falls exponentially with increasing energy loss. In the process of core-shell excitation, the energy-loss is equal to or larger than the critical excitation energy of the single core electron, E_c, which is characterized by the specific atom and electron shell. Therefore, the core-loss signal, also known as the ionization edge in the spectrum is associated with E_c and thus identifies the presence of particular elements in the specimen. Edges are named by the corresponding element and shell, e.g., carbon K-edge for the excitation of the carbon K-shell electron (1*s* electron) into the empty anti-bonding π orbital (π* orbital) or vacuum, respectively. Since the intensity of a given core-loss edge is proportional to the amount of the corresponding element, quantification is also possible.

Fig. 3.4.3 shows a C-K edge spectrum obtained from one of the a-C:H films studied within this work. Obviously, as will be discussed in section 3.4.3 the near-edge fine structures in the energy loss range above ~ 280 eV are typical for carbon with a high fraction of *sp*^{2}-bonds. Moreover, argon, which could be incorporated during the film deposition, is also detected by its Ar-L_{23} edge at the energy loss of 245 eV. The Ar-L_{23} edge is positioned ~ 40 eV in front of the C-K edge, which enables a convenient quantification with an EELS plug-in package in Gatan DigitalMicrograph. The content of Ar is given as less than 1 atom % by EELS quantification, which is indicative of the detection sensitivity of this analysis technique.

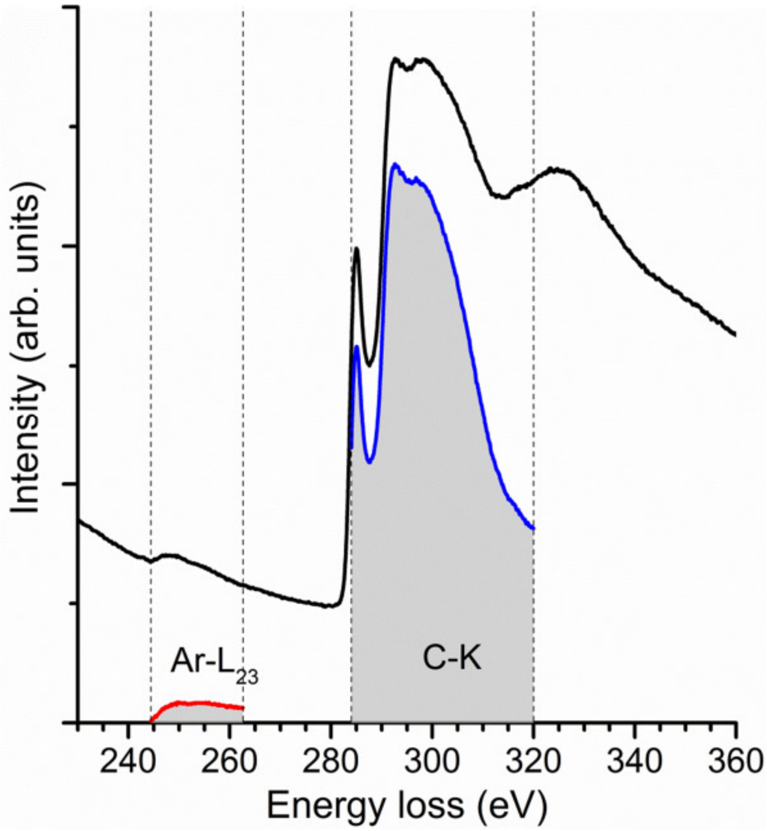

Fig. 3.4.3 C-K edge spectrum from an Ar-containing a-C:H film showing ionization edges of Ar at 245 eV and of carbon at 283 eV.

3.4.2 Post-acquisition data processing

In each case, a core-loss edge is superimposed on a background composed of the tails of ZLP, low-loss peaks, and other core-loss edges with lower energy losses. The maxima of the ZLP and low-loss peaks are usually 2 – 3 orders higher than the signal intensities of core-loss edges, and thus have a significant influence onto the measured EELS spectrum, even in high energy-loss regions. For this reason, the so-called jump-ratio, also known as the signal-to-background ratio, of a particular ionization edge of interest should be optimized during EELS acquisition or examined before data processing. Evidently, as discernable from the Ar-L_{23} edge in Fig. 3.4.3 the jump ratio does depend on the particular element concentration, but also on the thickness of the TEM sample.

In order to quantify the atomic concentration of an element, the spectral background underneath the corresponding ionization edge needs to be removed. Due to the fact that the background contribution cannot be calculated *ab initio*, one has to estimate it from the pre-edge region by modelling. An energy window before the considered ionization edge is chosen where the background is fitted by a suitable function and extrapolated under the edge. There are two rules for choosing this pre-edge region for background-model estimation:

Set the upper limit of the region close to the edge, but exclude any deviation from the general continuously decreasing edge shape; set the lower limit of the region as large as possible, but make sure to keep away from neighbor edges. For EELS background fitting the power-law function is a commonly used model, i.e.

$$I_B = A \cdot E^{-r} , \tag{3.9}$$

where the background intensity I_B is a function of the energy loss E, A and r are the two parameters to be derived by fitting the model to the chosen pre-edge region. Then the model can be extrapolated to the edge region and subtracted from the spectrum, resulting in the net intensity of the particular ionization edge.

Additionally, in contrast to the single-scatter event assumed in the theory of EELS, in reality the electrons can encounter more than once energy loss events. It is unlikely that an individual primary electron, having interacted with a core-shell electron in the sample, will excite another core-shell electron, but there is a certain probability that it interacts with an outer-shell electron and undergoes another low-loss event. This is called plural scattering effect, which becomes more pronounced as the specimen gets thicker. Plural scattering can be removed by Fourier deconvolution of the low-loss spectrum. The quality of this technique can be checked by comparing the deconvoluted spectra with a non-deconvoluted one obtained from a sufficiently thin specimen area, i.e. where plural scattering is much less of a problem. Generally, this technique works reasonably well for specimens with a relative thickness t/λ of 0.3 to 1.

3.4.3 Electron energy loss near-edge structure (ELNES) of the C-K edge

The fine structure visible in close neighborhood to the onset of an ionization-edge, reaching up to approximately 30 eV beyond it, is called energy-loss near-edge structure (ELNES). ELNES features are closely related to available unoccupied electron states, into which the individual core-shell electron can be excited. Since the corresponding density of electronic states is a function of the atomic bonding configuration of the excited atom (for more details, cf., e.g., Brydson (2001) and Egerton (1996), near-edge structures in EELS spectra can be used for chemical-bonding analyses.

In the case of carbon, the K-edge fine structure is pronounced and excitations from 1*s* states to π^* and σ^* states could be well resolved. Recalling that C-atoms in graphite are purely sp^2-hybridized, in diamond are all sp^3-hybridized, and amorphous carbon is generally a mixture of sp^2- and sp^3-hybridizations, where sp^1-C is typically assumed to be negligible (less than 2 %) (Bruley et al., 1995), ELNES is a powerful technique for differentiating between these different carbon allotropes. Evidently, the π^* excitation is exclusively characteristic for sp^2-C. Therefore, the π^* peak can not only be used to identify sp^2-C in C-materials, but also to give quantitative information about the sp^2/sp^3-ratio by its relative intensity compared to σ^* states.

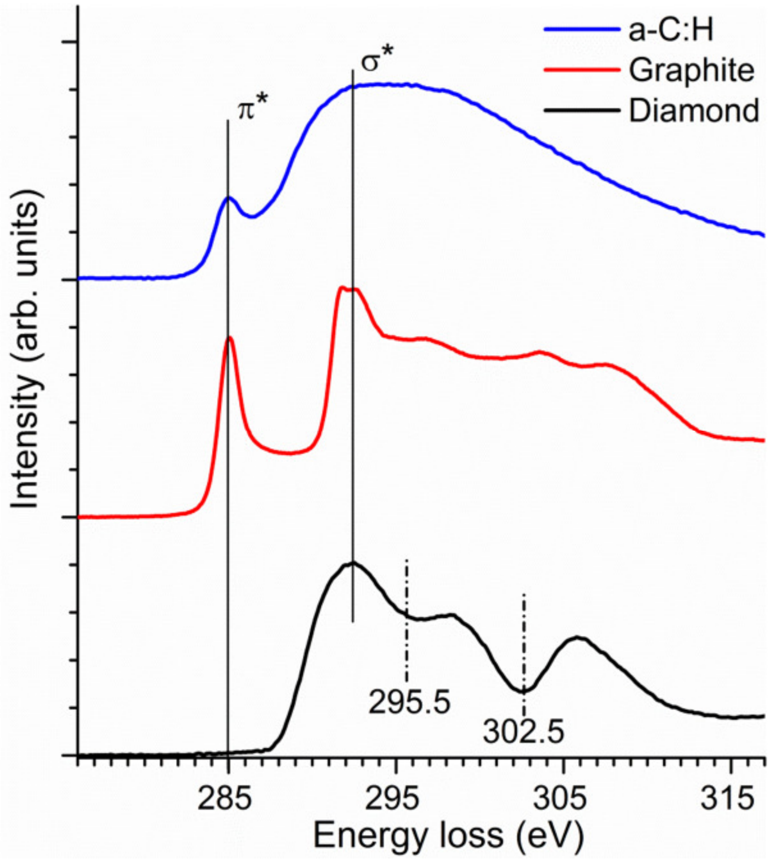

Fig. 3.4.4 Typical EELS spectra of carbon K-edges for graphite, DLC, and diamond.

Fig. 3.4.4 shows examples of C-K edge spectra from DLC, graphite, and diamond. In a C-K spectrum, the pre-peak (π* peak), which is pronounced for graphitic carbon and absent for diamond, is exclusively assigned to a transition from the 1*s* to π* state of an sp^2-hybridized C-atom. In this figure, the maximum of this pre-peak is manually positioned at 285 eV; this calibration is kept constant for all C-K edges measured and shown in this work. However, this position slightly differs from the findings of other researchers. For example, in the EELS studies of a-C specimens Urbonaite et al. (2007) and Alexander et al. (2008) the defined the π* pre-peak position at 284 eV and 286 eV, respectively. Batson (1993) performed high-resolution EELS (energy resolution of 0.15 – 0.22 eV) in a dedicated STEM and found the π* pre-peak at 285.38 ± 0.05 eV. Moreover, the accurate 1*s* level was studied by experimental (Le Normand et al., 2001) X-ray photoelectron spectroscopy (XPS) and calculations thereof (Titantah & Lamoen, 2005), where the 1*s* electron is excited into the continuum, at 284.6 eV for graphite and 285.6 eV for diamond. This is a minor difference could lead to a possible shift of the σ* intensities between graphite and diamond, as well as other C-materials.

For all carbon modifications the main maximum (σ* peak) of the C-K edge is located at ~ 292 eV (see Fig. 3.4.4) and is associated with 1*s* to σ* transitions for both *sp*^{2}- and *sp*^{3}-hybridized carbon atoms. Generally, a featureless σ* peak is ascribed to an amorphous carbon structure (Schmid, 1995), while a relatively sharp σ* peak can be recognized for crystalline graphite. In the work of Batson (1993), the σ* resonance of a natural graphite crystal was further resolved into two components: a Gaussian-shaped sharp peak centered at 291.65 eV and a broad free-electron-like contribution near 292.5 eV (corresponding to a 285.38 eV π* maximum). Additional diamond characteristics above the σ* onset are the two dips at ~ 295.5 eV and 302.5 eV, being indicative of a long-range ordered structure and especially with the latter results from the variation of the density of states correlating with the second absolute band gap in crystalline diamond (Coffman et al., 1996).

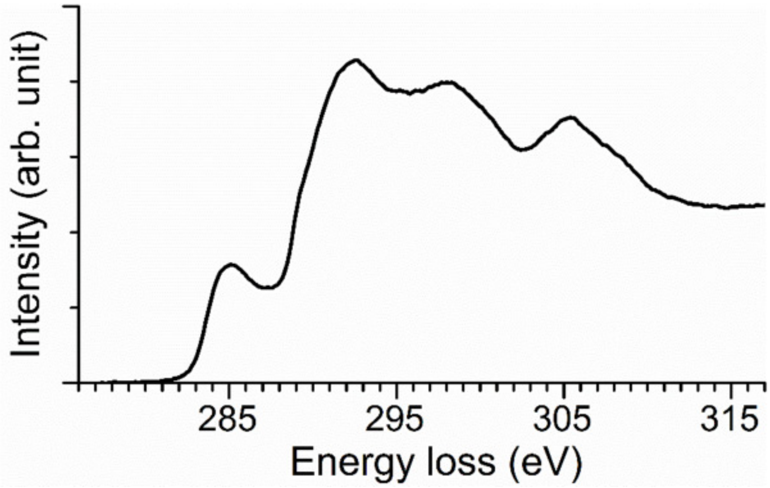

Fig. 3.4.5 C-K edge spectrum taken from a diamond particle on a supporting amorphous carbon film of a TEM grid.

Chemical shifts of the σ* peaks are reported for different carbon materials. According to literature data (Alexander et al., 2008; Batson, 1993; Schmid, 1995; Urbonaite et al., 2007), for graphitic carbon this peak is positioned about 6 – 8 eV higher than the π* peak and is found approximately 7 eV higher in the present work. For diamond, an accurate determination of the σ*-peak position is difficult due to the lack of the well-defined sharp π* peak in the corresponding C-K spectrum as well as the bad signal-to-noise-ratio and signal-to-background-ratio in simultaneous recording of both zero-loss and core-loss spectra. Alternatively, a spectrum was recorded from a µm-sized natural diamond particle supported by a thin amorphous carbon film on the TEM grid (Fig. 3.4.5), where the transmitted spectrum is a sum of both the diamond and the *sp*^{2}-C containing amorphous carbon film. Referring to the π* peak mainly from the supporting film, which is set at 285 eV, the sharp diamond peak is visible at 292.5 eV. However, Schmid (1995) reported that the σ* state for diamond can be observed at an energy loss about 6.7 eV higher than the π* maximum in graphite, which in contrast is 0.6 eV lower than the σ* excitation of graphite. The study of an amorphous *sp*^{3}-rich carbon specimen showed that the σ* peak is only 3.5 eV above the corresponding π* resonance. (Fallon et al., 1993)

Besides the π* and σ* excitations, more valuable details of C-K spectra are noteworthy for understanding the electronic structure of carbon modifications. For one thing, it is quite clear that below the π* excitations there are the resonances of surface dangling bonds (Bressler et al., 1997; Fallon et al., 1993; Pappas et al., 1992). For another, the energy-loss intensities between the π* and σ* have complex origins as demonstrated schematically in Fig. 3.4.6. The π* electronic excitations will lead to an oscillation structure above the peak at 285 eV, which has been studied in terms of calculated density-of-states (DOS) or ELNES (Batson, 1993; Titantah & Lamoen, 2005) as well as the π*/σ* decomposition technique (Browning et al., 1991). Papworth et al. (2000) reported that this signal intensity could come from C-atoms in an intermediate state. The σ* peak may contribute to energy-loss intensities as low as 288 eV due to lifetime broadening (Batson, 1993) or a shifting to lower energy losses for *sp*^{3}-rich C-materials (Fallon et al., 1993). With respect to hydrogen, by fitting an EELS spectrum with a linear combination of several Gaussian functions, a Gaussian function centered at 287 eV, i.e. in between the two ones for the π* (blue curve) and σ* (red curve) peaks, has been attributed to the σ* state of C-H bonds in hydrogenated C-material (Fink et al., 1983; Silvaf et al., 1996); however it should be noted that this feature was also assigned to the higher lying π* oscillations of the *sp*^{2}-C in H-free carbon materials (Robertson & O'Reilly, 1987). Apart from the 287 eV excitations, additional energy-loss features such as C-H intensities below the σ* edge (289 eV) were shown to be present in this energy-loss range by X-ray fine structure spectroscopy techniques (Bressler et al., 1997; Buijnsters et al., 2009), but also excitations owing to phenolic (286.5 eV) and carboxylic (288.5 eV) functional groups, which are indistinguishable due to radiation damage and poor energy resolution in EELS (Alexander et al., 2008).

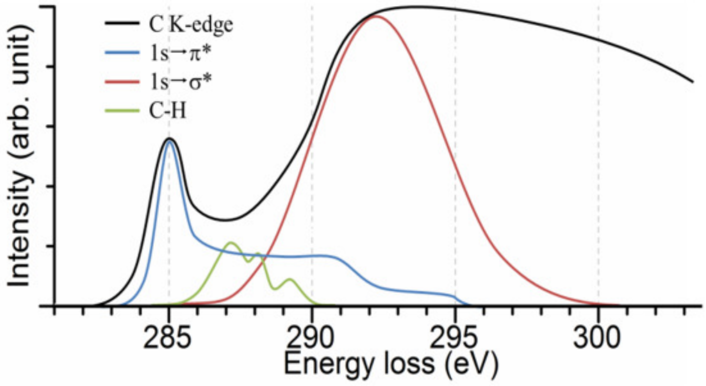

Fig. 3.4.6 A graphical presentation demonstrating the different components, i.e. π* (in blue), σ* (in red), and C-H (in green) excitations, of a C K-edge spectrum (in black).

3.4.4 EELS study of anisotropic materials: problems and solutions

An important problem associated with the quantification of *sp*^{2}-C is that the π and σ bonds in a-C are randomly orientated. On the contrary, crystalline graphite, which is commonly considered an ideal reference pure in *sp*^{2}-hybridizations, contains directional π bonds. To relate measurements of the C-K ELNES from C-materials of interest and from a reference, a suitable averaging technique is needed for the anisotropic graphitic carbon. This section and the next one (sections 3.4.4 – 3.4.5) will focus on the origin and solution of this problem.

Owing to its perfectly ordered structure highly ordered pyrolytic graphite (HOPG) is usually a preferable reference specimen for quantitative EELS analyses of the *sp*^{2}/*sp*^{3}-ratio of carbon materials. However, the anisotropic structure of HOPG is an obstacle to relate its near-edge fine structures with those recorded from the amorphous carbon materials under investigation.

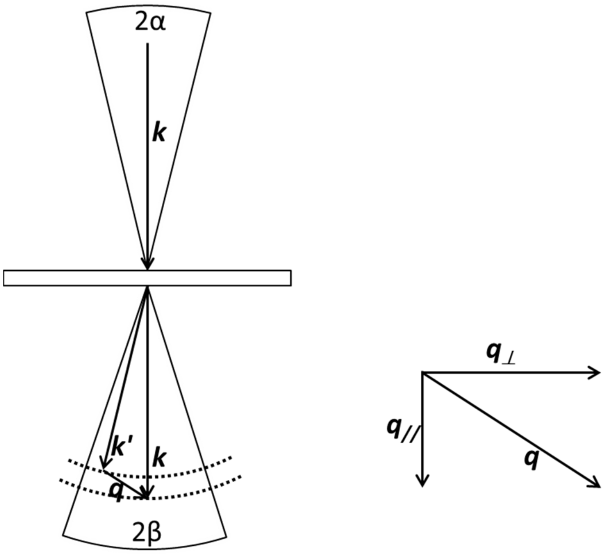

Fig. 3.4.7 Experimental geometry of EELS acquisition.

The reflection of the anisotropic nature of graphite into an EELS spectrum can be described by a single inelastic scattering event as presented in the following. The experimental geometry for an EELS spectrum is shown in Fig. 3.4.7. After being inelastically scattered by the sample, an incident electron with a primary momentum $\boldsymbol{k}$ will be collected by the detector with a momentum $\boldsymbol{k}'$. The energy loss and orientation deviation during the event can be revealed by the transferred momentum $\boldsymbol{q}$ with

$$\boldsymbol{q} = \boldsymbol{k}' - \boldsymbol{k}\,. \qquad 3.10$$

A resultant spectrum integrates a whole set of $\boldsymbol{q}$, defined by all incident $\boldsymbol{k}$ vectors within the convergence semi-angle α and all transmitted $\boldsymbol{k}'$ vectors within the collection semi-angle β. Each momentum vector $\boldsymbol{q}$ is composed of a parallel ($\boldsymbol{q}_{//}$) and a perpendicular ($\boldsymbol{q}_{\perp}$) component (cf. Fig. 3.4.7). For anisotropic materials, $\boldsymbol{q}_{//}$ and $\boldsymbol{q}_{\perp}$ usually correlates to excitations of different bonding configurations. Therefore, the different ways $\boldsymbol{q}_{//}$ and $\boldsymbol{q}_{\perp}$ are mixed and integrated is the origin of the orientation dependence of the spectrum. In other words, the particular shape or ELNES of the ionization edge, respectively, will vary with the crystal orientation as well as with the collection and convergence angles.

Specifically, for the situation where the incident ***k*** is parallel to the c-axis of graphite, the $\boldsymbol{q}_{//}$ carries information of π* transition, while the $\boldsymbol{q}_{\perp}$ is from σ* transition. Generally, as the specimen orientation or the angular range of ***k´*** changes, the weight factors of the overall π* transition and σ* transition components in the integrated spectrum are no longer preserved. As a consequence, for quantitative EELS of amorphous carbon, whose sp^2-bonds are randomly orientated, a suitable averaging technique is necessary to get rid of the orientation dependence for graphite.

A straightforward method is to use graphitized carbon black with small crystallites as a reference (Berger et al., 1988). By collecting spectra from a sufficiently large area, including a number of randomly orientated small crystallites, the final spectrum is rotationally averaged. However, the quality of such a reference spectrum relies on many conditions as, e.g., the orientation distribution of the crystallites and the degree of graphitization of the carbon black. Browning et al. (1991) put forward a prediction model to derive averaged ***q*** values from a single component $\boldsymbol{q}_{//}$ or $\boldsymbol{q}_{\perp}$. As an application of this result, it allows one to derive the average spectrum from a spectrum taken with the electron beam aligned along a specific zone axis. Also, C_{60} with rotational sp^2-bond configuration was studied as an alternative reference sample. However, an additional peak at 287 eV of the C-K edge required by the characteristic C_{60} molecular structure is controversial since this feature was similarly attributed to C-H bonds by other researchers (Papworth et al., 2000). Moreover, C_{60} is a material being highly sensitive to electron radiation of high energy (Egerton & Takeuchi, 1999), which makes it unsuitable as a reference in EELS studies. The solution of so-called "magic orientation" of a graphite specimen was reported to be 45° (Botton et al., 1995) or 54.7° (Sun & Yuan, 2005) away from the [001] zone axis, with the latter well established in extended X-ray absorption fine structure (EXAFS) and magic-angle spinning nuclear magnetic resonance (MAS-NMR) experiments. However, the tilting restriction of a common TEM sample holder limits the testing and application of this magic-orientation technique in TEM studies.

The magic-angle condition (MAC) is a technique using a certain collection semi-angle, for which the π* and σ* transitions are always averaged regardless of the specimen orientation. The collection semi-angle is then set to the magic angle (Jouffrey et al., 2004). The magic angle is a quantity that is determined by the fundamental inelastic scattering behavior (for comparison, see section 3.4.1). The corresponding deduction is based on the DDSCS, which is the probability of an incident electron being scattered into a direction described by a solid angle Ω and transferring an energy E and a momentum $\boldsymbol{q}$ to an electron of the excited atom,

$$\frac{\partial^2\sigma}{\partial E\partial\Omega}(E,\boldsymbol{q}) \,. \qquad 3.11$$

Since EELS measures a range of $\boldsymbol{q}$, determined by $\boldsymbol{k}$ and $\boldsymbol{k}'$, it is more efficient to use a partial differential cross section, i.e.

$$\frac{\partial\sigma}{\partial E}(E,\alpha,\beta) = \int_{\alpha,\beta} d\boldsymbol{q}\,\frac{\partial^2\sigma}{\partial E\partial\Omega}(E,\boldsymbol{q}) \,, \qquad 3.12$$

which integrates the DDSCS over the convergence angle and the collection angle. The specimen tilting coordinates can be further implemented into this expression. With a number of approximations like, e.g, the Born approximation and dipole approximation and subsequent treatments, it is possible to set the partial differential cross section irrelevant to the specimen tilting coordinate system, which gives equations of the beam energy, the energy loss, the convergence angle, and the collection angle. Furthermore, those equations could be solved and yield a special collection semi-angle to cancel the dependence of the specimen orientation, which depends only on those other scattering factors, namely the magic angle. It is noteworthy that the magic angle is independent of material properties.

Based on a premise of a parallel illumination ($\alpha = 0$ mrad) to simplify the algebra, the magic angle can be expressed in units of the characteristic scattering angle θ_E which is the half width at half maximum (HWHM) of the Lorentzian angular distribution of scattering,

$$\theta_E = \frac{E_m}{E_0}\cdot\frac{E_0 + m_e c^2}{E_0 + 2m_e c^2} \,, \qquad 3.13$$

where E_m is the mean energy loss (295 eV for C-K edge), E_0 is the energy of incident electron, m_e is the electron rest mass (511 keV/c^2), and c is the speed of light. The specific setup of collection semi-angle and convergence semi-angle is called magic-angle condition (MAC). Magic angle EELS (MAEELS) allows the quantitative analysis of carbon-based materials on a reference consisting of a cleaved HOPG TEM sample, with ideal crystalline structure and negligible sample preparation damage.

3.4.5 Magic angle: non-relativistic and relativistic calculations

Non-relativistic solutions predict a magic angle of $4\theta_E$ (Hebert-Souche et al., 2000; Hebert et al., 2004; Menon & Yuan, 1998), which however differs from experimental results. For example, for the C-K edge measured at 200 kV accelerating voltage ($\theta_E = 0.86$ mrad) the non-relativistic magic angle is 3.44 mrad, yet the experimental value is found to be $\beta_{magic} = 1.6$ mrad $= 1.86\ \theta_E$ (Daniels et al., 2003). Relativistic treatment explains the discrepancy for high accelerating voltages and indicates β_{magic}/θ_E accounts also for the electron energy (Hebert et al., 2006; Jouffrey et al., 2004). According to these authors, for parallel illumination the magic angle is defined by the equation,

$$\frac{1}{2}\left(ln(1+x^2)-\frac{x^2}{1+x^2}\right)=\frac{1}{2\gamma^2}\frac{2x^2}{1+x^2}, \qquad 3.14$$

where $x = \gamma\beta/\theta_E$, β is the collection semi-angle, and γ is the relativistic factor. The non-relativistic case is nicely integrated in this explication as $\gamma = 1$, whereby the magic angle is $3.98\theta_E$. For an accelerating voltage of 200 kV ($\gamma = 1.39$) the theoretical magic angle is reduced to 1.26 mrad for the C-K edge, which is much closer to the experimental value obtained by Daniels et al. (2003) than the non-relativistic value.

As it is well known, the relativistic effect is important when the electron velocity is close to that of light. Therefore a relativistically corrected theory fits better to the experimental results for high accelerating voltages (200 – 300 kV). However, the magic angle for the C-K edge at 100 kV is experimentally found to be $\beta_{magic} = 7.4$ mrad, which is even larger than the predicted non-relativistic value (Menon & Yuan, 1998). Detailed experiments were carried out with this fixed collection semi-angle, and convergent semi-angles up to 7 mrad were tested to be valid for achieving orientation independence (Ferrari et al., 2000). This setup has been applied to studies on various carbon materials at 100 kV (LiBassi et al., 2000; Yuan & Brown, 2000). Therefore, more consideration is still lacking for the full understanding of MAEELS experiments. Although, the MAC has been nicely predicted theoretically, for a better accuracy the use of an experimentally determined MAC is generally recommended.

3.5 Contamination and beam damage

Contamination and beam damage are the two common sorts of artifacts in electron microscopic techniques, which can deteriorate analyses in different ways, e.g., by degrading the image quality, changing the crystalline structure, and causing errors in thickness measurement. Particularly in the case of the present work, that deals with carbon modifications, these artifacts could lead to discrepancies in the sp^2-C quantification, as well as erroneous conclusions about mechanically driven amorphization for diamond, which are especially undesirable.

For this reason, in this work optimized EELS acquisition conditions were determined, ensuring only minimum or even absolutely no influence of such artifacts on the obtained quantitative results of sp^2/sp^3-ratios. Corresponding systematic studies yielded that it is best to perform EELS measurements of the C-K edge at 80 kV high voltage in the microprobe STEM mode with a dose rate of several 10 $e^-/\text{Å}^2\text{s}$. It has been verified that after a typical EELS acquisition time of 60 s, for both graphite and diamond the near-edge features of the C-K edge spectra, being typical for their crystal structure, are maintained and no trace of contamination or damage is observed for DLCs.

In the following sections of this subchapter, the events of contamination and beam damage observed in the early stage of this work will be summarized and discussed. A discussion about inevitable beam damage in TEM sample preparation is also included.

3.5.1 Contamination

Fig. 3.5.1 shows STEM HAADF images of a DLC specimen that was prepared by FIB milling. The layer with bright contrast on top of the DLC material is the Au protective layer. In these images the DLC appears darker in contrast due to its low atomic number. Firstly, EELS experiments were performed at 300 kV in the nanoprobe STEM mode. In both image regions, 20 C-K edge spectra were recorded in vertical direction with a 10 nm interval, covering a distance of 200 nm from the surface to the inner region. A line-profile series of low-loss spectra was taken with a horizontal distance of ~ 50 nm away from the measuring positions of the C-K edge spectra recorded prior to this. Here one can assume that within such a small distance, the horizontal variance of specimen thickness and other microstructure is negligible and, thus, the low-loss spectra can be used for the correction of plural scattering effects and the estimation of specimen thickness for the corresponding C-K edge spectra. In Fig. 3.5.1(a), the two lines visible in the DLC region, whose brighter contrast is indicative of an increased thickness, reveal the contamination produced by the line-profile EELS acquisition of the C-K edges as well as of the corresponding low-loss spectra. In Fig. 3.5.1(b), plasma cleaning was performed on the same specimen and afterwards the same routine of EELS experiments was carried out in an area nearby. From that STEM HAADF image it can directly be observed that no visible contamination was produced by the focused electron beam during the EELS acquisition.

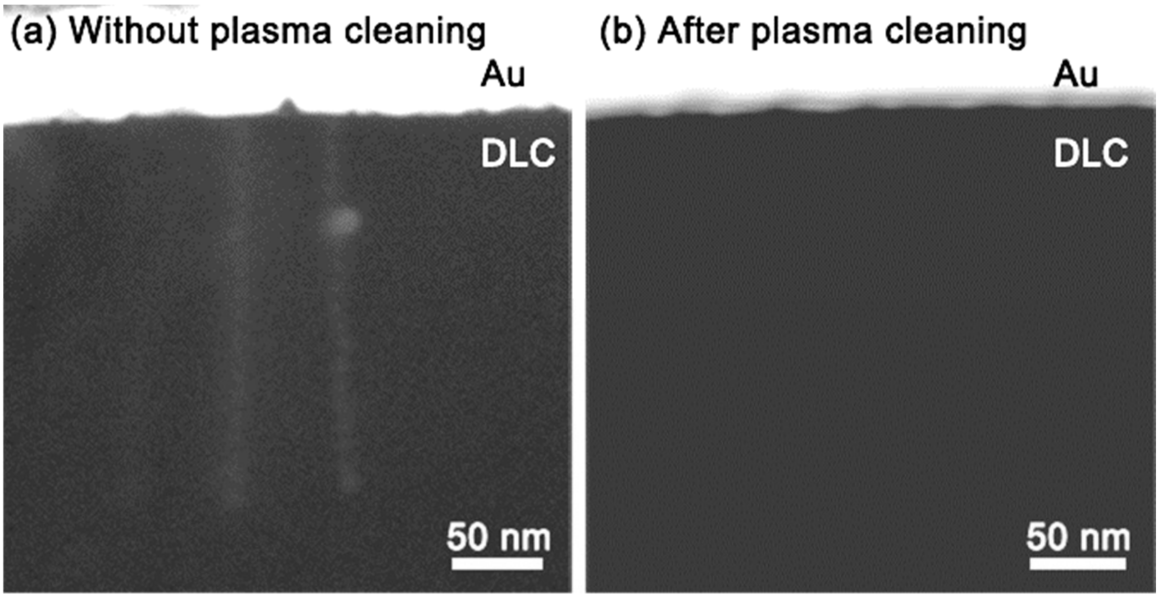

Fig. 3.5.1 STEM HAADF images of a DLC specimen prepared by FIB (a) without plasma cleaning and (b) after plasma cleaning and recorded after EELS line-profile acquisition at 300 kV.

Two series of C-K spectra, before and after plasma cleaning, covering a distance of 400 nm from the surface with a step size of 10 nm were recorded with the same routine. After data processing, i.e. background subtraction and plural scattering deconvolution, the maximum intensity of the π^* peak normalized by the integral intensity from 290.5 eV to 303 eV ($I_{\pi^*}/I_{\Delta E}$) was obtained from each C-K edge spectrum as a qualitative indication of the content of sp^2-C in the sample. Fig. 3.5.2(a) illustrates the $I_{\pi^*}/I_{\Delta E}$ as a function of the distance from the surface. The $I_{\pi^*}/I_{\Delta E}$ derived from the spectra before plasma cleaning shows a tendency of increase, which is from the near-surface (20 nm) to the inner area (40 nm) by a factor of ~ 5 %. After plasma cleaning, such an increase vanishes to the order of data fluctuation. Given by the low-loss spectra, the corresponding relative specimen thickness (t/λ) for each C-K edge spectrum is shown in Fig. 3.5.2(b) and Fig. 3.5.2(c). As seen from the two thickness line profiles, the specimen gets thinner from the surface to the inner regions. For the specimen before plasma cleaning, the inverse correlation between the $I_{\pi^*}/I_{\Delta E}$ values and the corresponding relative thickness is indicative of the error caused by the carbonaceous contamination layer, which is larger for originally thinner specimen areas.

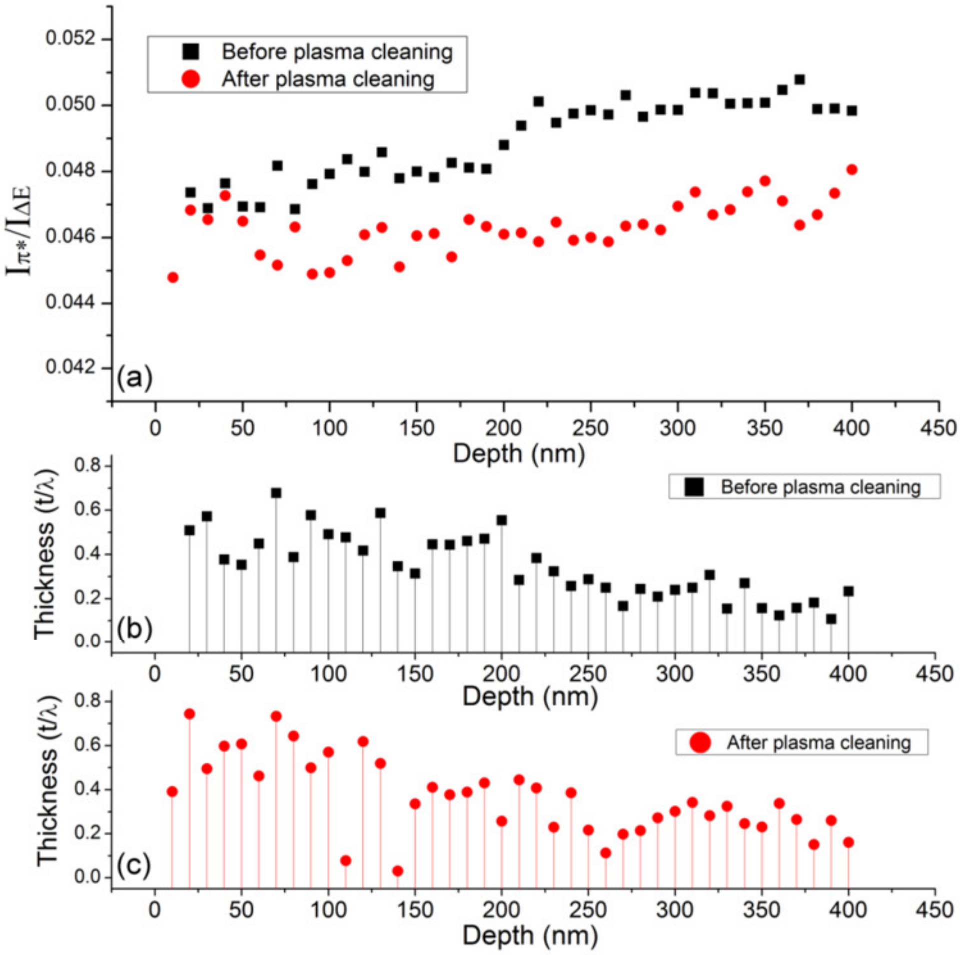

Fig. 3.5.2 (a) Normalized π* maximum intensity from two series of C-K edge spectra, before and after plasma cleaning, and corresponding relative specimen thickness for (b) before and (c) after plasma cleaning.

Contamination viewed in TEM is usually a carbonaceous layer generated by the interaction between the incoming electron beam and hydrocarbons, which stray in the path of the electron beam and get ionized, polymerized, and finally deposited as a carbon-rich film, unfortunately on the area of interest. The sources of these hydrocarbons could be

(i) present in the TEM chamber under imperfect vacuum conditions,
(ii) introduced by the specimen and the specimen holder adsorbed with hydrocarbon species,
(iii) emitted by the material under investigation.

There are several ways to reduce contamination. First of all, since any inappropriate handling of the specimen during the complex procedure of sample preparation could get hydrocarbon molecules adsorbed to the specimen, which becomes the source of contamination, even the sample itself is stable. Therefore, it is primarily helpful to reduce the time of exposure to the normal environment, meaning to transfer the specimen from one vacuum chamber to another very quickly.

Secondly, there are several external/attached facilities for TEM that can deal with contamination, e.g., a plasma cleaner, cold trap, and cooling specimen holder. For plasma cleaning, an oxygen-containing plasma is usually applied to decompose the hydrocarbons into small molecules and later-on to pump them away. In this process, the specimen as well as the sample holder is "cleaned". A cold trap or a cooling sample holder can also effectively reduce the contamination rate by cryoshielding or immobilizing the hydrocarbons.

Nevertheless, it has been demonstrated beneficial to work under microprobe STEM mode conditions instead of nanoprobe mode, giving up some spatial resolution of STEM. A nanoprobe, which applies a highly local electric field on the sampled area, induces chemical, thermal, and electrical gradients for the hydrocarbons, whose diffusion and polymerization will be enhanced dramatically, leading to strongly gathered contamination. On the other hand, a more broadened electron probe, i.e. a microprobe, will make the surface diffusion process much more harmless, resulting in a contamination not only less but also in the shape of thin layers, as schematically illustrated in Fig. 3.5.3 (Joy et al., 1986).

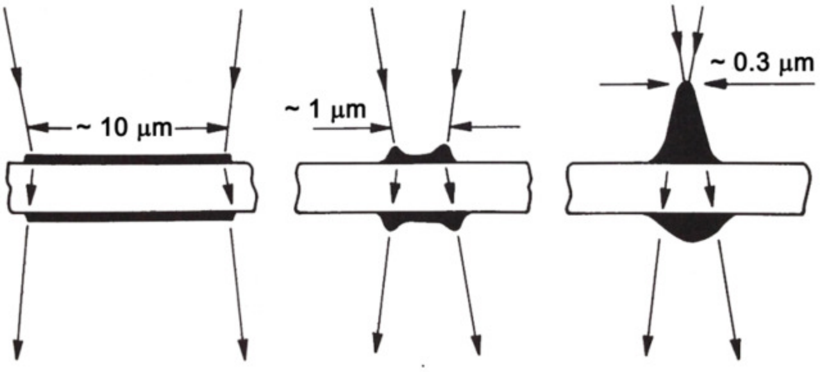

Fig. 3.5.3 A sketch of the change in the appearance of contamination with the change of beam size after Joy et al. (1986).

3.5.2 Beam damage in TEM

Materials made of light elements, such as carbon, are generally sensitive to high-energy electron bombardment. Apart from diamond, which is highly resistant to beam damage, different forms of damage were observed for DLC and crystalline graphite after EELS acquisition in nanoprobe STEM mode at 300 keV. For instance, in the case of DLC remarkable material loss was observed as shown in Fig. 3.5.4 by the holes at EELS acquisition sites. The image was taken under defocus condition so that the holes could be better recognized with a dark contrast. For this EELS/STEM experiment, the electron-beam convergence semi-angle was 17.6 mrad. Each hole was produced by a single acquisition of EEL spectra for 5 s, with an electron dose rate of 600 – 1000 $e^-/Å^2s$ amounting to a total electron dose of 3000 – 5000 $e^-/Å^2$. The holes have a diameter of several nm and would disappear until unrecognizable within 1 hour, which is possibly a self-recover process due to the inner stress in the DLC film. Moreover, structural degradation was directly observed for crystalline HOPG during EELS measurements, showing a gradual broadening of the sharp bump between 291 and 294 eV and fading of the π^* pre-peak in its C-K edge spectra.

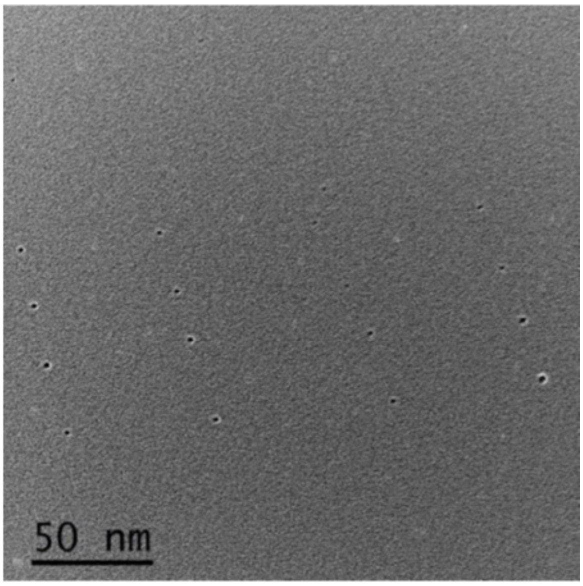

Fig. 3.5.4 Conventional TEM image showing the spots of material loss produced by EELS acquisition at 300 kV using a nanoprobe with a total electron dose of 3000 – 5000 $e^-/Å^2$.

Phenomena of electron-beam damage in C-materials have been investigated in a number of studies, e.g., in a review by Banhart (1999). Knock-on processes and radiolysis are considered as the two governing mechanisms, with the former being predominant in graphite.

Lowering the TEM accelerating voltage is an effective means for reducing the knock-on damage. In order to kick an atom out of its original site, the incident electron needs to transfer an energy larger than the displacement threshold energy (E_d) or surface binding energy (E_s) of the atom. For a specific target element, the maximum transferable energy of an incident electron is a function of the accelerating voltage (Fig. 3.5.5), which is for carbon ~ 70 eV at 300 keV and ~ 15 eV at 80 keV (D. B. Williams & Carter, 1996). Reports of E_d for carbon do scatter, e.g., 10 eV is reported (Cosslett, 1980) and 25 eV (Thrower & Mayer, 1978) for polycrystalline graphite, and 35 eV for diamond (Palmer, 1994). According to a review of irradiation effects in carbon nanostructures by Banhart (1999), for graphite, again, E_d is anisotropic, which is low along the c-axis (15 – 20 eV) and high in plane (higher than 30 eV). Displacement along the c-axis leads to the change of tetrahedral C-bonds formation and fading of the π^* pre-peak in the C-K ELNES. Therefore, in order to use graphite as a reference for 100 % sp^2-C, it is essential to operate the TEM at 80 kV or even below it for EELS measurements. In general, E_s is smaller than E_d, and thus material loss from surface regions may be inevitable even at 80 kV.

For radiolysis damage, which is an inelastic scattering process depending on the corresponding scattering cross section, it is advantageous to work at sufficiently low electron doses or low temperature, so that the damage could be negligible (Joy et al., 1986).

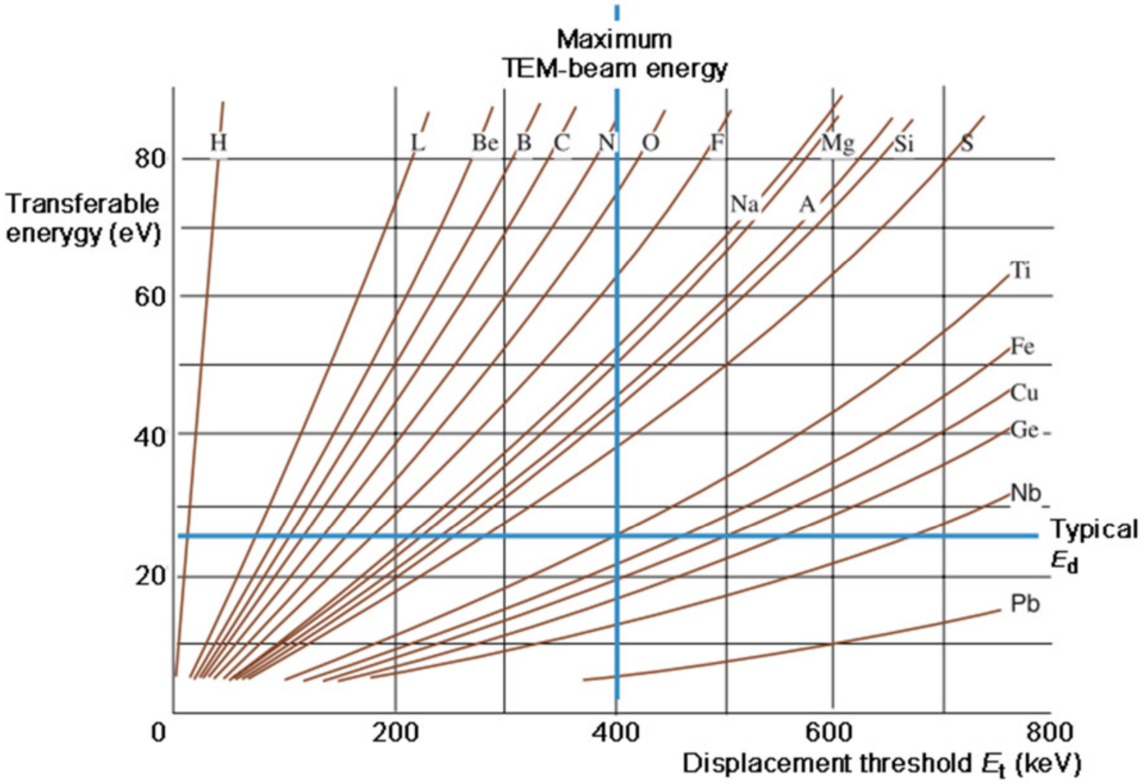

Fig. 3.5.5 Maximum transferable energy for a range of atoms as a function of the displacement-threshold energy after D. B. Williams and Carter (1996).

3.5.3 Beam damage by sample preparation

Both conventional and FIB-assisted TEM sample preparation techniques could still damage the structure to a certain degree, i.e. induce amorphization of crystalline diamond or alter the bonding configuration in a-C films, in spite of all the precautions already discussed in subchapter 3.1.

Table 3.1 Comparison of the ion-beam thinning approaches in the conventional and FIB sample preparation techniques

	Ion-species	Ion-energy	
		for thinning	for final polishing
Conventional	Ar^+-ion	3 keV	1 keV
FIB	Ga^+-ion	30 keV	5 keV

During the study of tribologically induced crystalline/amorphous phase transformations of diamond films, conventional cross-sectional TEM specimen could be prepared for comparison with FIB-lamella. As listed in Table 3.1, the conventional preparation uses Ar^+-ions with a lower atomic number and a lower ion-energy than those of Ga^+-ions in FIB milling. With such distinct differences in the preparation parameters, artifacts caused by the particular technique can be checked.

FIB-induced errors in sp^2-C quantification will be shown in this work not only correctable but also beneficial to provide a sample series containing different fractions of sp^2-C to test the EELS quantification method. This will be discussed in detail in Chapter 4.

4 TEM and quantitative STEM/ELNES studies of diamond-like carbon films

This chapter deals with the structural and chemical peculiarities, in particular with regard to chemical bonding phenomena, of diamond-like carbon (DLC) films. As already mentioned in subchapter 2.2, DLCs generally consist of mixture of sp^2- and sp^3-hybridized carbon atoms and their physical properties such as hardness and friction coefficient are mainly influenced by the specific sp^2/sp^3-C fraction, besides the contributions of hydrogen. As demonstrated in section 3.4.3, EELS in combination with STEM seem to be a suited means to determine this sp^2/sp^3-C ratio at high lateral resolution by performing quantitative analyses of the C-K edge ELNES. However, there are several practical issues to be solved before STEM/EELS can be successfully applied to this materials problem. The main point is that of an appropriate reference material which can be used as a standard for sp^2/sp^3-C fraction analyses of unknown DLC films under comparable experimental conditions. Usually, graphite is considered to be the best candidate for this purpose, but its anisotropic properties, also concerning the fraction of sp^2-hybridized carbon as a function of crystal orientation, make corresponding EELS applications difficult (see section 3.4.2). Likewise, the processing of EELS spectra to extract the information needed from near-edge fine structures has carefully to be revised.

For this reason, in the following both detailed considerations regarding EELS spectrum processing, particularly with respect to spectral contributions of π^* and σ^* excitations, and the experimental setup of the STEM/EELS system for optimized measuring conditions are presented. Moreover, besides the presentation of quantitative ELNES methods, the occurrence of FIB-induced material damage is treated and means for correction of these artificial contributions are shown. In more detail, in subchapter 4.1 some more information about the HOPG material, serving as reference for quantification of sp^2-C by ELNES analyses, is given. Also, two different DLC specimens are described, namely a hydrogenated amorphous carbon film (a-C:H) and a tetrahedral amorphous carbon film (ta-C). These two extremely differing DLCs were chosen to elucidate the influence of hydrogen bonds onto features of the C-K ELNES. Furthermore, in subchapter 4.2 the fundamental ideas are discussed how detailed features of the C-K edge ELNES can be used for quantification of the sp^2/sp^3-C ratio. In this context, artifacts in EELS spectra introduced by specimen damage owing to FIB milling are here demonstrated as well as possible means for their corrections. Subsequently, the experimental conditions for FIB preparation and characterization of the above-mentioned specimens are reported in subchapter 4.3. The corresponding obtained TEM and TEM/EELS results are presented in subchapter 4.4, where also such details will be shown like sp^2-C quantification and the applicability of the established FIB-damage-correction model. A discussion of all experimental findings is given in subchapter 4.5, whereas a summary of this part of work, i.e. referring to DLCs, is the final section (cf. subchapter 4.6).

4.1 Preliminary remarks on HOPG and DLC films

Usually, "typical" graphite, especially natural one, exhibits a quite imperfect structure with plenty of defects and impurity inclusions. From this point of view, the application of natural graphite as a reference for 100 percent of sp^2-hybridized C in STEM/EELS experiments is not recommended. But, there are a number of synthesis technologies available which allow the preparation of perfect graphite specimens to take advantage of its unique crystalline structure. Among them, the pyrolysis of organic compounds is one of the most common and effective preparation routes. Taking this into account, pieces (10 mm × 10 mm × 2 mm in size) made of highly ordered pyrolytic carbon (HOPG) of ZYA grade were bought from MikroMash™ and used for systematic quantitative EELS studies of DLC and diamond films (for the latter, see chapter 5). Grade ZYA means that the so-called mosaic spread amounts to 0.4 ± 0.1°, which stands for the highest quality HOPG. In general, the term "mosaic spread" characterizes the crystal perfection of HOPG specimens and originates from X-ray diffractometry. Pieces of HOPG are layered polycrystals, where each bulk polycrystal looks like a mosaic made of µm-sized single-crystalline grains. These grains are slightly disoriented with respect to each other, and the angle of deviation of the grain's boundaries from the perpendicular axis of the structure is a measure of the parallelism of grains, namely their mosaic spread.

From the ZYA-grade HOPG sample, two TEM specimens were prepared by FIB, one parallel to the graphite basal planes and the other in perpendicular direction to them.

Such specimens with a 90° deviation of graphitic *c*-planes are needed for the experimental determination of magic-angle conditions (MAC) for EELS in orientations near the [001] and [110] zone axes. A third HOPG TEM specimen was prepared by cleavage using a scotch tape and also studied by EELS, whose spectrum free of any FIB damage was used as the reference of pure sp^2-C for EELS quantification.

Quantitative STEM/EELS investigations were performed on two DLC films: one is hydrogenated amorphous carbon (a-C:H) containing a relatively large amount of sp^2-hybridized carbon, which was deposited on 100Cr6 steel by PECVD process with a hydrocarbon plasma. The thickness of the a-C:H film was 2.8 μm and the hardness and the Youngs modulus of the film were ~ 916 HV and ~ 73.8 GPa, measured by the film producers. The other is a tetrahedral amorphous carbon film (ta-C), which is rich in sp^3-hybridized carbon atoms.

4.2 Methodology of STEM/ELNES studies

4.2.1 Quantification of the sp^2-C content

The basic idea of making use of ELNES features for quantification is analogous to that of general EELS quantification. In detail, the intensity of a certain spectrum component is supposed to be the product of the number of available anti-bonding orbitals in the sampled area and the corresponding inelastic scattering cross-section. For a two-constituent system, i.e. consisting of two types of anti-bonding orbitals with densities of n_a and n_b, such relationship can be written as

$$\frac{I_a\,(E_0,\alpha,\beta,\Delta E)}{I_b(E_0,\alpha,\beta,\Delta E)}=\frac{n_a}{n_b}\cdot\frac{\sigma_a(E_0,\alpha,\beta,\Delta E)}{\sigma_b(E_0,\alpha,\beta,\Delta E)}. \qquad 4.1$$

In this equation, the intensities I and the partial cross-sections σ are all functions of the experimental parameters such as acceleration voltage E_0, convergence semi-angle α, and collection semi-angle β, as well as the way of extraction of the intensity (e.g. integration window ΔE in a two-window method). The partial cross-section ratio σ_a/σ_b must be either calculated or experimentally derived from a reference material under the same experimental conditions as for the material of interest.

The intensity-ratio (abbreviated as *I*-ratio, I_a/I_b) can directly be derived from the ELNES spectrum. Most methods of ELNES quantification reported in the literature primarily differ in the way to extract this *I*-ratio. In general, ELNES quantification methods can be divided into three groups:

(i) the classical two-window methods (Berger et al., 1988; Bruley et al., 1995; Cuomo et al., 1991),
(ii) functional fitting methods (Bernier et al., 2008; Papworth et al., 2000; Silvaf et al., 1996), and
(iii) model fitting methods (Bertoni & Verbeeck, 2008; Titantah & Lamoen, 2004a; Verbeeck & Bertoni, 2008).

The first method will be the main approach applied and discussed in this chapter. Methods involving functional fitting are also widely used in quantification of sp^2-C, one of which regarding fitting of the π* and σ* excitations by Gaussian functions is demonstrated in Fig. 4.2.1. In this figure, the C-K edge from graphite is processed by background subtraction and plural scattering removal and fitted by two Gaussian functions without any constrained parameters. The intensity-ratio $I_{\pi*}/I_{\sigma*}$ can be derived as the ratio between the integrations of both Gaussian functions. Further, the residual signal in the range near 287 eV could be fitted by a third Gaussian function, being part of the three-Gaussian-function method. Gaussian function fitting methods will be discussed and compared to the two-window methods in section 4.5.2, dealing with the discussion of the setup of the σ* and the π* integration windows. Specifically, the third method, which is based on the ELNES model simulation or calculation, respectively, is able to extract an *I*-ratio containing multiple information of partial cross-sections and experimental conditions, and thus enables a standardless quantification.

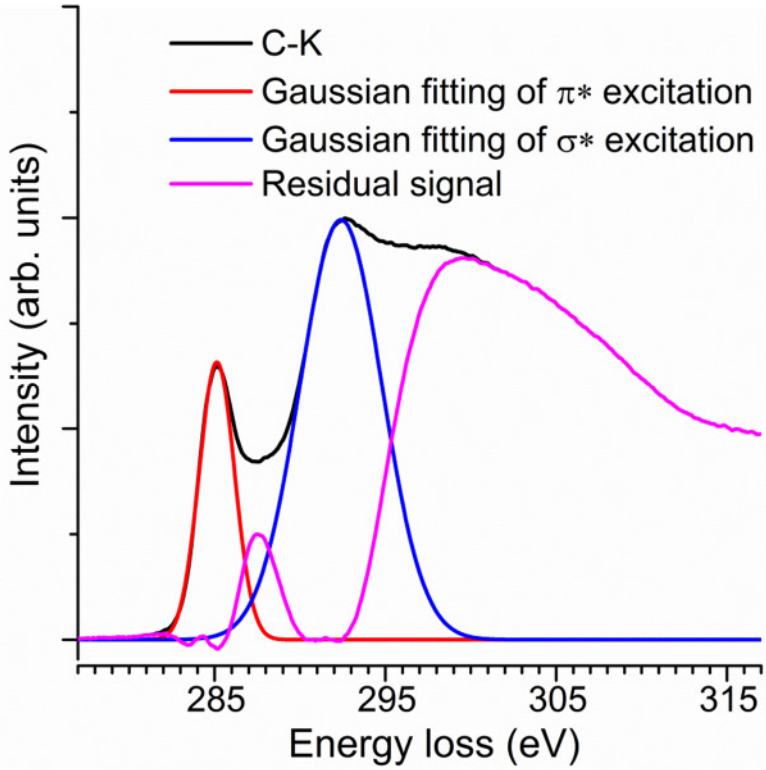

Fig. 4.2.1 C-K edge spectrum fitted by two Gaussian functions for the π* and σ* excitations, respectively.

The ratio n_a/n_b between the numbers of the anti-bonding orbitals of the two constituents is closely related to the corresponding concentration ratio c_A/c_B in the material. For example, in a certain type of C-material consisting of both sp^2-C and sp^3-C, all the π* orbitals are contributed by the sp^2-hybridized C-atoms, accompanied by three σ* orbitals, whereas each sp^3-hybridized C-atom contributes four σ* orbitals (see Fig. 2.1.1). To deal with this relationship, there are two main formalisms for sp^2-C quantification, one proposed by Berger et al. (1988) and the other by Cuomo et al. (1991), respectively. The main principles of these two methods were first put forward for a two-window method, and are transferrable to other methods, too. In the following, a brief introduction into the two formalisms is given as based on the two-window method.

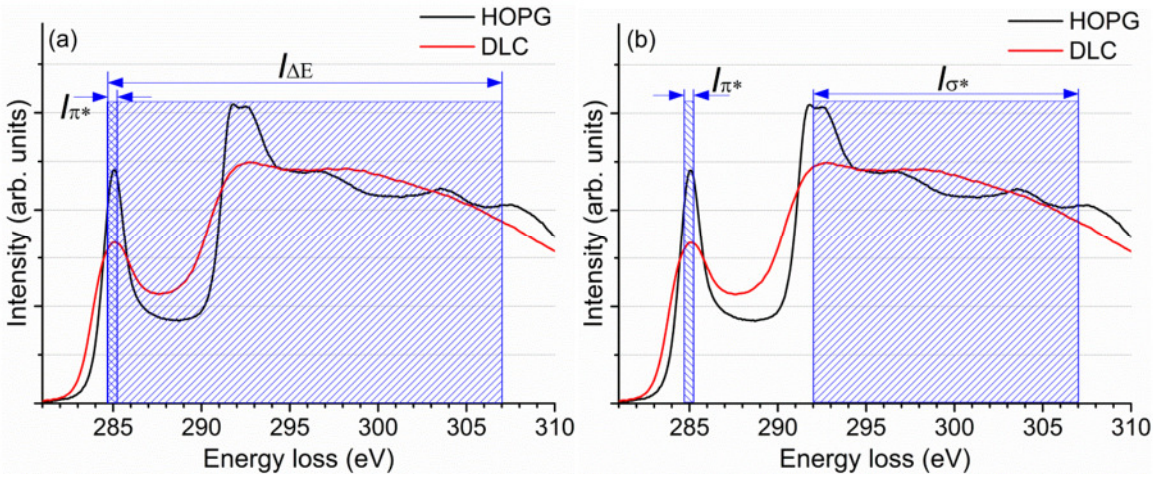

Fig. 4.2.2 Schemes of sp^2-C quantification of DLC by referring to HOPG, using two-window methods suggested by (a) Berger et al. (1988) and (b) Cuomo et al. (1991).

According to Berger et al. (1988), as is illustrated in Fig. 4.2.2(a), the intensity of the π* peak is integrated over an energy window $I_{\pi*}$ and normalized by the integral intensity over a large energy window encompassing both the π* peak and the σ* peak ($I_{\Delta E}$) for both the unknown C-material and the reference, i.e. HOPG, which is

$$\frac{I_{\pi^*}}{I_{\Delta E}}. \tag{4.2}$$

This I-ratio is assumed proportional to the ratio between the number of π* orbitals and the total number of π* and σ* orbitals and can be expressed for a suitable reference specimen of pure sp^2-C and for an unknown C-material as

$$\left(\frac{I_{\pi^*}}{I_{\Delta E}}\right)_{reference} = k \cdot \frac{1}{4}, \tag{4.3}$$

and

$$\left(\frac{I_{\pi^*}}{I_{\Delta E}}\right)_{unknown} = k \cdot \frac{x}{4} \ \left(sp^2\ \%_{unknown} = x\right). \qquad 4.4$$

where *k* is the partial cross-section ratio between a π^* transition cross-section and the mean cross-section of all kinds of transitions (π* and σ*) in the material and is assumed to be a constant under a certain setting of experimental conditions and energy windows. Consequently, *x* could be derived by combination of these two equations as

$$sp^2\ \% = \left(\frac{I_{\pi^*}}{I_{\Delta E}}\right)_{unknown} \Big/ \left(\frac{I_{\pi^*}}{I_{\Delta E}}\right)_{reference}. \qquad 4.5$$

Alternatively, as shown in Fig. 4.2.2(b) an *I*-ratio between the integrals of intensities of the π* peak and the σ* peak (Cuomo et al., 1991) can also be used, written as

$$\frac{I_{\pi^*}}{I_{\sigma^*}}. \qquad 4.6$$

This *I*-ratio is considered proportional to the ratio between the numbers of empty π^* and σ* orbitals, with a pre-factor *k´*, which is the partial cross-section ratio between a π^* transition and a σ* transition. For example, for a reference specimen pure in sp^2-C this ratio is

$$\left(\frac{I_{\pi^*}}{I_{\sigma^*}}\right)_{reference} = k' \cdot \frac{1}{3}. \qquad 4.7$$

For an unknown C-material containing sp^2-C with a fraction of *x*, the ratio can be written as

$$\left(\frac{I_{\pi^*}}{I_{\sigma^*}}\right)_{unknown} = k' \cdot \frac{x}{4(1-x)+3x} = k' \cdot \frac{x}{4-x}. \qquad 4.8$$

Combining the equations 4.7 and 4.8 will remove the dependence on *k'* and the sp^2 % in the unknown C-material can be expressed as

$$x = \frac{4\left(\frac{I_{\pi^*}}{I_{\sigma^*}}\right)_{unknown} / \left(\frac{I_{\pi^*}}{I_{\sigma^*}}\right)_{reference}}{3 + \left(\frac{I_{\pi^*}}{I_{\sigma^*}}\right)_{unknown} / \left(\frac{I_{\pi^*}}{I_{\sigma^*}}\right)_{reference}}. \qquad 4.9$$

These two formalisms, of which one uses an *I*-ratio in form of $I_{\pi^*}/I_{\Delta E}$ and the other uses I_{π^*}/I_{σ^*}, could be well connected for the two extreme cases of carbon in form of pure diamond or graphite:

$$\frac{\left(\frac{I_{\pi^*}}{I_{\Delta E}}\right)_{diamond}}{\left(\frac{I_{\pi^*}}{I_{\Delta E}}\right)_{reference}} = \frac{\left(\frac{I_{\pi^*}}{I_{\sigma^*}}\right)_{diamond}}{\left(\frac{I_{\pi^*}}{I_{\sigma^*}}\right)_{reference}} = 0\,; \qquad 4.10$$

$$\frac{\left(\frac{I_{\pi^*}}{I_{\Delta E}}\right)_{graphite}}{\left(\frac{I_{\pi^*}}{I_{\Delta E}}\right)_{reference}} = \frac{\left(\frac{I_{\pi^*}}{I_{\sigma^*}}\right)_{graphite}}{\left(\frac{I_{\pi^*}}{I_{\sigma^*}}\right)_{reference}} = 1\,, \qquad 4.11$$

where both formalisms give the sp^2 % as 0 and 1, respectively.

In order to better understand these two formalisms, which generally give different quantification results, we introduce here a third formalism, where two energy windows are positioned on the π^* and σ^* peaks and a new type of intensity-ratio is defined as,

$$\frac{I_{\pi^*}}{I_{\pi^*}+I_{\sigma^*}}. \qquad 4.12$$

For this new method, the window settings are the same as those used for I_{π^*}/I_{σ^*}, while the quantification formulas are similar to those in the formalism using $I_{\pi^*}/I_{\Delta E}$, yielding:

$$\left(\frac{I_{\pi^*}}{I_{\pi^*}+I_{\sigma^*}}\right)_{reference} = k'' \cdot \frac{1}{4}, \qquad 4.13$$

$$\left(\frac{I_{\pi^*}}{I_{\pi^*}+I_{\sigma^*}}\right)_{unknown} = k'' \cdot \frac{x}{4}, \qquad 4.14$$

$$x = \left(\frac{I_{\pi^*}}{I_{\pi^*}+I_{\sigma^*}}\right)_{unknown} \Big/ \left(\frac{I_{\pi^*}}{I_{\pi^*}+I_{\sigma^*}}\right)_{reference}. \qquad 4.15$$

Here it should be pointed out that all the above-mentioned three formalisms give the atomic fraction of sp^2-C (sp^2 %) instead of the sp^2/sp^3-ratio, which is irrelevant for the particular choice of I-ratio. The method using I_{π^*}/I_{σ^*} is the approach that has been mainly applied to quantitative STEM/EELS studies in this work, i.e., for testing the specific setting of the two energy windows for signal integration in sections 4.4.5 and 4.4.7, as well as relevant discussion in section 4.5.2. The method using $I_{\pi^*}/I_{\Delta E}$ will be applied and compared in sections 4.4.9 and 4.5.3, where a few problems contained in this formalism will be discussed.

4.2.2 Model for correcting contributions of FIB-induced damage

In general, STEM/EELS locally probes in detail the electronic structure and chemical bonding configuration of the material under investigation, and any damage occurring already during sample preparation or later under electron bombardment will directly affect the obtainable EELS results. For carbon materials, such effects are particularly of interest when ELNES features are used to quantify the sp^2/sp^3-ratio.

In this context, amorphization by TEM sample preparation has indeed been observed and verified for DLCs in our experiments, and thus could be a source of error in EELS quantitation. An ingenious way to get rid of it is the use of a free-standing DLC thin film (< 100 nm) readily suitable for direct TEM investigation. This can be achieved by film deposition on water soluble crystals (e.g. NaCl, Bhushan et al. (1992)) or Si substrate which is later on resolved/etched away in water or a corrosive solution (e.g. HF and HNO_3, (Yamamoto et al., 1998)). However, for industrial DLC applications the layer thickness is commonly larger than only 100 nm and, in addition, substrates like NaCl and Si are usually not used in real application.

For several reasons FIB is nevertheless a preferable technique to prepare a cross-sectional TEM specimen from DLC layers. For instance, the cross-section view of the layer structure is of more interest than the plan-view one, e.g. allowing to study film-growth mechanisms and thereby excluding interferences by the surface layer which is a post-deposit from remnant gas. Furthermore, FIB with its site selectivity is capable to show material changes, e.g. phase transitions, after some material treatment such as indentation and tribological testing. Unfortunately, during FIB thinning the high-energy Ga^+ beam may have damaged the original structure at the milled surfaces of the TEM cross-section specimen. Damaged cover layers of amorphous carbon can form with modified bonding configurations compared to inner DLC regions, leading to errors in quantitative EELS/ELNES measurements of the sp^2-content.

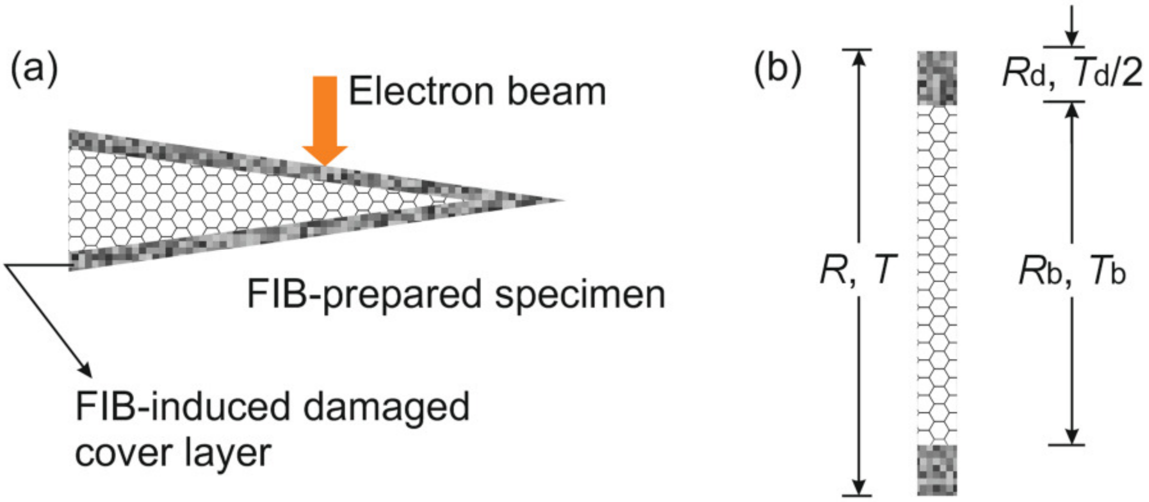

Fig. 4.2.3 (a) Influence of FIB-induced damaged cover layers in determining the sp^2-fraction by quantitative EELS; (b) material column interacted with the electron beam (overall bond configuration R and thickness T, measured by EELS), composed of damaged layers on both sides (bond configuration R_d and thickness T_d) and the bulk material (bond configuration R_b and thickness T_b)

As discussed in section 4.2.1, the I-ratio or sp^2 % derived from a C-K edge spectrum is representative for the bond configuration throughout the whole material column defined by illuminated sample region and can be considered as a linear combination of the bulk contribution and those of the damaged layers on both sides (cf. Fig. 4.2.3). Thus, it can be written as

$$R = R_b + (R_d - R_b) \cdot T_d \cdot \left(\frac{1}{T}\right), \qquad 4.16$$

where R denotes the I-ratio for HOPG or sp^2 % for DLCs, and T indicates the thickness or relative thickness (t/λ) of the overall specimen; subscripts d and b of R and T represent damaged region and bulk region in the material column. Ignoring the local difference and consequently assuming T_d, R_d and R_b to be constant, a linear relationship between R and ($1/T$) could be derived and the intercept could be R_b. Collecting spectra at different sample thicknesses T allows to extract R_b.

This concept is not only capable of correcting the error caused by the damaged layer, but also those C-K ELNES spectra recorded from one and the same carbon layer and yet showing different fractions of sp^2- and sp^3-C, where thus these differences are caused by sample-thickness variations. Detailed application examples for the correction of sp^2-C quantification data for a-C:H and ta-C films are given in section 4.4.8.

4.3 Experimental setup

The surface morphology of the as-prepared a-C:H and ta-C films was first viewed by scanning electron microscopy in an SEM of the type LEO 1530 .

For HOPG and DLC samples, FIB preparation of TEM lamellae followed a standard lift-out technique. In this process, for specimen protection a Pt/C-layer was deposited in the FIB prior to any milling. 30 keV Ga^+-ions were used for coarse thinning, and during the final stage of polishing the ion-beam energy was decreased to 5 keV to minimize specimen damage. Only for DLCs, an additional gold layer of approximately 100 nm in thickness was deposited on the film before it is inserted into the FIB chamber, so that its surface can later be distinguished from the protective Pt/C-layers.

TEM imaging was performed using an FEI Titan^3 80-300 microscope operated at 300 kV. This TEM is equipped with a Cs-image corrector in the imaging lens system allowing a resolution of 0.08 nm for HRTEM imaging. For EELS acquisition, the FEI Titan^3 80-300 microscope is equipped with a GATAN imaging energy filter (GIF) Tridiem model 865 HR and a 4 mega-pixel CCD camera as detector. In all STEM/EELS experiments, the Titan microscope was operated at 80 kV in the microprobe STEM mode, so that beam damage and contamination can be minimized or even prevented during STEM/EELS investigations. The combination of the convergent illumination and spectrometer acceptance semi-angles was always confined to the magic-angle condition (MAC) in order to obtain reliable quantitative EELS results (cf. section 3.4.5), i.e. without strong dependency from crystal orientations as known from anisotropic graphite. The energy dispersion of the Tridiem model 865 HR was set to 0.1 eV/channel. The duration of a single EELS acquisition of the C-K edge was 1 s, with a typical electron dose rate of several 10 $e^-/Å^2s$. In each case, the final C-K ELNES spectrum was obtained by summing up of ~ 100 single spectra. No structure variation was observed during the STEM/EELS acquisition. Low-loss spectra were obtained under a similar setup, except that the electron dose rate and acquisition time were largely reduced to prevent any beam damage of the scintillator in front of the CCD chip. The energy resolution was of the order of 0.6 – 0.7 eV measured from the FWHM of the zero-loss peak. During EELS acquisition, the HOPG specimens were oriented close to a certain zone axis (ZA) and channeling effects were avoided by tilting the specimens by 5 – 10° away from it. In contrast to that, the DLC specimens must not be tilted at a certain angle because of their amorphous structure. C-K edge spectra follow a standard post-acquisition data processing, i.e. background subtraction and plural scattering removal by Fourier-ratio deconvolution with the relevant low-loss spectra. Usually, the sensitivity of EELS for element detection is better than 1 at. % (see the discussion related to Fig. 3.4.3).

4.4 Results

4.4.1 TEM imaging of HOPG

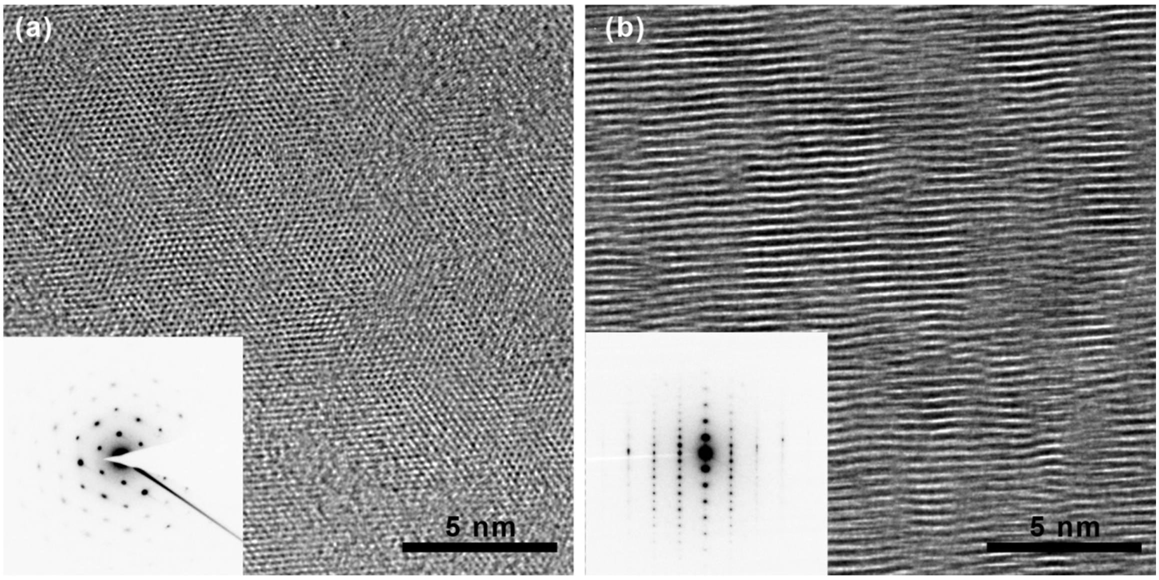

Fig. 4.4.1 HRTEM images of HOPG specimens taken along (a) the [001] zone axis and (b) [100] zone axis with insets showing the relevant diffraction patterns.

HRTEM imaging was performed on two HOPG samples, which were prepared in orientations close to the [001] zone axis (cleaved) and [100] zone axis (FIB-prepared), respectively. For HRTEM, the Titan microscope was operated at 300 kV and structural degradation of the graphite lattice could be observed during the imaging process, seen from the amorphization during the recording of a sequence of HRTEM images and diffraction patterns. This structural damage was more severe for the HOPG specimen prepared perpendicular to the graphite basal planes, i.e. for TEM imaging along the [100] ZA.

Nevertheless, in HRTEM images taken with a short beam exposure the graphite lattice can be seen clearly. Corresponding HRTEM images and related diffraction patterns from HOPG along the [001] and [100] zone axes are shown in Fig. 4.4.1. The hexagonal atomic arrangement of the graphite basal plane is well seen in Fig. 4.4.1 (a), whereas Fig. 4.4.1 (b) shows the graphite basal planes in cross-section view. In the latter, the lattice seems to be highly disturbed possibly due to the beam damage, with a scatter in the lattice distance of 0.330 – 0.345nm.

4.4.2 C-K ELNES of HOPG

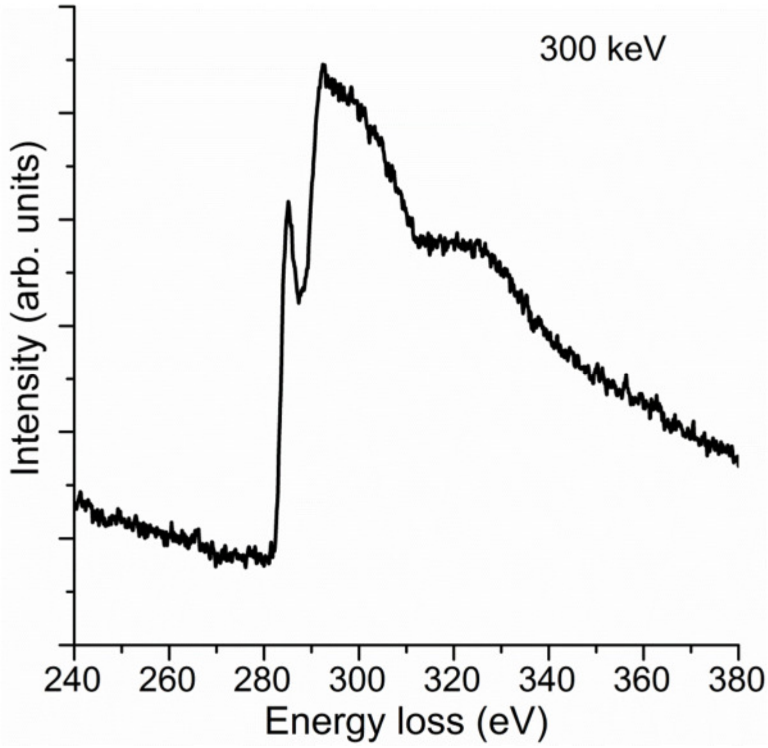

Fig. 4.4.2 C-K edge spectrum from HOPG recorded at 300 keV primary electron energy. The nominal collection semi-angle is 0.85 mrad (defined by a camera length of 185 mm and an EELS spectrometer entrance aperture of 1 mm in diameter), and the nominal convergence semi-angle is 0.34 mrad.

Fig. 4.4.2 shows a C-K ELNES spectrum of an HOPG specimen, close to the [001] zone axis. The microscope was operated at 300 kV and the EELS acquisition condition was close to the MAC, where the collection angle is theoretically predicted by Jouffrey et al. (2004) to be 0.62 mrad for parallel illumination at 300 keV. The acquisition duration was 1 s, which is responsible for the noise in this spectrum. The spectrum shows a pronounced π* pre-peak at 285 eV, followed by a nearly featureless σ* peak. Oscillations in the σ* excitation, which are characteristic of crystalline graphite (cf. the spectrum in Fig. 3.4.4), are absent, possibly due to the beam damage from the incident high-energy electrons.

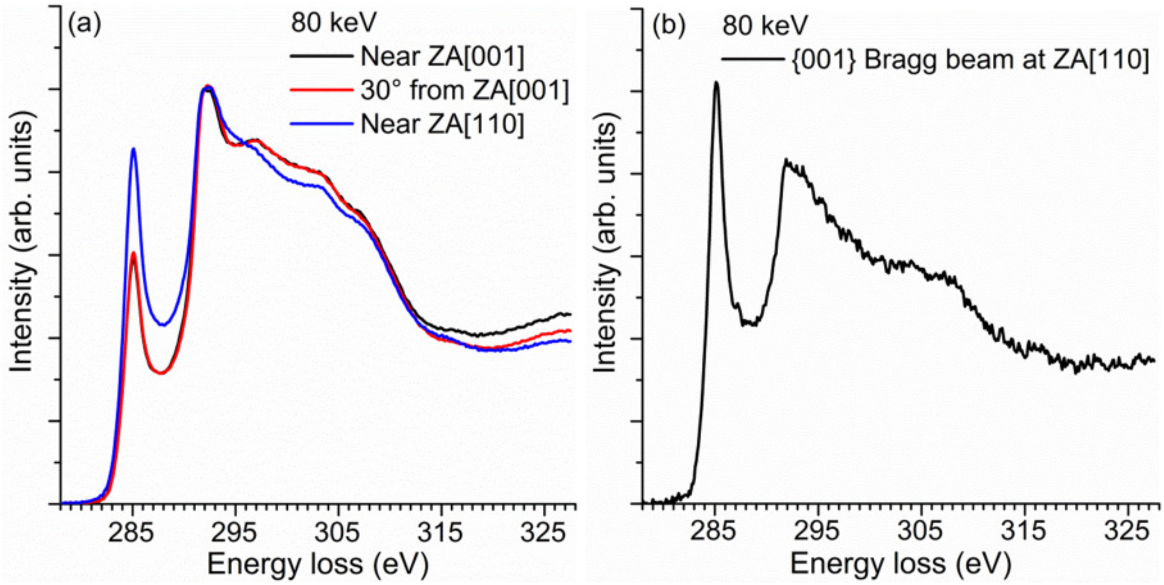

Fig. 4.4.3 C-K ELNES spectra from HOPG collected at β = 8.34 mrad, α = 2.0 mrad for 80 keV electrons (a) at different orientations without objective aperture; (b) with the {001} Bragg beam selected by an objective aperture.

Fig. 4.4.3 shows C-K edge spectra collected with β = 8.34 mrad (defined by a camera length of 73 mm and an EELS spectrometer entrance aperture of a diameter of 2.5 mm), α = 2.0 mrad for 80 keV incident electrons in microprobe STEM mode. The spectra show a good signal-to-noise ratio, and the characteristic features for crystalline graphite can be recognized. In the absence of any objective aperture (Fig. 4.4.3(a)), the intensity of the π* pre-peak is independent of the orientation from near [001] zone axis to 30° away from that. However, if the beam is aligned close to the [110] zone axis and the {001} Bragg beams (kinematically forbidden but show up because that the sample was rather thick) contribute to the resultant spectrum, the π* peak is more pronounced. By selecting solely the {001} Bragg beams by the objective aperture for EELS acquisition, the intensity of the π* peak is even stronger (Fig. 4.4.3(b)). It is noteworthy that the application of the objective aperture could have changed the collection angle of EELS spectrometer. However, the Bragg beams could still be the source of the erroneously pronounced π* pre-peak in the spectrum taken close to [110] zone axis. Therefore, Fig. 4.4.4 shows C-K edge spectra from three different HOPG specimens taken under a similar condition as that for the spectra in Fig. 4.4.3, with an objective aperture of 30 μm in diameter applied to select the zero-order beam.

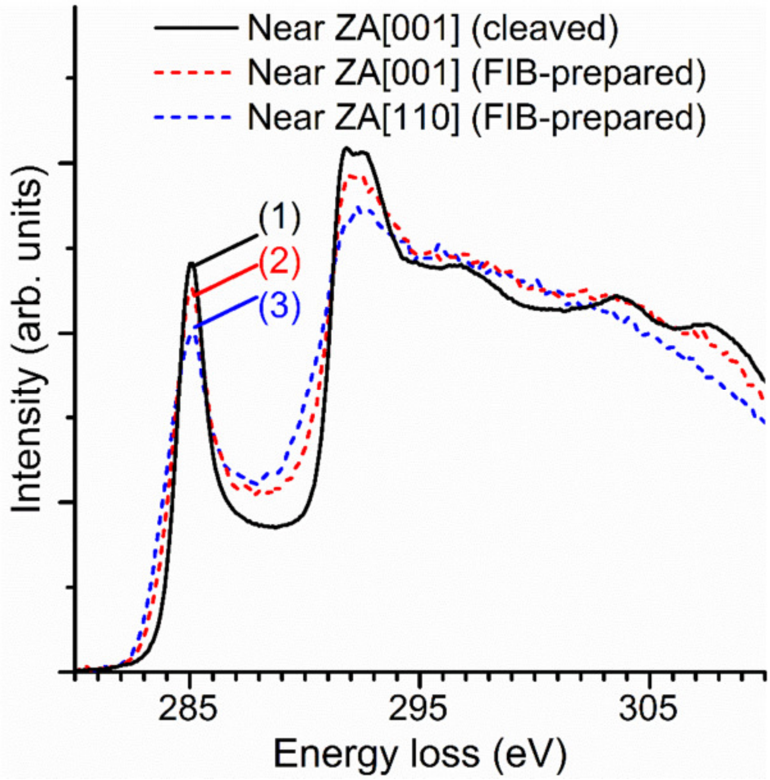

Fig. 4.4.4 C-K ELNES spectra taken under magic-angle condition from HOPG specimens (1) prepared by scotch tape cleavage; (2) prepared by FIB milling parallel to the graphite basal layers, and (3) prepared by FIB milling perpendicular to the graphite basal layers.

In Fig. 4.4.4 the background and plural scattering were customarily removed for each spectrum. Each individual spectrum exhibits more or less pronounced characteristic features of the C-K ELNES as known from graphite.

In detail, spectra labeled (1) and (2) were recorded from HOPG specimens of a similar orientation, but obtained by different TEM sample preparation techniques, namely scotch-tape cleavage and FIB-preparation, respectively. Spectra (2) and (3) were collected from two FIB-prepared TEM specimens, one prepared perpendicular and the other parallel to the graphite basal planes, respectively. Spectrum (1) from the cleaved HOPG specimen shows the sharpest π^* pre-peak and σ^* peak among the three depicted spectra. All the σ^* main peaks are seen with a sharp maximum at ~ 292 eV, followed by several oscillations being indicative of the ordered crystal graphite structure. The three spectra were normalized to their integral intensities between 292 – 307 eV, and the maximum intensities of the π^* pre-peaks from spectra (1) to (3) show a slight reduction, accompanied by peak broadening.

4.4.3 Correction of FIB-induced damage for HOPG

The I_{π^*}/I_{σ^*} intensity ratios of the C-K ELNES spectra (1) – (3) in Fig. 4.4.4, which were obtained by a π^* integration window of 284.7 – 285.3 eV and a σ^* integration window of 292 – 307 eV, are summarized in Table 4.1. Their relative thicknesses (t/λ) calculated from their corresponding low-loss spectra (not shown) are also included. The relative thickness t/λ ranges from 0.35 for the cleaved HOPG to 0.98 for the FIB-prepared HOPG standard orientated along the [110] zone axis, which, obviously, is a great difference. Especially, for $t/\lambda = 0.98$ a high degree of plural inelastic scattering events can be expected, complicating any EELS quantification. As can be seen, the ratios I_{π^*}/I_{σ^*} of spectra (2) and (3) are 15 % and 8 % smaller than that of spectrum (1) that was recorded from cleaved HOPG near to the [001] ZA. However, making use of the relationship for correcting the FIB-induced change in the sp^2/sp^3-ratio (cf. equation 4.16), the correspondingly modified evaluation of spectra (2) and (3) results in an R_b value of 0.0474, which is only 3 % different from that of spectrum (1). Thus, it is clearly demonstrated that the correction model established and discussed in section 4.2.2 indeed enhances the reliability of the applied ELNES quantification procedure.

Nevertheless, it can be supposed that the intensity-ratio $I_{\pi^*}/I_{\sigma^*} = 0.0461$ from the cleaved graphite is the most trustable and, therefore, it has been used as reference for all STEM/EELS studies performed on DLC and worn diamond films within the present work.

Table 4.1 I_{π^*}/I_{σ^*} ratios derived from C-K ELNES spectra in Fig. 4.4.4 and corresponding relative thicknesses (t/λ) derived from low-loss spectra.

Specimen	**R (I_{π^*}/I_{σ^*})**	**t/λ (Relative thickness)**
(1) Near [001] ZA (cleaved)	0.0461	0.35
(2) Near [001] ZA (FIB-prepared)	0.0393	0.58
(3) Near [110] ZA (FIB-prepared)	0.0426	0.98

4.4.4 SEM and conventional TEM imaging of a-C:H

First of all, before any TEM preparation the surface topography of the as-deposited a-C:H specimen was imaged by scanning electron microscopy (SEM). Fig. 4.4.5 shows typical SEM micrographs which were recorded at different magnifications at 5 kV by means of the in-lens secondary-electron detector of the LEO 1520 microscope. Evidently, the a-C:H film presents a cauliflower-like surface with round swells piled on each other. The diameter of those swells ranges from several 100 nm to several µm.

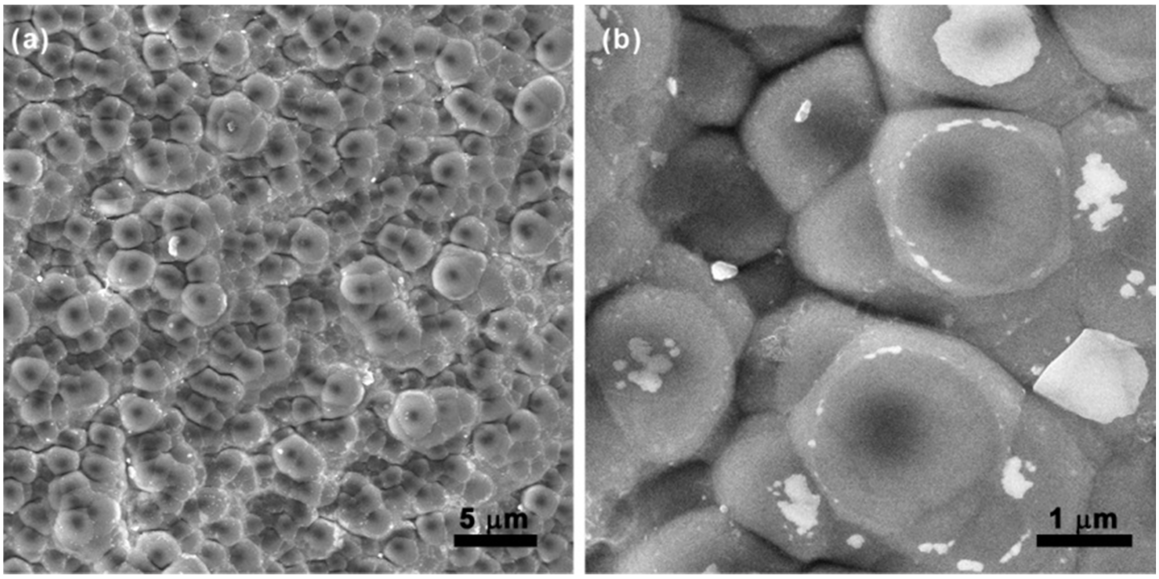

Fig. 4.4.5 SEM images of the topography of the as-deposited a-C:H film, clearly showing a cauliflower-like surface: (a) overview image, (b) detailed image taken at higher magnification.

After SEM inspection, a thin gold layer was deposited onto the DLC specimen to prevent its surface from any damage caused by FIB milling. A subsequently FIB-prepared TEM cross-section specimen is depicted in Fig. 4.4.6, where Fig. 4.4.6(a) gives an overview at low magnification. Here, the Au layer visible on top of the DLC specimen delineates the original surface of the carbon layer. Inside the DLC layer, the structure imaged in cross-section view is homogeneous. The high-resolution TEM image of Fig. 4.4.6(b) as well as the corresponding diffractogram obtained by fast Fourier transformation (FFT) in Fig. 4.4.6(c) reveal its amorphous structure. In the HRTEM image there is no contrast feature hinting at any crystallinity.

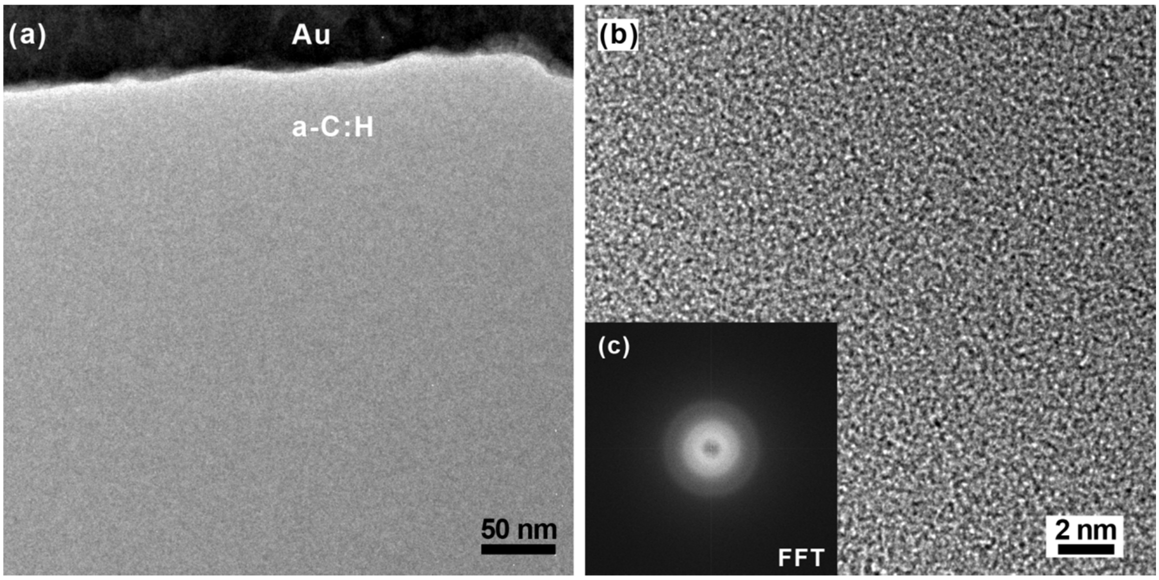

Fig. 4.4.6 (a) Typical cross-section TEM and (b) HRTEM images of the a-C:H film with inset (c) of the corresponding diffractogram obtained by FFT.

4.4.5 EELS data processing and ELNES quantification of a-C:H

Fig. 4.4.7(a) shows two enlarged low-loss spectra, superimposed on each other, which were recorded from different regions of the a-C:H film. For both spectra the maximum intensities of the zero-loss peaks were normalized to 1 and only 1/10 of the total intensity of the zero-loss peaks are shown in this figure. The energy resolution measured as the ZLP's FWHM (not included in the figure) amounts to 0.6 eV. Moreover, the visible plasmon excitations are rather noisy which is due to their low intensities compared to that of the ZLP and due to the short acquisition time chosen to prevent any possible beam damage of the CCD camera. Despite the bad signal-to-noise ratio and the strong influence of the high-energy ZLP tail, two small bumps can be seen just above the zero-loss peak at ~ 5 eV. These local intensity maxima can be attributed to the excitation of π plasmons. The σ plasmon peak (~ 23 eV) of spectrum (1) shows a higher amplitude than that of spectrum (2), which is indicative of a larger thickness of the sampled volume. For both spectra the σ plasmon peaks are centered at ~ 23 eV and have an onset at ~ 16.5 eV. Relative thicknesses (t/λ) were derived based on the equations 3.6 and 3.7 from these two spectra to be 0.74 and 0.45, respectively. In Fig. 4.4.7(b) the zero-loss peaks are removed so that only the remaining inelastic intensities are shown, where the two π plasmons of low intensity are better recognized and measured both centered at ~ 5.5 eV.

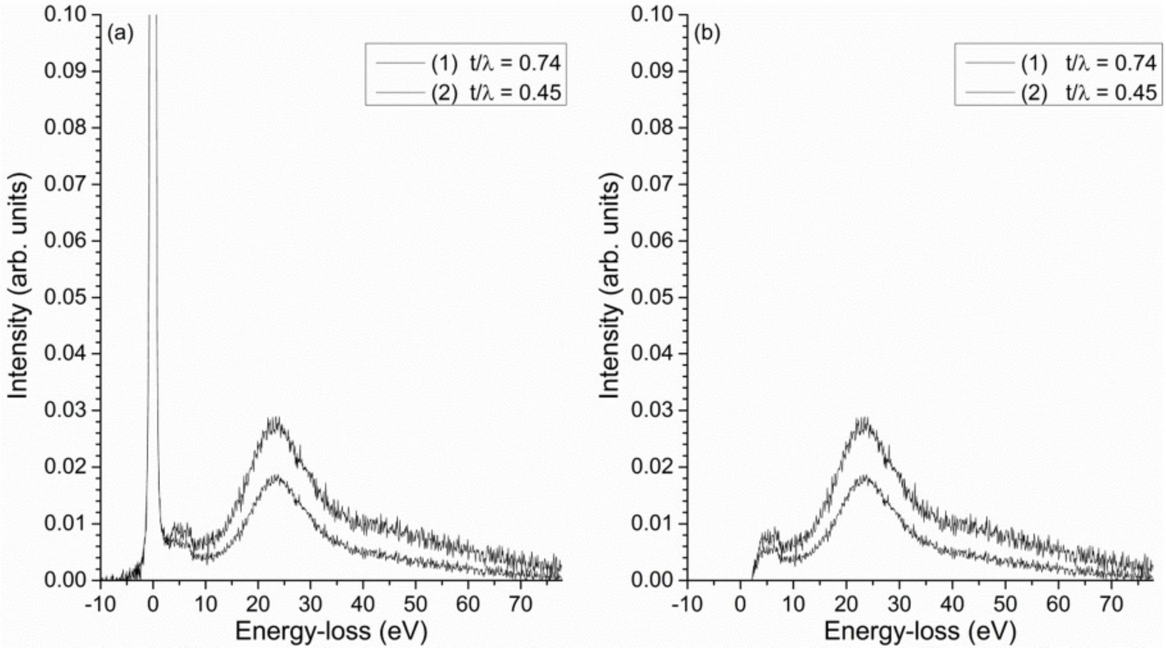

Fig. 4.4.7 (a) Low-loss spectra and (b) inelastic scattering intensities extracted from the low-loss spectra of the a-C:H specimen from regions with t/λ of 0.74 and 0.45.

In Fig. 4.4.8 typical C-K edge spectra are presented which were taken from the a-C:H film at positions of the cross-section specimen ranging from ~ 20 to ~ 500 nm below the surface. This figure demonstrates the details of the applied EELS data processing, i.e. in Fig. 4.4.8(a) raw spectra are depicted, spectra after background subtraction are shown in Fig. 4.4.8(b) and spectra after plural-scattering deconvolution in Fig. 4.4.8(c). Each subfigure of Fig. 4.4.8 presents 13 C-K edge spectra from the a-C:H film, among which the spectra labeled from (1) to (8) are recorded from regions with a relative thickness t/λ (mean) = 0.46 and the spectra from (9) to (13) at positions with t/λ (mean) = 0.73. These C-K edge spectra were manually aligned horizontally to locate the maxima of the π^* intensities at 285 eV, but vertically normalized according to their σ^* intensities. For the raw data in Fig. 4.4.8(a), a background is clearly observable for each individual spectrum. The jump-ratio, which is the ratio of the maximum edge intensity to the minimum intensity of the background just below the edge, also known as the signal-to-background ratio, is measured as ranging from 5 to 10. A 50 eV wide background-fitting window was positioned just in front of the rise of the π^* pre-peak, but any arc-shaped features of surface dangling bond resonances was always avoided from the selection (as already mentioned in section 3.4.3). The background was then fitted by a power-law function and extrapolated into the post-edge region. In Fig. 4.4.8(b), where the background is for each spectrum, the π^* pre-peaks are seen of a similar height and the broad σ^* peaks shows a tip at 292.2 eV. For all C-K edges shown, spectral contributions arising from plural scattering, mainly by the excitation of σ plasmons, are evident at ~ 325 eV, among which the last five spectra exhibit much larger plasmon contributions owing to the thicker specimen regions. In addition, in the last two spectra with t/λ equals to 0.76 and 0.74, the tips mounted on the σ^* peaks appear less pronounced since their maxima are surpassed by the higher-lying shoulders of the σ^* peaks. The plural scattering intensities were removed by Fourier-ratio deconvolution of the C-K edge spectra with their corresponding low-loss spectra, yielding nearly single-scattering spectra as shown in Fig. 4.4.8(c). For all the spectra, it can be seen that the plural scattering contribution of the plasmon excitation is reduced to a similar level that can be neglected, despite the previous intensities are significantly different. Moreover, the shoulders of the σ^* peaks were lowered as well. However, the 292.2-eV tips for spectra (12) and (13) are still less pronounced than those in other spectra, which could be due to the inadequate removal of the plural scattering by this Fourier-ratio deconvolution technique.

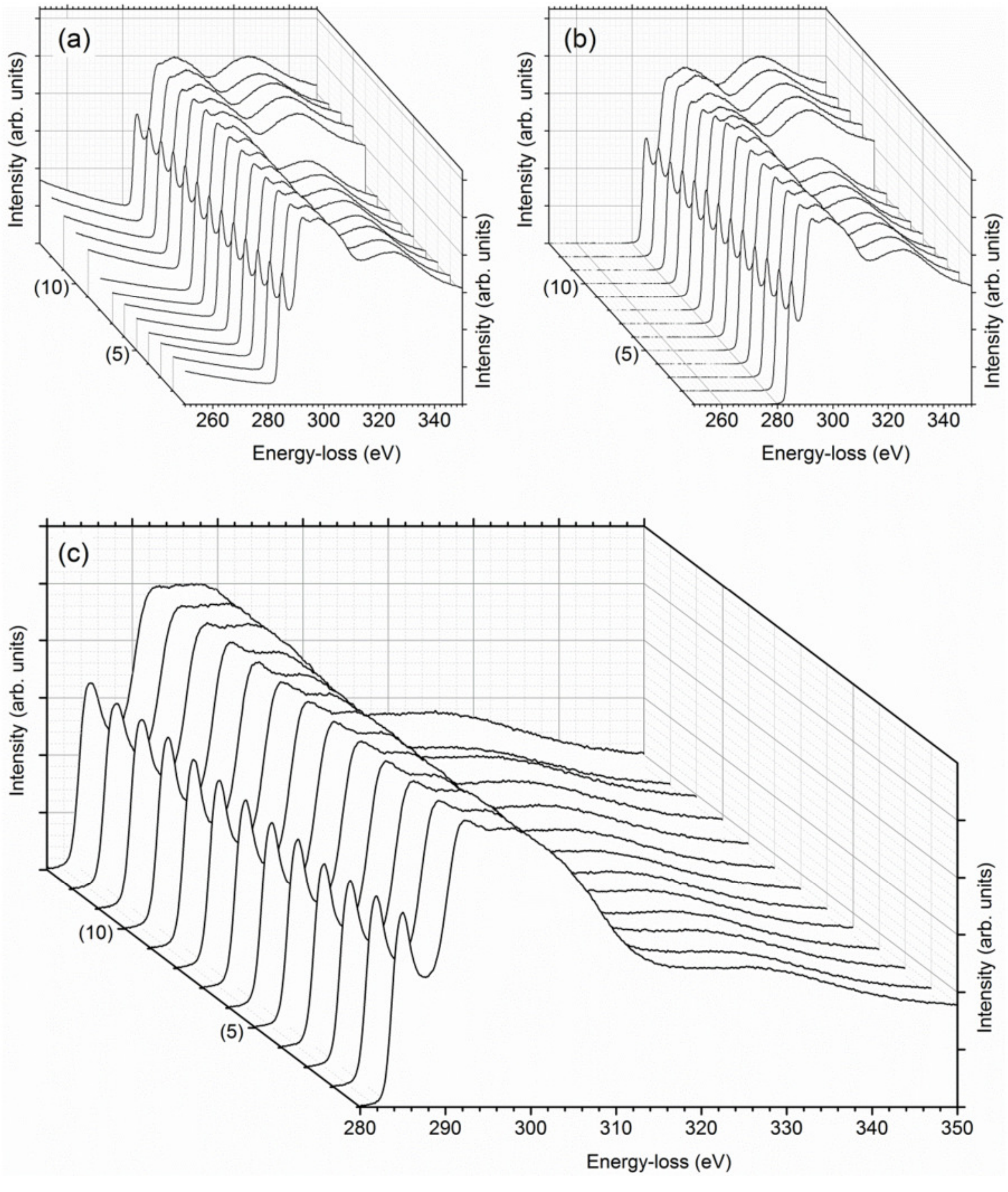

Fig. 4.4.8 EELS data-processing procedure for 13 C-K edge spectra (labeled from (1) to (13) taken under magic-angle condition from a-C:H: (a) raw spectra, (b) spectra after background subtraction, (c) spectra after deconvolution with relevant low-loss spectra.

EELS quantification tests were performed based on the setting of the two integral windows previously described for HOPG in Table 4.1 (284.7 – 285.3 eV for $I_{\pi*}$ and 292 – 307 eV for $I_{\sigma*}$), using the *I*-ratio in form of $I_{\pi*}/I_{\sigma*}$. Firstly, the σ* window was varied with the π* window fixed (284.7 – 285.3 eV). Fig. 4.4.9(a, c) reproduce the spectrum labeled (13) in Fig. 4.4.8(c) from a thick specimen region ($t/\lambda = 0.74$), while in Fig. 4.4.9(b, d) the spectrum with label (1) from a thin region ($t/\lambda = 0.47$) is shown. In each figure, the spectrum of the HOPG reference (spectrum (1) in Fig. 4.4.4) is also included for comparison. In Fig. 4.4.9(a, b), sp^2-C quantification results are superimposed on the spectra as a function of the position of the upper boundary of the σ* window, which was varied from 293 eV to 320 eV, with the lower boundary of the σ* window maintained at 292 eV.

In the case of both spectra, the plotting can be clearly divided into three sectors I to III (cf. Fig. 4.4.9 (a)). The quantification results show a drop of the evaluated sp^2-C content for the σ* upper boundary from 293 eV to 300 eV, followed by a stable region of little variation from 300 eV to 314 eV. For energy windows ending from 314 eV to 320 eV, a drop of the sp^2-C value can be seen again. For the spectrum in Fig. 4.4.9(a), within each of the three sectors the standard deviations of the calculated sp^2-C values are 0.039, 0.007, and 0.027 with increasing sector number, while for Fig. 4.4.9(b) the deviations are 0.046, 0.006, and 0.028.

On the other hand, Fig. 4.4.9(c, d) plot the determined fraction of sp^2-C as a function of the starting position of the σ* energy window, with the upper boundary fixed at 307 eV. In both figures, i.e. Fig. 4.4.9(c, d), each plot shows a smaller range of variation than that observable in Fig. 4.4.9(a, b). A gradual increase of sp^2 % is rather clear in the region before 291 eV, where the latter is a maximum point. Afterwards, from 292 eV to 300 eV the quantification results show a descending and ascending arc, with a small extreme value in between. At the end, an increase of the calculated sp^2-C content is seen, with its starting point traced back to ~ 298 eV. The standard deviations for the corresponding testing regions, 286 – 292 eV, 292 – 300 eV, and 298 – 307 eV are 0.010, 0.007, and 0.024 for the results in Fig. 4.4.9(c), while being 0.011, 0.006, and 0.024 for those in Fig. 4.4.9(d).

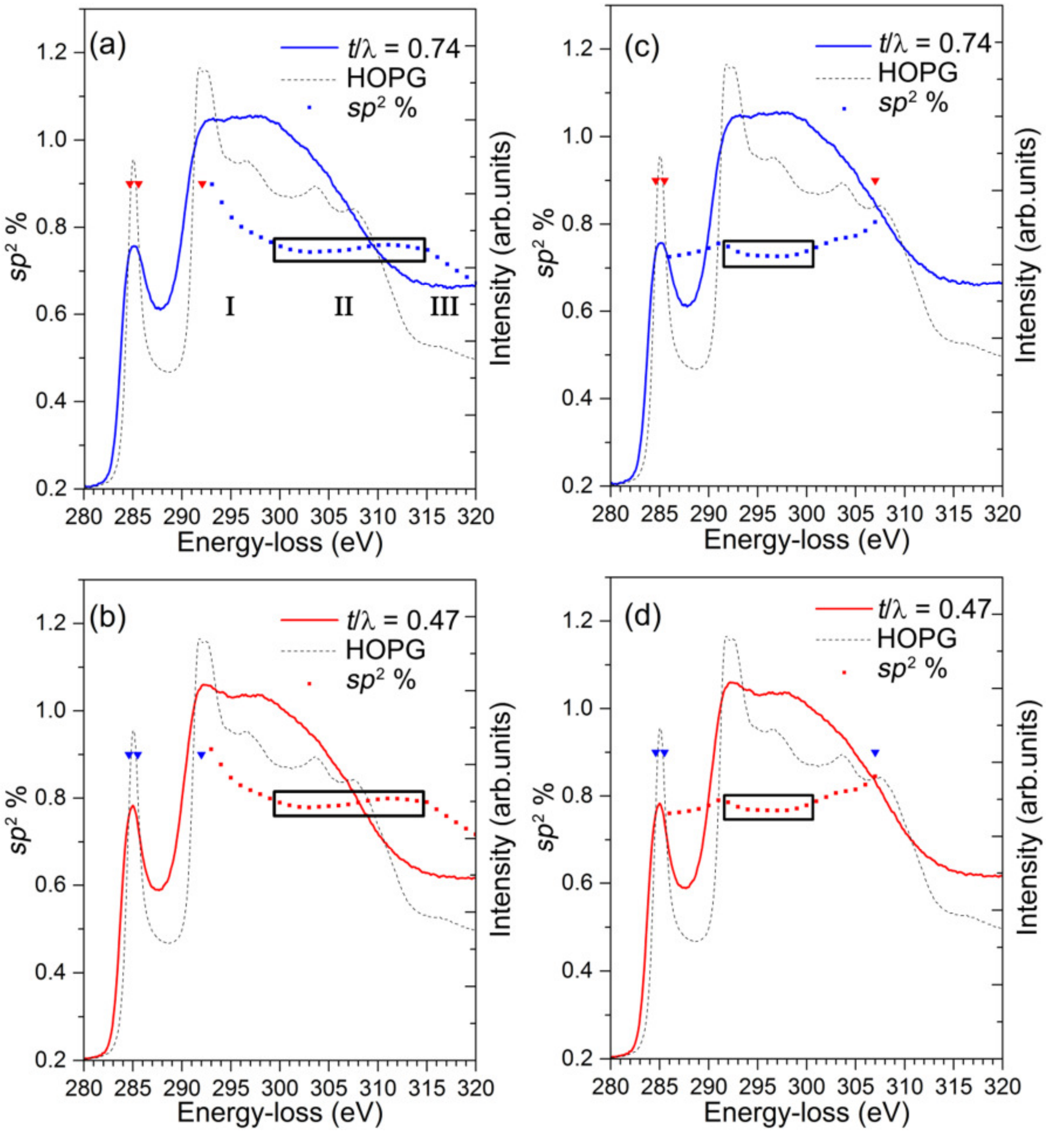

Fig. 4.4.9 EELS quantification results for the C-K ELNES of a-C:H as a function of (a, b) the upper boundary of the σ* energy window and (c, d) the lower boundary of the σ* energy window with relevant spectra from sampled area (a, c) $t/\lambda = 0.74$ and (b, d) $t/\lambda = 0.47$ superimposed on the results.

The tests of the influence of width variation of the π* window on the quantified *sp*^{2}-C content were based on setting the σ* window from 292 eV to 307 eV and keeping the π* window centered at the maximum intensity of the π* pre-peak (285 eV). The size of the π* energy window previously used (0.7 eV) is slightly larger than the energy resolution (0.6 eV). A variation of both boundaries for ± 0.2 eV gives standard deviations of 0.020 for spectra in Fig. 4.4.9 (a, c) and 0.019 for spectra in Fig. 4.4.9(b, d).

The setting of integration windows from 284.7 to 285.3 eV for the π* peak and from 292 to 307 eV for σ* excitations is applied for ELNES quantification of all 13 spectra, which gives a fraction of *sp*^{2}-C of (76.9 ± 1.1) %. In more detail, for spectra from (1) to (8) (thin specimen regions), the *sp*^{2} % is (77.2 ± 0.7) %, while for spectra from (9) to (13) (thick region), the *sp*^{2} % is (76.3 ± 1.3) %.

Quantification results for all 13 spectra obtained by varying the upper boundary of the σ* window between 300 and 314 eV, by varying the lower σ* window boundary between 292 and 300 eV, and by varying the size of the π* window between 0.3 and 0.9 eV (351 numbers in all) amount to an average of 76.6 % with a standard deviation of 1.7 %.

4.4.6 SEM and conventional TEM imaging of ta-C

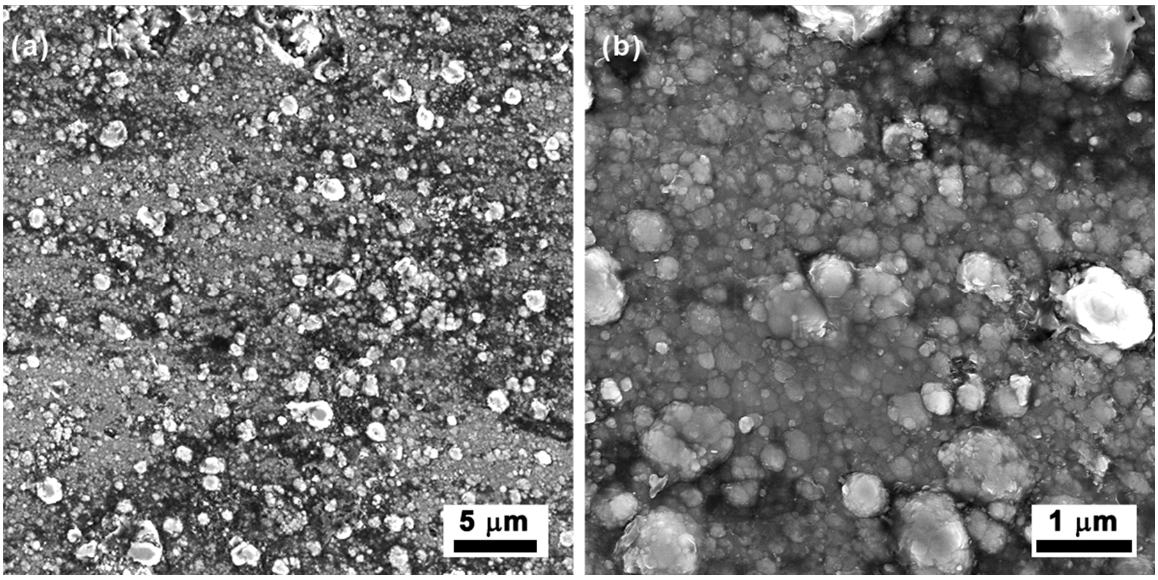

Fig. 4.4.10 SEM images of the surface topography of the as-deposited ta-C sample, (a) overview image, (b) detailed image taken at higher magnification.

According to the SEM observation at low magnification (Fig. 4.4.10(a)), the topography of the pristine surface of the ta-C film is rather chaotic. Compared to the a-C:H specimen with the cauliflower-like structure (cf. Fig. 4.4.5), there is no similar regular structure visible since the deposition rigs and consequently the growth mechanisms for the these two films are rather different. At a higher magnification of 30,000 times (Fig. 4.4.10(b)), in top view the ta-C specimen is seen mainly composed of small swells with diameters of a few 100 nm. A number of relatively large swells with a typical diameter of ~ 1 µm, which are responsible for the random topography in Fig. 4.4.10(a), could be identified as aggregations of those small ones.

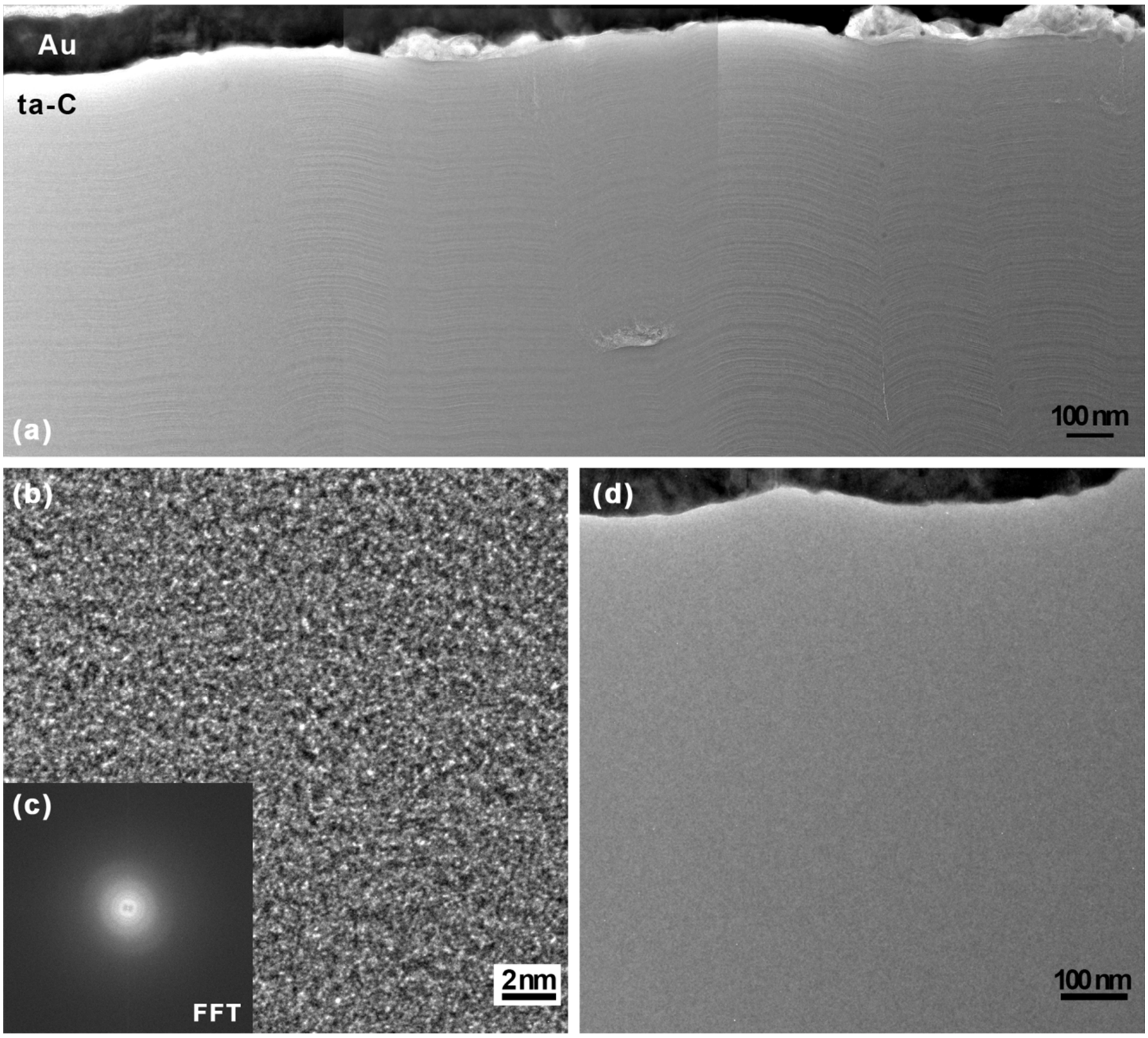

Fig. 4.4.11 Microstructural characterization of the ta-C film by cross-section TEM imaging. (a) Overview given by a montage of three single TEM bright-field images, (b) an HRTEM image obtained from a thick specimen region with (c) the corresponding diffractogram, and (d) TEM bright-field image of a thin region.

In cross-section TEM imaging, the ta-C specimen looks more uniform than observed from top. Though, in comparison to the findings of the a-C:H there are microstructural differences observable, which are especially evident for thicker regions of the TEM specimen. This can be concluded from Fig. 4.4.11(a), showing a montage of three single TEM bright-field images taken from an extended area of the FIB-prepared lamella. Here, where later on a thickness over 100 nm was measured by low-loss EELS, wavy fringes can be seen inside the film that propagate along the whole deposited ta-C layer. As found for other ta-C DLC/steel specimens (not shown), it can be assumed that these fringes follow the surface topography of the underlying steel substrate and, moreover, are running mostly parallel to each other with a mean distance of a few nm. However, those fringes are invisible in HRTEM images of the same region as shown in Fig. 4.4.11(b), which reveals an amorphous structure of the ta-C DLC layer. Although the image quality is limited by the large specimen thickness, this finding is in agreement with the corresponding diffractogram (Fig. 4.4.11(c)). In other regions (Fig. 4.4.11(d)), where the specimen is much thinner (thickness ~ 50 nm and less), fringes were not detected, either, and it is highly possible that FIB milling with its damaging influence disturbed the fringe contrast. We assume here that structural variations among these fringes in the ta-C layer could also not be detected by EELS.

4.4.7 EELS data processing and ELNES quantification of ta-C

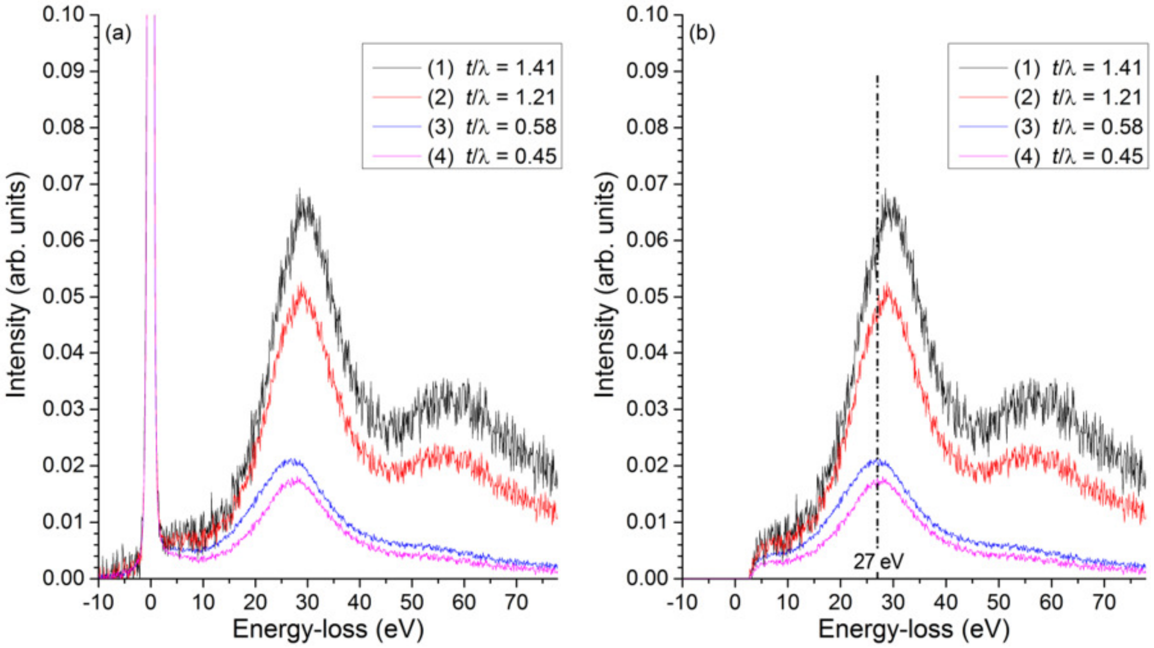

Fig. 4.4.12 (a) Low-loss spectra and (b) inelastic scattering intensities extracted from the low-loss spectra of the ta-C film, EELS spectra were recorded from regions with a relative thickness t/λ of 1.41, 1.21, 0.58, and 0.45.

Fig. 4.4.12(a) shows four enlarged low-loss EELS spectra from the ta-C film, superimposed on each other without any vertical offset. For all spectra, the maximum intensities of the zero-loss peaks were normalized to 1 and only 1/10 of their heights are shown in the figure. The energy resolution measured as the ZLP's FWHM (not included in the figure) amounts to 0.6 eV. The signals of the σ plasmons are all rather noisy owing to their low intensities compared to the zero-loss peaks. The plasmon peaks in spectra (1) and (2) are noisier than those in spectra (3) and (4), because before normalization the maximum intensities of spectra (1) and (2) were ~ 1 order of magnitude smaller than those in spectra (3) and (4). Calculated by the equations 3.6 and 3.7 , the relative thicknesses given as t/λ are 1.41, 1.21, 0.58, and 0.45, respectively, and the thickness sequence is in accordance with the height sequence of the corresponding σ plasmon peaks. For the raw low-loss spectra (Fig. 4.4.12(a)), in the range just above the ZLP any signal raise attributed to π–π* excitations is hardly visible. But, after separating the inelastic signals from the tails of the zero-loss peaks as shown in Fig. 4.4.12(b), an extremely small signal increase can be recognized at an energy loss of ~ 5 – 6 eV. However, compared to a-C:H (cf. Fig. 4.4.7(b)) the spectral contribution of the π–π* excitations is here much lower, which is in agreement with the higher fraction of sp^3-bonds expected for ta-C. Furthermore, for spectra (1) to (4) it can be seen that the σ plasmon peaks are centered at 29.4 eV, 28.8 eV, 26.8 eV, and 27.4 eV, respectively. The energies of the σ plasmon are ~ 4.5 – 6.5 eV higher than that for a-C:H (~ 23 eV from Fig. 4.4.7), among which this shift to higher energies is more pronounced for thicker regions, i.e. spectra (1) and (2). A dash dot line is positioned at 27 eV to guide the eye. As already demonstrated in section 3.4.1, the position of the σ plasmon has been studied indicative of the sp^2/sp^3-ratio in C-materials in literature, therefore the shifts are probably due to the less influence of FIB damaging for spectra (1) and (2). Additionally, because of the larger specimen thickness a second plasmon peak shows up at 56.7 eV and 55.9 eV in spectra (1) and (2). For spectra (1) and (2) the onsets of the first plasmon peaks are at approximately 21.5 eV, whereas those of spectra (3) and (4) are about 19 eV.

Each individual graph (a), (b), and (c) of Fig. 4.4.13 demonstrates 20 C-K edge spectra of the ta-C film with a depth from the original surface of ~ 20 – 1000 nm, among which the spectra labeled from (1) to (9) are recorded at t/λ of 0.44 – 0.69 and the spectra labeled from (11) to (20) are recorded at t/λ of 1.06 – 1.42. The spectra labeled (18), (15), (5) and (1) correspond to the low-loss spectra labeled from (1) to (4) in Fig. 4.4.12. In horizontal direction these C-K edge spectra were manually aligned with respect to the maxima of the π* intensities at 285 eV, whereas vertical normalization was done according to their σ* intensities. Fig. 4.4.13(a) presents the raw EELS spectra; subsequently, in Fig. 4.4.13(b) and Fig. 4.4.13(c) spectra are shown after background subtraction and after plural scattering deconvolution, respectively, illustrating the sequence of data processing. Background intensities are visible for all the spectra in Fig. 4.4.13(a), and the C-K edge jump ratios are in the range between 4 and 10. A 50 eV wide background-fitting window was positioned just in front of the rise of the π* pre-peak for each raw spectrum in Fig. 4.4.13(a), avoiding any arc shape of surface dangling bond resonances (mentioned already in section 3.4.3). As usual, the background was fitted by a power-law function and extrapolated into the higher-energy edge region. In Fig. 4.4.13(b), where the background is subtracted for each spectrum, we can clearly see that the π* pre-peaks show a height which is higher for the first 9 spectra compared to the next 11 spectra. The broad σ* peaks at 292.2 eV are all round and featureless. For all spectra, at ~ 325 eV contributions to the C-K edge by additional excitations of plasmons are observable. These plasmon contributions are distinctly broad and intense for the last 11 spectra, which were taken from thicker regions. These plural scattering intensities were removed by deconvolution of the C-K edge spectra with their corresponding low-loss spectra (Fig. 4.4.13(c)). Obviously, it can be seen that the intensities beyond the σ* peaks were reduced to a similar order by applying this correction, regardless of their previous appearances.

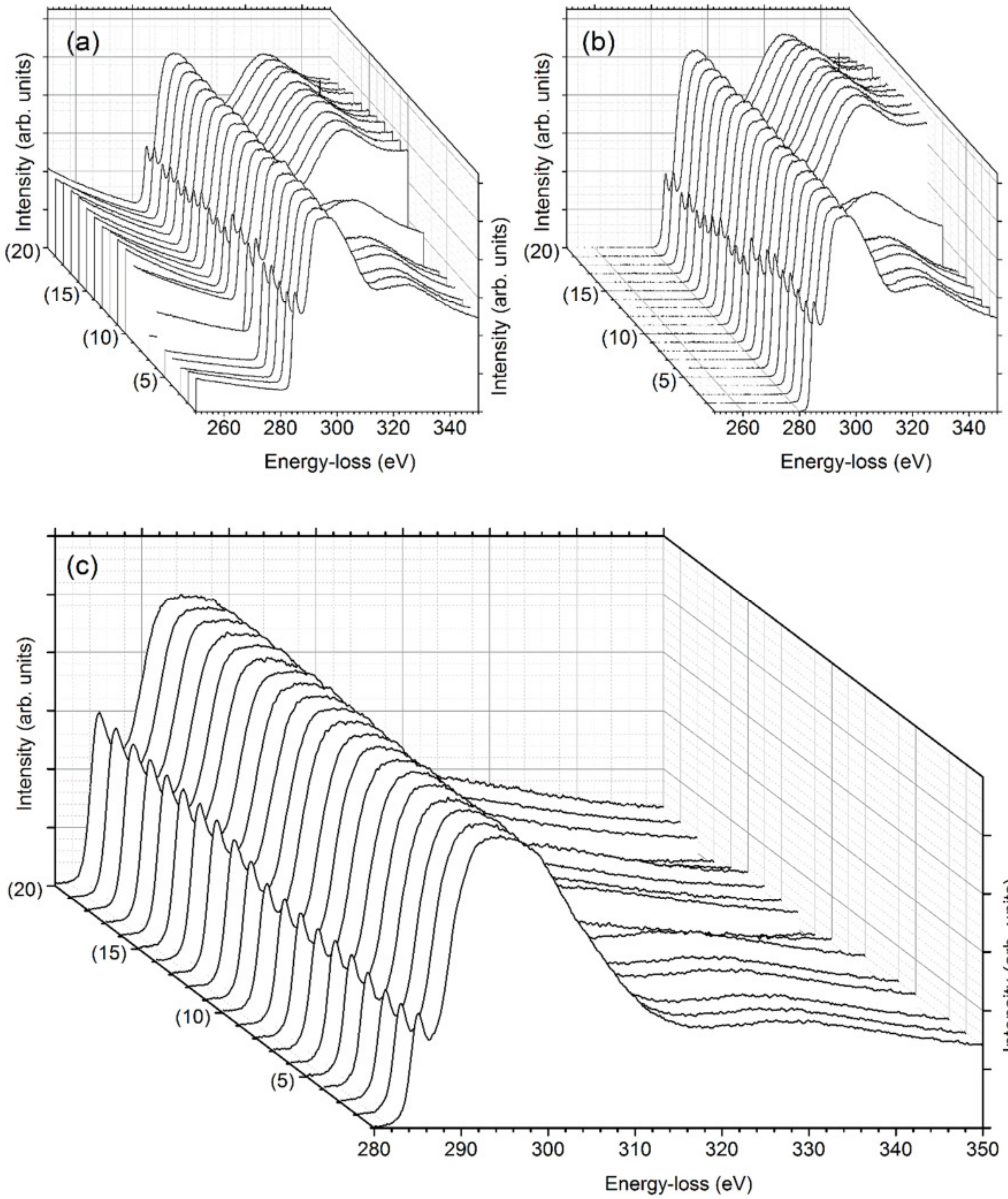

Fig. 4.4.13 EELS data processing for 20 C-K ELNES spectra (labeled from (1) to (20)) taken under magic-angle condition from ta-C: (a) raw EELS spectra, (b) spectra after background subtraction, and (c) spectra after deconvolution with relevant low-loss spectra.

As already reported for quantitative EELS studies on a-C:H (cf. section 4.4.5), similar quantification tests were carried out for the ta-C sample. In detail, the influence of the particular choice of the integration windows onto the resulting I-ratio in the form of $I_{\pi*}/I_{\sigma*}$ was tested by variation of the positioning of the energy-window boundaries.

Firstly, the σ* integration window was varied, where the π* window was kept fixed. Fig. 4.4.14 reproduces two C-K ELNES spectra obtained from differently thick regions, namely labeled with (15) and (5) in Fig. 4.4.13). The former (Fig. 4.4.14(a, c)) was taken from a thick ta-C region (t/λ = 1.41) and clearly shows a lower sp^2 % than the latter (Fig. 4.4.14(b, d)) obtained from a thin region (t/λ = 0.58). For comparison, the spectrum from the HOPG reference (spectrum (1) in Fig. 4.4.4) is also included in each graphical presentation. In Fig. 4.4.14(a, b), sp^2-C quantification results are superimposed on the spectra as a function of the position of the upper boundary of the σ* window, which was varied from 293 eV to 320 eV with the lower boundary of the σ* window maintained at 292 eV. For both spectra, the variation of the sp^2 % shows a descending first part from 293 eV, whose slope gets flattened at ~ 302 eV, followed by an increase until a maximum is reached at ~ 315 eV. Afterwards, the curve decreases again until the end of the scale. We separate the plotting into three sectors by two points at 297 eV and 307 eV, and the middle sector is centered at 302 eV, where the slope is approximately zero. For these three sectors, the standard deviations of the calculated sp^2 % values are 0.029, 0.010, and 0.012 for Fig. 4.4.14(a) and 0.037, 0.008, and 0.019 for Fig. 4.4.14(b).Secondly, Fig. 4.4.14(c, d) plot the fraction of sp^2-C as a function of the starting position of the σ* energy window, with the upper boundary fixed at 307 eV. A region with a gradual increase of sp^2 % is rather clearly visible before 291 eV, corresponding to a local maximum of sp^2 % = 0.55 for Fig. 4.4.14(c) and sp^2 % = 0.68 for Fig. 4.4.14(d). For higher energy losses from 291 eV to 298 eV, the quantification results show a descending and ascending arc with only a slow variation in the sp^2-C content and a relatively wide region of a minimal extreme point in between. At the end, an increase of the sp^2 % shows up, with its starting point traced back to ~ 295 eV. The sp^2 % standard deviations obtained for three regions, i.e. 286 – 291 eV, 291 – 298 eV, and 298 – 307 eV, amount to 0.011, 0.007, and 0.047 for the results presented in Fig. 4.4.14(c), while are 0.012, 0.006, and 0.044 for those in Fig. 4.4.14(d).

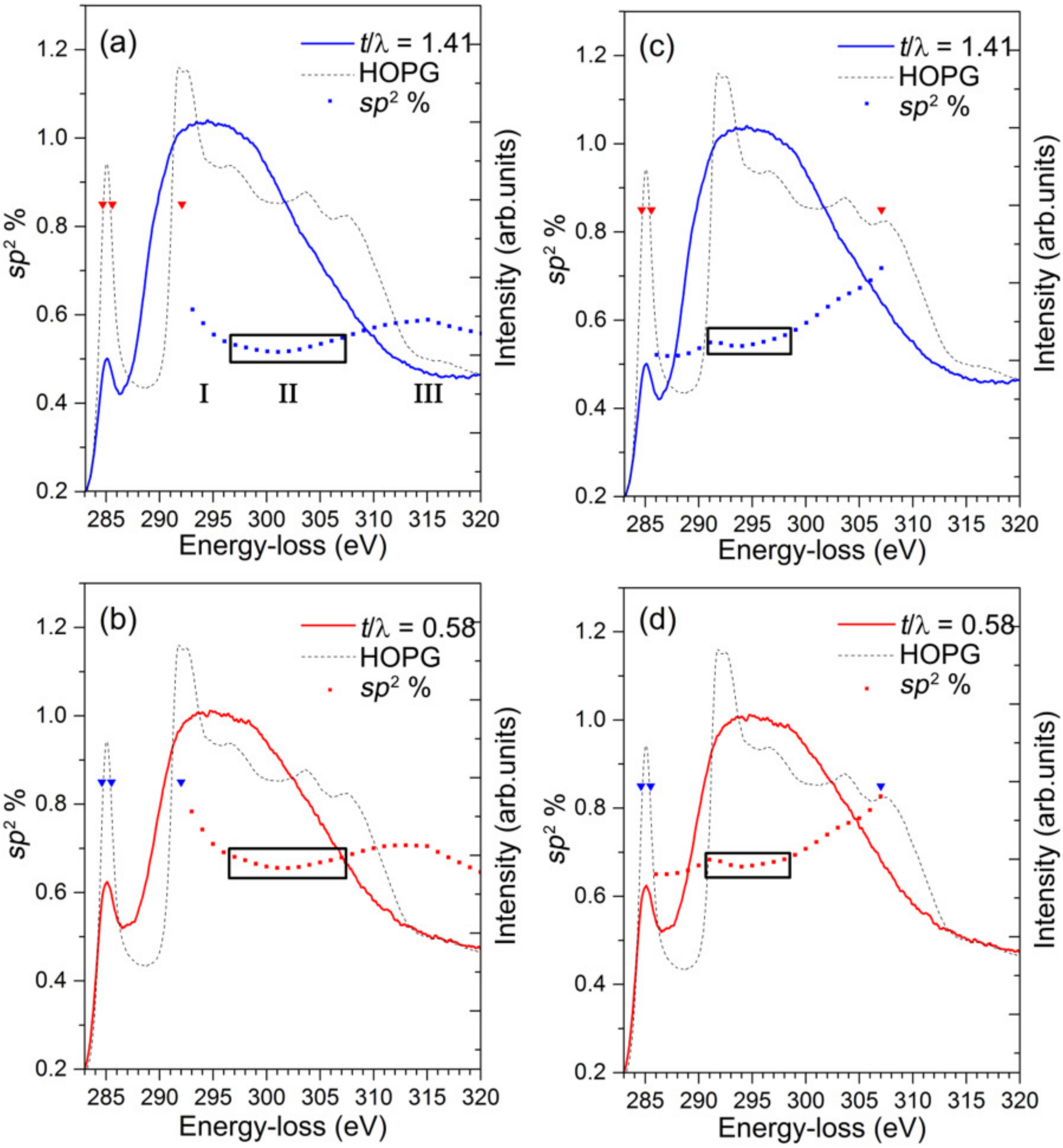

Fig. 4.4.14 Quantification results for the C-K ELNES of ta-C as a function of (a, b) the upper boundary of the σ* energy window and (c, d) the lower boundary of the σ* energy window together with relevant spectra from thick ta-C regions (a, c) with t/λ = 1.41 and thinner ones (b, d) with t/λ = 0.58. For comparision, in each graph the C-K ELNES spectrum of HOPG is also shown.

As in the case of a-C:H, the tests shown here for ta-C of the influence of the size variation of the π* window onto the determined sp^2 % were again based on setting the σ* window from 292 eV to 307 eV and keeping the π* window centered at the maximum intensity of the π* pre-peak (285 eV). The π* energy window is again 0.7 eV in width, i.e. slightly larger than the energy resolution (0.6 eV). A variation of both boundaries in a range of ± 0.2 eV gives sp^2-C contents of 0.550 ± 0.009 for the spectrum in Fig. 4.4.14(a, c) ($t/\lambda = 1.41$) and 0.682 ± 0.015 for that in Fig. 4.4.14(b, d) ($t/\lambda = 0.58$).

For comparison purposes, when setting the integration windows from 284.7 eV to 285.3 eV for the π* signal and from 292 eV to 307 eV for the σ* excitation, quantification of the sp^2-C fraction of all 20 C-K ELNES spectra results in values between approximately 0.55 for $t/\lambda = 1.41$ and 0.68for $t/\lambda = 0.58$, exhibiting a large scatter, and the standard deviation is about 0.069. This behavior hints at a strong influence of the specimen thickness on the quantified sp^2 % value and, therefore, on a more or less pronounced effect of FIB-induced damage. This phenomenon is revealed in more detail in the next section, dealing with the correction of erroneous contributions of FIB-induced damage to ELNES quantifications of the sp^2/sp^3-ratio.

4.4.8 Correction of FIB-induced damage for a-C:H and ta-C

For all spectra, fractions of sp^2-C were quantified by the two-window method using the I-ratio in form of I_{π^*}/I_{σ^*} and setting of the energy windows to 284.7 – 285.3 eV (π*) and 292 – 307 eV (σ*), by referring to the spectrum recorded from the cleaved HOPG reference sample. The thickness effect is demonstrated in Fig. 4.4.15, where the sp^2 % is plotted as a function of the reciprocal relative thickness (λ/t) of each region analyzed by STEM/EELS. Linear fittings were performed on data groups obtained from the a-C:H and ta-C specimens, respectively (dashed lines in Fig. 4.4.15).

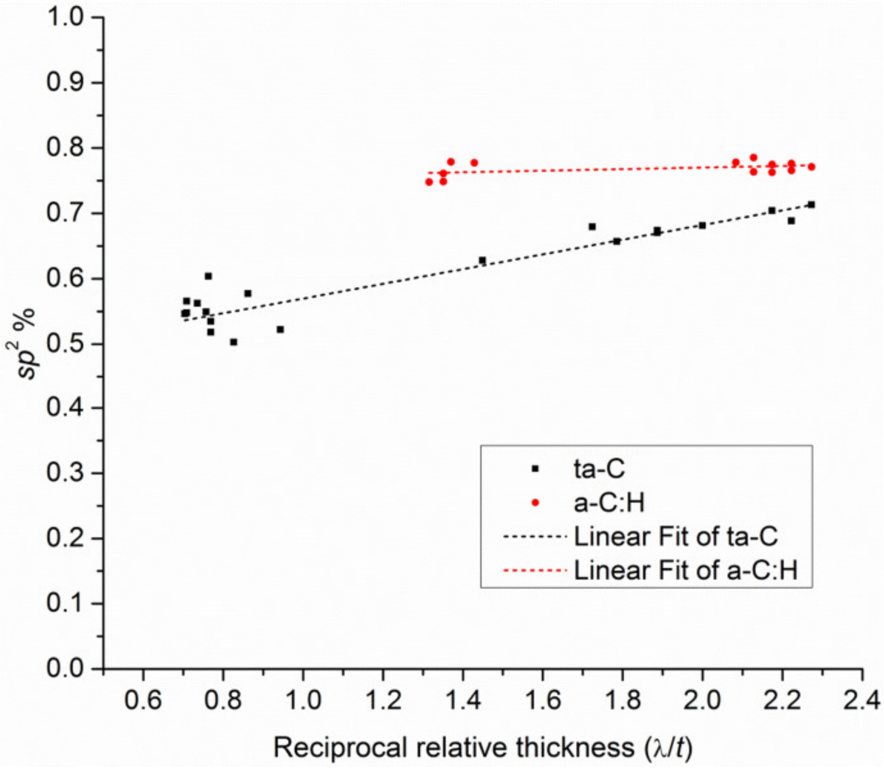

Fig. 4.4.15 sp^2-C quantification by ELNES analyses for the a-C:H and ta-C films as a function of the reciprocal of the relative thickness (λ/*t*). Dashed lines are linear fitting results for each sample.

It has already been shown for a-C:H that the mean quantification results of the overall spectra, i.e. the sp^2 % values obtained from EELS spectra of thin specimen regions (t/λ ~ 0.47) and those of thicker ones (t/λ ~ 0.74) are close to each other, where the difference lies within the range of the standard deviation. As a result, plotting the quantification results as a function of the reciprocal relative thickness and performing linear fitting, a nearly horizontal line is seen (as illustrated by the red dashed line in Fig. 4.4.15). Subsequently, the linear function in form of equation 4.16 is

$$R = (0.746 \pm 0.014) + (0.012 \pm 0.008)/T \,. \qquad 4.17$$

The data set for the ta-C film shows a larger scatter of sp^2 % from 50.3 % to 71.3 % with t/λ ranging from 0.44 to 1.42 (black dashed line in Fig. 4.4.15), which is well fitted by a linear relationship. Here, the linear function (cf. equation 4.16) is

$$R = (0.457 \pm 0.013) + (0.112 \pm 0.009)/T\,. \qquad 4.18$$

Seen from the trend line (black dashed line in Fig. 4.4.15), the values of sp^2 % fit better to the line towards the right end of the scale, i.e. when t/λ is smaller than 0.7, while the data points deviate more from the fitting line at the other end, i.e. for thicker specimen regions. As already mentioned in subchapter 4.4.7, this wide range of sp^2 % values from 50.3 % to 71.3 % for one and the same ta-C specimen is probably due to the more or less increase of sp^2-hybridized carbon atoms induced by FIB damage. Consequently, the thicker the ta-C film analyzed by STEM/EELS the less is the error in the quantified sp^2-content. On account of this, for the present ta-C DLC the true sp^2-content is expected to be approximately 50 %, which is about 22 % lower than that of the a-C:H sample.

4.4.9 Quantification results from other formalisms based on the two-window method

Due to the FIB-induced damage of the ta-C sample, we have a variety of C-K edge spectra showing a wide range of determined sp^2 % values, indicating a definite dependence on the transmitted DLC film thickness. To evaluate the influence of the specific formalism used for quantification of the sp^2-content based on the two-window method applied to the C-K ELNES (see section 3.4.3), the three different setups of integration-window setting were tested on all available EELS data. Therefore, quantification was performed on all the 33 C-K edge spectra recorded from both the a-C:H and ta-C samples, where in each case the two-window method was used. In more detail, the formalisms regarding I_{π^*}/I_{σ^*} and $I_{\pi^*}/I_{\pi^*+\sigma^*}$ with the same setting of energy windows, i.e. 284.7 – 285.3 eV for π^* and 292 – 307 eV for σ^* signal integration, were applied as well as the formalism using $I_{\pi^*}/I_{\Delta E}$, whereupon the π^* and σ^* energy windows were identical.

In Fig. 4.4.16 the relationship of resulting sp^2 % values is plotted for the quantification based on the usage of $I_{\pi^*}/I_{\pi^*+\sigma^*}$ and $I_{\pi^*}/I_{\Delta E}$ intensity ratios against the results obtained by using the I_{π^*}/I_{σ^*} ratio. Evidently, the use of $I_{\pi^*}/I_{\pi^*+\sigma^*}$ shows an underestimated of sp^2 % compared to the use of I_{π^*}/I_{σ^*}. Specifically, a parabolic fitting to the data nicely (adjusted r-square = 1.00) passes through the values (0, 0) and (1, 1), meaning that these two formalisms give identical results in such extreme cases. In contrast, the use of the

$I_{\pi^*}/I_{\Delta E}$ ratio shows a larger underestimation of sp^2 %. Furthermore, the parabolic fitting (adjusted r-square = 0.99) passes through the (0, 0), but not through (1, 1).

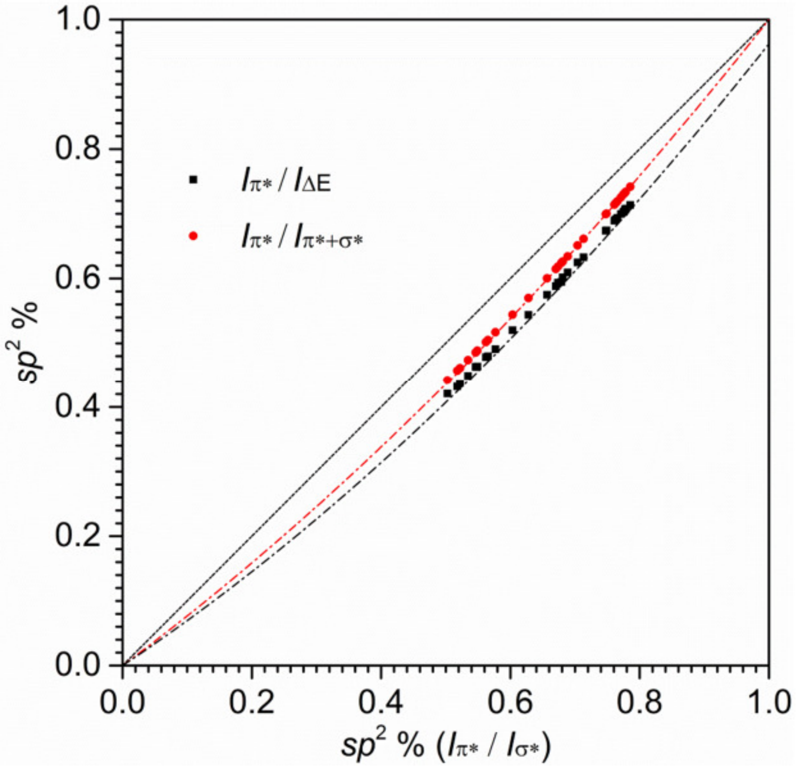

Fig. 4.4.16 Plotting of sp^2 % quantification results derived by formalisms using the $I_{\pi^*}/I_{\pi^*+\sigma^*}$ and $I_{\pi^*}/I_{\Delta E}$ intensity ratios against those by using I_{π^*}/I_{σ^*}.

4.5 Discussion

4.5.1 Microstructure of HOPG and DLC specimens

Despite of some beam damage observable at 300 kV accelerating voltage, HRTEM imaging of the ZYA-grade HOPG specimen (MikroMash^{TM}) revealed a fairly good crystallinity, which is good enough to be used as graphite reference for quantitative STEM/EELS analyses (cf. Fig. 4.4.1). Particularly, as demonstrated by structure imaging along the [001] zone axis, the use of cleaved HOPG specimens is recommended since here no preparation artifacts occur that could falsify any TEM investigation. Because of the general cleavage behavior of graphite, however, cross-section TEM specimens orientated perpendicularly to [100] cannot be prepared by the scotch-tape technique. For this reason, FIB-prepared HOPG lamellae have to be used for combined TEM and EELS investigations along the [100] zone axis. In addition, a FIB-prepared HOPG lamella perpendicular to [001] was also used for further detailed comparison. To summarize, the HOPG specimen cleaved parallel to the (001) lattice planes and two FIB-prepared TEM lamellae cross-sectioned along the [100] as well as [001] direction were demonstrated to be well suited to determine the magic-angle conditions (MAC) for STEM/EELS at 80 keV. Any further quantitative STEM/EELS analysis of DLC and diamond films could not be performed without this prerequisite of a well-defined MAC.

As expected for DLCs, both the a-C:H and ta-C films showed an amorphous structure. The completely homogeneous inner structure of the a-C:H film as imaged by TEM/HRTEM is well understandable. In contrast, the reason is unclear for the occurrence of fringes with a spacing of a few nanometers inside the ta-C film by conventional TEM imaging. For an amorphous material with mass-thickness contrast, the fringes indicate density fluctuations, assuming that the sample thickness is constant within the imaged area. Moreover, their appearing in thick specimen regions but disappearing in thin ones indicates that these features are not artifacts induced by the FIB, but could be milled away due to FIB damaging. Our investigations of other ta-C films (not shown here), where the film/substrate interface was also studied, also showed such fringes, and it was found that the curvature of the fringes is exactly the same as the surface profile of the underlying substrate. Recalling that the growth mechanisms of ta-C films involve either subplantation or densification or phase transformation of the growing surface (Schwan et al., 1996), let assume that such fringes could be formed during the film growth. Any relationship between the fringes and the growth mechanisms could be of general interest for further studies. Nevertheless, there seems to be no detectable influence of these fringe-like structural details on HRTEM image contrast and EELS results, perhaps because of the limitation of HRTEM for a thick specimen region and a too large beam diameter (micro-probe mode was applied for EELS acquisition), minor local structure variations could still exist.

4.5.2 Energy-window determination and sp^2-C quantification

Setting of the σ* integration window

We first discuss the setting of the σ* integration window, which is in general less sensitive for the sp^2-quantification than that of the π* window.

The first general concern would be the plural scattering or error in the corresponding plural scattering removal. The optimization of the cut-off position for the σ* window correlates with both the strength and the position of the plasmon. The former factor corresponds to the specimen thickness, which determines the intensity of the plural scattering (only negligible if the specimen is much thinner than the plasmon mean free path) and is largely correlated to the effectiveness of the deconvolution process with the corresponding low-loss spectrum (errors in this technique are always possible and could be severe for specimens with t/λ larger than 1). Regarding the position of the σ plasmon peak, it is more reliable to consider its onset position instead of its maximum position since the plasmon peak is usually rather broad.

Taking the a-C:H spectra as an example (cf. section 4.4.5), seen from the low-loss spectra, the onset of the σ plasmon is ~ 17 eV above the zero-loss peak and the maximum is at ~ 23 eV. Thus in an analog manner, plural scattering by plasmon excitation could contribute to the C-K edge signal in a range starting about 17 eV above its threshold and extending to higher energy losses. In more detail, since for sp^2-C quantification the necessary integration of the σ* signal is done with an energy window between 292 and 307 eV, there will only be a disturbing influence of the plural scattering of the σ plasmon on the integrated σ* signal in the energy loss range 292 – 300 eV, but such contributions should be noticeable increasingly from 301 eV to 307 eV (considering the onset of C-K edge at 284 eV). For the ta-C sample, the plural scattering contribution to the C-K edge is energetically shifted to higher energy losses since σ plasmon peaks were found in the energy-loss range from about 27.4 eV to 29.4 eV and onsets from 19 eV to 21.5 eV (cf. section 4.4.7), which means the contribution to the C-K edge should start to be noticeable from ~ 303 – 305 eV and reach a maximum at ~ 311 – 313 eV. Unlike to plural scattering by excitation of σ plasmons, contributions of π plasmon excitation to the C-K edge might be less of problem because due to its low intensity compared to that of the σ plasmon. But, if there is any contribution it would little increase the signal in the region of the π* pre-peak, owing to the π plasmon position at 5 – 6 eV.

Secondly, the energy-loss intensities near the lower boundary of the σ* window have been reported to have complex origins: for instance, the higher-lying oscillation structure of π* electronic ionizations (Batson, 1993; Browning et al., 1991; Titantah & Lamoen, 2005), the excitation of C-atoms into an intermediate state (Papworth et al., 2000), and C-H resonances (Fink et al., 1983; Silvaf et al., 1996). Lifetime broadening of the π* signal and σ* signal could also extend into this energy-loss range. Apart from the two-window method ($I_{\pi*}/I_{\sigma*}$), which refrains from this intermediate range, those sp^2-C quantification methods involving a fitting process usually decompose this intermediate area between the π* and σ* peaks to a certain degree, which is a great advantage over the two-window methods. However, each of these fitting methods requires further improvement. The Gaussian function fitting methods roughly treat the higher-lying π* oscillation and lower-shifting σ* peak as the tail/onset of a broad Gaussian function peak. (In fact, one must be very cautious to fit the π* peak by a Gaussian function and include the lifetime broadening effect, which will be discussed later in this section.) Specifically, the three-Gaussian-function fitting method (cf. Fig. 4.2.1), is able to extract a third Gaussian-shaped signal centered at 287 eV, which is variably assigned either to the π* excitations of sp^2-C in H-free amorphous carbon (Robertson & O'Reilly, 1987) or to the σ* excitations of C-H bonds in hydrogenated amorphous carbon by ignoring the π* excitations in this region (Silvaf et al., 1996). Bernier et al. (2008) established a function series to fit the π* excitation until a high energy loss by admitting the higher energy-loss oscillations of the π* excitations, but it is still an approximate treatment. Those model-fitting methods are promising to better deal with the higher-lying π* oscillation and life-time broadening effects due to their in-depth physical background. However, there is still a large discrepancy between the simulated C-K edge models and experimental spectra and, thus, further improvements have to be made (Titantah & Lamoen, 2004b). In addition, the application of a computerized fitting procedure to hydrogenated carbon is difficult because it mostly requires a maximum likelihood measurement to check the quality of fitting (Verbeeck & Bertoni, 2008), which is at present impossible when energy losses of C-H excitations are part of the spectrum.

Thirdly, the differences in σ* fine-structure features for different C-materials must be taken into account. On one hand, the C-K edge spectrum taken from crystalline HOPG shows a very pronounced fine structure of the σ* excitation and beyond it, especially the prominent feature at ~ 292 eV with a width of ~ 3 eV (see Fig. 3.4.4). On the other hand, for a disordered carbon material the σ* excitation is broad and featureless. From this point of view, for quantification of the sp^2/sp^3-ratio it is recommended to increase the size of the σ* integration window so that the effect of graphite fine structure is averaged.

We have tested the positions of the two boundaries of the σ* energy window by varying one of them separately with the other fixed to show the direct influence on the sp^2-quantification (cf. Fig. 4.4.9 and Fig. 4.4.14).

As to the variation of the upper boundary of the σ* energy window (the lower boundary fixed at 292 eV), the first non-stable range (sector I) is seen for 293 – 300 eV for the a-C:H sample, whereas it is 293 – 297 eV for the ta-C specimen (standard deviation in the range 0.03 – 0.05). This behavior could be attributed to the too small size of the σ* integration range to average the pronounced σ* fine structure of crystalline HOPG. After this non-stable range, a stable range (sector II) with nearly constant sp^2 % shows up between 300 eV and 314 eV for the a-C:H specimen and from 297 eV to 307 eV for the ta-C sample, which gives standard deviations smaller than 0.01 for both spectra for each sample. This kind of stabilization could have two reasons. For one thing, the fine structure of crystalline HOPG is better averaged as the size of the σ* energy window increases. For the other, errors in plural scattering removal could be negligible within such a range, because these two ranges are also valid for a stable quantification results for both thick and thin specimen regions (t/λ = 0.74 and 0.47 in Fig. 4.4.9, and t/λ =1.41 and 0.58 in Fig. 4.4.14). Note that the stable range extends to as high as 314 eV for the a-C:H sample, but is clearly narrowed for the ta-C sample, followed by an sp^2 % increase in the range from 307 eV to 315 eV. In the third range (sector III), the standard deviations increase to 0.03 again for the a-C:H specimen in the range of 314 – 320 eV, whereas for the ta-C specimen the standard deviations are 0.01 – 0.02 for 307 – 320 eV.

As the upper boundary of the σ* window is fixed at 307 eV, a stable range of the lower boundary is clearly seen for both spectra of the ta-C sample. Each of the four spectra in Fig. 4.4.9(c, d) and Fig. 4.4.14(c, d) from differently thick specimens shows an increase of sp^2-quantification results in sector I. One of the origins could be those extra signals such as the C-H excitations and the tail of the π* excitations falling between the π* and σ* excitations, which are included in the window for σ* signal integration (see in Fig. 3.4.6). The tail of the π* excitation could be proportional to the sp^2 %, i.e. predominantly strong in graphite with pure *sp*^{2}-C (Robertson & O'Reilly, 1987), but weak for amorphous carbon materials with less *sp*^{2}-C. For the a-C:H sample, the tail of the π* excitation could be weaker than that of HOPG, but additional C-H excitations can be present (see Fig. 3.4.6). As a result, these combined effects lead to a slight underestimation of the *sp*^{2} % and, consequently, a slightly increased *sp*^{2}-quantification result as the lower boundary of the σ* window is moved to higher-energy position (sector I in Fig. 4.4.9(c) and (d)). For the ta-C sample, the tail of π* excitations is clearly much weaker than for HOPG as well as for a-C:H. Therefore the *sp*^{2} % is more underestimated, leading to an obvious increase of the *sp*^{2} % in this range as the lower boundary of the σ* window increases in sector I in Fig. 4.4.14(c) and (d). Nevertheless, this region could be too complex to interpret, because broadening of both π* and σ* peaks could affect the results as well. The stable region afterwards, which is 292 – 300 eV for the a-C:H and 291 – 298 eV for the ta-C, giving a standard deviation of less than 0.01, indicates a reliable quantification. Finally, if the σ* energy window starts higher than 298 eV, the resulting window size could be too small to average the fine structures and, in addition, too sensitive towards errors in plural scattering removal, thus yielding a high standard deviation.

After all, for the setting of the σ* window we have found stable ranges for the lower boundary as 292 –300 eV (for a-C:H) and 291 – 298 eV (for ta-C). As well, regarding the upper boundary stable ranges are 300 – 314 eV (for a-C:H) and 297 – 307 eV (for ta-C) for different specimens with different thicknesses. Therefore, one would be on the safe side to routinely fix the σ* integration window at 292 – 307 eV.

Setting of the π* window

Now we discuss about the setting of the window for integration of the π* excitation. Because of the extremely small width of the π* peak, any small variation of the setting of the π* window could lead to a large scatter in the resulting *sp*^{2} % and, hence, quantification is generally very sensitive to this setting. It is of great importance to study the influence of the π* window onto *sp*^{2}-quantification based on the above-mentioned optimized σ* window setting.

The π* pre-peaks of various C-materials do not only show different relative intensities, but also differ in their FWHMs. It is generally accepted that EELS spectra are broadened by two mechanisms: the lifetime broadening (Lorentzian broadening) and the experimental broadening (Gaussian broadening) (Muller et al., 1998).

On the one hand, the lifetime broadening is correlated with the extension of the periodic structure at the sites of the excitations, i.e. the crystallinity of the material. After excitation of a core electron in the sampled material from an initial state to a final state (an unoccupied state), both the excited electron and the core hole left behind can decay and thus have only finite lifetime. The shorter the lifetime is, the broader the states are. As a result, the EELS spectrum, which is the sum of transitions between initial and final states, is broadened accordingly. The lifetime of the initial and final states is even shorter in an aperiodic environment, resulting in a stronger lifetime-broadening effect of an EELS spectrum for amorphous materials than for crystalline ones (Muller et al., 1998). Therefore, in the sp^2-quantification the direct comparison between the material of interest (amorphous carbon) and the reference material (crystalline graphite), showing different degrees of lifetime broadening, could lead to an error.

On the other hand, the experimental broadening, which is another way of viewing the energy resolution (the FWHM of the zero-loss peak) of the EELS spectrometer, is an instrumental factor, being relevant to the primary electron beam, the electron-optical properties of the spectrometer, thermal effects, etc.. At present, the experimental-broadening effect, usually in the order of better than 1 eV, is less of a problem for EELS quantification because the widths of the ionization edges are generally much larger (~ 50 eV). However, it requires consideration for quantitative ELNES, where the spectral feature of interest could have a similar width as the experimental broadening.

These two broadening effects have been treated differently in different quantification methods. Lifetime-broadening effect is mostly included in the *ab-initio* ELNES simulation, whereas the beam-broadening effect is manually set to zero (an ideal experimental condition). In order to fit here the simulated model to an experimental spectrum, experimental-broadening effect is convoluted into the model as a Gaussian function, whose width is estimated as that of the zero-loss peak. Jorissen (2007) and Titantah and Lamoen (2004b) computed orientation-resolved C-K ELNES of graphite, from which models of π* and σ* components were obtained. Quantification was then performed through fitting of the two components to a C-K edge spectrum of interest by vertical alignment according to the π* maximum and horizontal broadening by convolution with a Gaussian or Lorentzian function. In this approach, the broadening effects were added as a whole into the models, so that they can be compared with a measured spectrum. A Gaussian fitting to the π^* pre-peak without a constrained FWHM gives the integral intensities including both the lifetime-broadening and experimental-broadening effects (cf. Fig. 4.2.1). However, the fact that lifetime-broadening induced intensity is much higher for amorphous carbon than for crystalline graphite, does not allow a direct comparison for quantification and leads to a significant overestimation. For instance, if the π^* intensity is extracted by Gaussian fit, for the two spectra from a-C:H in Fig. 4.4.9, an sp^2 % above 100 % is obtained (only ~ 70 – 80 % by two-window method), which is definitely wrong. With respect to the two-window-method, Berger et al. (1988) suggested the use of a π^* energy window from the edge rise to the peak maximum, where the lifetime effect was ignored. It should be noted that in this work the reference spectrum was obtained from a polycrystalline graphitic carbon, which may have a similar lifetime broadening as the studied amorphous carbon materials. If a highly ordered graphite specimen is used as reference, there will be the same problem as in the Gaussian fitting method, which consequently overestimates the sp^2 % for amorphous carbon materials exhibiting extra lifetime-broadening effects.

In brief, to set the π^* energy window, there are two contradictory rules. Firstly, it is commonly preferred to choose an energy window much larger than the energy resolution. However, in practice this is impossible because of the relatively sharp π^* pre-peak and the erroneous lifetime-broadening effect. Secondly, in order to exclude the lifetime-broadening effect of the amorphous structure, only the maximum value should be used since it largely represents the basic feature of the π^* excitation (Titantah & Lamoen, 2004b). Due to the flexible setting of the two energy windows, especially for the I-ratio extraction in form of I_{π^*}/I_{σ^*}, a compromise between including the experimental broadening and largely excluding the lifetime broadening can be achieved. By centering the π^* energy window on the maximum intensity of the π^* pre-peak, we will essentially use the height of this peak. In order to take into account the experimental broadening effect, which is 0.6 – 0.7 eV in this work, we set the width of the π^* energy window to 0.7 eV, close to/slightly larger than the energy resolution. Afterwards, each boundary of this window was varied by ± 0.2 eV, which is a 0.4-eV-range slightly more than half of the energy resolution (0.3 – 0.35 eV), to check the standard deviation of the quantification results, which is a measure of the effectiveness of the compromise we have made. The results show that the standard deviation is 0.019 – 0.020 for the a-C:H sample, and is 0.009 (thick film region) and 0.015

(thin) for the ta-C sample. The higher standard deviation for the material with higher sp^2 % is in accordance with the stronger lifetime-broadening effect in such highly disordered carbon.

4.5.3 Choice of specific intensity-ratio formalism

The sp^2 % quantification results based on the three different formalisms are presented in Fig. 4.4.16, where a generally lower sp^2 % is observed if the $I_{\pi*}/I_{\pi*+\sigma*}$ is used as compared to $I_{\pi*}/I_{\sigma*}$, and the $I_{\pi*}/I_{\Delta E}$ I-ratio formalism gives the lowest sp^2 % among the three formalisms. More detailed, for one of the two extreme cases at the left end of the x-axis, where the studied C-material is pure in sp^3-C, the three formalisms all tend to give sp^2 % as 0. For the other extreme case at the right end of the x-axis, i.e. for the studied C-material containing 100 % of sp^2-C as given by the formalisms using $I_{\pi*}/I_{\sigma*}$, the $I_{\pi*}/I_{\pi*+\sigma*}$ formalism tends to give the fraction of sp^2-C of 100 % as well, but the sp^2 % obtained by $I_{\pi*}/I_{\Delta E}$ formalism is lower in this case. Earlier researchers, e.g. Bruley et al. (1995), regarded the formalisms $I_{\pi*}/I_{\Delta E}$ and $I_{\pi*}/I_{\sigma*}$ as alternative due to their equalization at these two extreme cases, which could not be true in practice.

There are two problems concerning the use of the $I_{\pi*}/I_{\Delta E}$ I-ratio formalism. Firstly, the setting of the large energy window encompassing both the π* and σ* peaks inevitably includes the intermediate energy-loss region, which has already been shown to cause errors in quantification. We have studied the detrimental influence of these energy losses by using the I-ratio in form of $I_{\pi*}/I_{\sigma*}$, i.e. in Fig. 4.4.9(c, d) and Fig. 4.4.14(c, d), the first sector of the quantification results show a slightly lower sp^2 % compared to the second sector. However, even the intermediate energy-loss region is omitted from the σ* energy window, which then gives the formalism using the I-ratio of $I_{\pi*}/I_{\pi*+\sigma*}$, the consequent sp^2 % are still lower than those by the $I_{\pi*}/I_{\sigma*}$, except the two extreme cases. Therefore, there is a second problem hidden in the formalism using the I-ratio of $I_{\pi*}/I_{\Delta E}$, which is that the partial cross-section ratio used in this formalism is dependent on the sp^2 % in the material, and is therefore not a constant but differs for the reference and the studied C-material with an unknown fraction of sp^2-C. By comparing the use of $I_{\pi*}/I_{\pi*+\sigma*}$, where the intermediate energy loss region is also avoided (the formalism proposed in section 4.4.9), to the use of $I_{\pi*}/I_{\sigma*}$, the effect of the non-constant partial cross-section ratio emerges. Although linear fitting shows also a good fit, the fitting with a parabola is even better and agrees well with the equality of these two formalisms when sp^2 % is 0 and 1, i.e. for pure diamond and graphite. And apparently, the results by using the $I_{\pi^*}/I_{\pi^*+\sigma^*}$ deviates from those obtained by the use of the I_{π^*}/I_{σ^*}-ratio the most as sp^2 % is ~ 50 %. Both these problems are contained in the use of $I_{\pi^*}/I_{\Delta E}$, whereas the use of $I_{\pi^*}/I_{\pi^*+\sigma^*}$ suffers only from the discrepancy between the partial cross-section ratios for the reference and the interested C-materials. It can be seen that the error caused by a not well-suited quantification formalism is more severe than that caused by including those intermediate signals into the σ^* integration window.

4.5.4 Influence of FIB milling on the determination of the sp^2/sp^3-ratio

The spectra (1) and (2) in Fig. 4.4.4 were recorded from HOPG specimens with almost the same crystallographic orientation. Therefore, the anisotropic property of graphite cannot be responsible for the difference in their *I*-ratios. Instead, the difference in the I_{π^*}/I_{σ^*} ratio can most likely be attributed to the different sample preparation techniques. The broadened and reduced π^* pre-peak of spectrum (2) implies that the Ga^+-ion milling could have damaged the surface regions of the specimen where the ordered crystal structure was amorphized. Hence, some of the C-atoms were transformed from sp^2-hybridization into sp^3 one. On the other hand, the crystallinity of graphite was largely kept perfect in the cleaved HOPG specimen. With respect to the difference visible between spectra (2) and (3), an angular effect due to the orientation difference as large as ~90° between them can be considered as reason. Also, this difference could be due to a thickness effect since the share of a FIB-induced damaged layer is less for a thick specimen and thus the *I*-ratio is higher, which is just the case for spectrum (3) compared to spectrum (2).

By assuming that the FIB-damaged layers are of the same thickness and that the original bond configuration was identical for the specimen of spectra (2) and (3), we applied the model suggested in section 4.2.2 and the *I*-ratio for the undamaged bulk R_b was derived. This *I*-ratio corrected for the FIB damage gets much closer to the *I*-ratio from spectrum (1), which is free of FIB damage, with a small difference of ~3 % compared to the original difference of 8 %/15 % for those from spectra (2)/(3). Therefore, it can be concluded that it was the FIB-induced damage that is responsible for the difference in *I*-ratios for spectra (1) – (3).

The damage-free spectrum labeled (1) in Fig. 4.4.4 is used as the reference (100 % sp^2-C) for quantification. Although, the model-derived I-ratio could be viewed as an average of EELS spectra acquired in perpendicular and parallel orientation to the graphite planes, which might seem better suitable as a quantification reference but contains several uncertainties. Firstly, for the two FIB-prepared HOPG specimens the assumptions of constant T_d and R_d in equation 4.9, which are the key assumptions in the model, were actually made based on two individual specimens with different crystallographic orientations. Although our FIB parameters are mostly identical, there could be anisotropic "hardness" seen by the Ga^+-ions resulting in a different thickness and bond configuration of the damaged layers. Secondly, the two specimens were tilted in TEM, which could have increased T along the incident direction of the electron beam by a factor of 0.4 – 1.5 % with respect to a tilting angle of 5 – 10°, but have no effect on R since the thickness share of a damaged layer would be unchanged by tilting. As a result, the data plotted on a ($1/T$, R) coordinate system could be left-shifted and consequently lead to an error in the intercept of the linear fitting result. Thirdly, the plasmon removal by deconvolution is generally considered less accurate for analyzed volumes with t/λ larger than 1.

The rightness of the magic-angle condition could be better than 3 %, which is the difference between the I-ratios from the spectrum (1) and the FIB damage-correction-model, considering the errors in the latter as discussed above for the anisotropic graphite.

For the a-C:H and ta-C films, a linear relationship between their sp^2 % and the reciprocal relative thickness is obvious, showing a good validation of the model. The data from the thick region of the ta-C specimen shows a stronger deviation from the linear fitting, possibly because of the error in plural scattering removal for t/λ exceeding 1. Although we have already considered this problem by excluding the plasmon intensity out of the σ^* integration window, it is clear that the plasmon intensities extend to a large range of energy loss and is difficult to be avoided completely in the energy window. Another factor affecting the fitting quality is that the specimen position of the low-loss spectrum measurement is not exactly the same as that for the recording of the C-K edge spectrum. The low-loss and the C-K edge spectra were recorded separately, and several experimental parameters have to be adjusted due to different acquisition efficiencies. As a result, specimen drift is possible during this process, and the measured thickness for a corresponding sp^2 % could contain an error, leading to a discrepancy for the linear fitting. More factors, such as local structure and thickness fluctuations for the bulk material and the damaged layer influence the fitting as well, e.g., an indication of the structure variation of ta-C film has already been shown in Fig. 4.4.11(a).

The results corrected for FIB damage give the true fractions of sp^2-C as 74.6 ± 1.4 % and 45.7 ± 1.3 % for the a-C:H and ta-C films, respectively. The fractions of sp^2-C in the a-C:H film are hardly influenced by the thickness as indicated by the nearly-zero slope, which could be attributed to two possibilities: the specimen contains no layer damaged by the FIB milling ($T_d = 0$) or the damaged a-C layer contains the same fraction of sp^2-C as the bulk ($R_d - R_b = 0$). The former possibility that the Ga^+-ions could have milled away the material directly without inducing a damaged layer is unlikely, because even for HOPG containing 100 % sp^2 bonding, FIB thinning along the graphite basal planes involves a phase transition as well. Therefore, given the small standard deviation (0.011) from the sp^2 % dataset of this a-C:H film, we could assume that this is a special amorphous carbon specimen containing the same sp^2 % as the FIB-induced amorphous carbon, which is ~ 75 %. Further assuming that this R_d ~ 75 % is transferrable to the ta-C specimen, the relative thickness of the damaged layer can be estimated from the slope of the model equation, which is 0.39, corresponding to a total thickness of ~ 40 nm and a damage depth of ~ 20 nm.

This model for the FIB-induced damage correction has a straightforward background since it is derived by simple mathematics. It is very beneficial because there could be hardly any physical error in it. However, a number of assumptions have to be made. The assumption of a damaged layer being homogeneous in both thickness and bond configuration, could be largely valid as seen from studies of FIB-induced damage of Si (Kato et al., 1999), where the crystal structure of the cross section of a FIB lamella was studied by TEM. However, this technique is not accessible for the amorphous carbon material, which is undistinguishable from the damaged layer. With respect to the bonding configuration of the damaged layer, to consider it to be transferrable from one amorphous carbon material (the a-C:H film) to another (the ta-C film) for estimating the damaged depth is a bold postulate and requires further studies.

4.5.5 Accuracy and precision of sp^2-quantification

It has generally been suggested that one should distinguish between precision and accuracy while discussing the confidence of a certain analysis technique like, e.g., STEM/EELS. The precision is given as the standard deviation of the results of a set of repeated experiments, whereas the accuracy corresponds to the true value measured as the deviation of the mean result of a set of experiments. A high precision contributes, but not necessarily correlates, to a high accuracy, and vice versa. However, lacking an exact true value, it is difficult to give the accuracy of ELNES quantification of sp^2-C. Since some of the experimental factors influence both the precision and the accuracy, it is difficult to give the precision and the accuracy separately.

In the following, we first list the factors that possibly cause errors in sp^2-C quantification.

TEM sample preparation could be a serious source of error. It has been shown that FIB-assisted sample preparation will induce layers with possibly different sp^2 % on both sides of the TEM lamella. These two damaged surface layers have a total thickness of ~ 40 nm, meaning they could have a large effect on spectra recorded from a thin sample with only several 10 nm overall thickness. It is even impossible to minimize the influence of this FIB damage by increasing of the TEM specimen thickness because, in that case, plural scattering effects would complicate STEM/EELS quantification. The model used for correcting the FIB-induced error is derived by simple mathematics; therefore, there could be hardly any physical error in the model. The rightness of this model largely relies on the assumption of a damaged layer being homogeneous with respect to both thickness and bond configuration.

During EELS spectrum acquisition, the alignment of the microscope, beam damage and contamination, any drift of the specimen as well as of the spectrometer, will affect the spectrum quality. For the different carbon materials under investigation, i.e. HOPG reference, DLC and diamond layers, beam damaging and contamination effects have been optimized by operating the microscope at 80 kV in the micro-probe mode (see discussion in subchapter 3.5). Drifts of the specimen and the spectrometer were indeed observed in some cases. Acquisition of a single C-K edge spectrum takes less than 1 min, where both specimen drift and spectrometer drift could be less of a problem. However, specimen drift may lead to different positions of acquisitions of a C-K edge spectrum and its corresponding low-loss spectrum, resulting in some error in plural scattering removal. In some cases, the instability of the spectrometer deteriorates the FWHM of the zero-loss peak from about 0.6 eV to 0.7 eV.

The EELS background extrapolation and subtraction (cf. section 3.4.2), which is done by fitting the background by a certain type of function, is usually valid for only a few 10 eV and, thus, could have a large uncertainty for energy losses higher than 100 eV. In general, it is the largest source of error in EELS quantification to determine element concentrations by two well separated ionization edges, but for two reasons this error could be much less serious for ELNES quantification of C-materials. For one thing, there is no strong excitation below the edge rise, and a window of 50 eV width can be conveniently positioned right in front of the edge onset to perform the fitting. One should only pay attention to the minor signals right in front of the C-K onset, which is assigned to dangling bond excitations, as well as energy losses of Ar-L_{23} edge, which could be present at ~ 40 eV in front of the C-K edge if Ar is contained in the sampled material (cf. section 3.4.1). The former could be easily excluded in the window for the background fitting, while the latter is not present for the two DLCs studied in this work. For the other, the π^* and σ^* components used for quantification are in close neighborhood, and the energy-loss range used for background extrapolation is less than 50 eV beyond the upper boundary of the background fitting window.

There are two ways to improve the efficiency of the removal of plural scattering by deconvolution for sp^2-C quantification using two-window method. The first one is the “the thinner the better” rule for a TEM specimen. This approach is generally applicable for t/λ below 1. (It is even unnecessary to do this procedure if the specimen is sufficiently thin). Alternatively, for a thick specimen, where the removal of plural scattering is necessary but difficult, one could avoid those dubious signals, which are induced by the inaccurate plural scattering removal process, by choosing an appropriate cut-off position of the σ^* energy window. The possible position and range of those dubious signals is analogous to those of the plasmon in the corresponding low-loss spectrum. This is useful as a thicker specimen is preferred, in order to reduce the influence of sample preparation damage, mainly induced by FIB milling.

With respect to the quantification methods, the systematic error caused by any uncertainty in the physics of ELNES quantification and the extraction of relevant signals is the most difficult to consider, due to the lack of true results. However, by studying the effects of energy-window variation (see sections 4.4.5 and 4.4.7), stable regions of quantification results are indeed present for the variation of the two boundaries of the σ^* window. Further, the setting of the two energy windows, which is correlated to the thickness effect, the overlapping area between the π* and the σ* excitations, and the C-H excitations, is discussed. Therefore, the efficiency of the two-window-method could be verified. We are now quite certain about the cause of different results given by different formalisms, and the use of the $I_{\pi*}/I_{\sigma*}$ intensity-ratio is more accurate than those of other formalisms. Additionally, the proper MAC was chosen, which yields deviations of only up to 3 % for $I_{\pi*}/I_{\sigma*}$ if the orientation of the crystalline HOPG reference samples is varied, as already discussed in sections 4.4.2 and 4.4.3.

The sp^2 % results from the a-C:H film could be used to gain a knowledge of the precision and accuracy of this ELNES quantification technique, where the effect of FIB-induced damage could be ignored due to the comparable C-atom bonding configuration within the damaged surface layers. The influence of specimen thickness could be visualized by comparing the quantification results from thick/thin specimen regions. The optimized setting of two energy windows (284.7 – 285.3 eV for π* and 292 – 307 eV for σ*) gives an sp^2 % value of 77.2 % with a standard deviation of ± 0.7 % from 8 C-K edge spectra taken from regions with t/λ (mean) = 0.46, whereas it amounts to (76.1 % ± 1.3) % for 5 spectra with t/λ (mean) = 0.73. Therefore, as the thickness increases from t/λ (mean) = 0.46 to 0.73, the precision is lowered from ± 0.7 % to ± 1.3 % and the accuracy gets worse as well. A lower mean sp^2 % from thick specimen regions (77.2 %) compared to that from thin specimen regions (76.3 %) indicates an underestimation due to the error in the plural scattering removal by deconvolution, which probably leads to remnant plural scattering intensity later-on erroneously included in the σ* energy window.

351 ELNES quantification results for 13 C-K edge spectra of the a-C:H film, obtained by diverse variations of the σ* window within the stable quantification range, yield a standard deviation of 1.7 %, which is a measure of multiple precision and accuracy factors concerning instrumental instabilities and treatment of the thickness effect as well as any unwanted signal included in each energy window, which is very important regarding the physical meaning of the two-window method. A systematic error due to the MAC veracity, being approximately 3 %, should be added into the consideration as well. Still unknown is the truth of the general assumption of the two-window method, which requires further systematic STEM/EELS investigations and corresponding studies of data processing.

5 Crystalline diamond films

This chapter presents the microstructural features of a crystalline diamond layer before and after tribological testing. This work was motived by the observation of low friction coefficients in diamond which are surprising on first sight considering the high hardness and strong bonding of the material. Two mechanisms were suggested in the literature as possible origins of the wear of diamond. The SEM, TEM and EELS/ELNES investigations presented in this chapter allow conclusions on the relevance of these mechanisms.

The chapter is subdivided into 5 subchapters. In addition to the subchapter 2.3 which describes some general aspects of diamond, the state of research on the tribological properties of diamond is reviewed in subchapter 5.1. Subchapter 5.2 gives details of the specimen fabrication and tribological testing conditions. The experimental results are presented in subchapter 5.3. Based on the experimental observations, the wear mechanism and the role of the tribo-induced a-C layer are discussed in subchapter 5.4.

5.1 Tribological properties of diamond: State of research

Diamond coatings produced by PECVD have been demonstrated as tribological coatings of high quality (Avigal et al., 1997; De Barros & Vandenbulcke, 2000; Skopp & Klaffke, 1998). Because of its high hardness, diamond can only get worn by polishing against diamond powder. It has been known for a long time that the wear of diamond is highly anisotropic, i.e. for certain crystallographic surfaces and polishing directions (Casey & Wilks, 1973; Grillo et al., 2000; Hird & Field, 2004). The origin of low COFs of diamond has been controversially discussed in literature up now. It has been attributed to either the passivation of dangling bonds or the transformation of sp^3-C at the surface into sp^2-hybridized C-atoms.

Ultralow COFs below 0.1 were observed during sliding in a water-vapor containing atmosphere (De Barros Bouchet et al., 2012; Manelli et al., 2010; Zilibotti et al.,

2009) and were attributed to the passivation of the strong σ dangling bonds at the surface in an environment containing chemically active species, for example, water vapor, H_2 or other H-/OH-containing molecules in the ambient atmosphere. In the study of De Barros Bouchet et al. (2012), high COFs between 0.6 – 1.0 were found in ultra-high vacuum (UHV), which were attributed to the direct contact of strong σ dangling bonds on both sliding surfaces. The COF was afterwards significantly reduced by introducing heavy water vapor (D_2O) or H_2 into the testing chamber, which was interpreted as the passivation of the dangling bonds at the diamond surface by D- and OD- ionic species in the case of D_2O, or H-atoms in the case of H_2. By tracing the ^2H-containing species using time-of-flight secondary-ion mass spectrometry (ToF-SIMS), it was revealed that the superficial carbon film indeed contains hydrogen and hydroxyl groups.

Alternatively, low COFs were also achieved for tests in dry inert gas atmosphere without any active species, where the mechanism of low friction was assigned to the formation of a layer containing sp^2-hybridized C-atoms (Miyoshi et al., 1998; Moras, Pastewka, Walter, et al., 2011; Pastewka et al., 2011). This process has been investigated by molecular dynamics simulations and the low wear resistance was attributed to the gradual destruction of the crystalline diamond surface, which leads to the formation of an amorphous interface layer. The transformation from crystalline diamond into the amorphous phase is shown to be mechanically driven, whereby a crystal atom is forced to get out of the potential well of its crystal position. During this process, there occurs a change of bonding configuration from pure sp^3-hybridization to a substantial fraction of sp^2- (60 %) and sp-hybridized (20 %) C-atoms (Moras, Pastewka, Walter, et al., 2011; Pastewka et al., 2011). These studies also offered an explanation for the anisotropic wear behavior of the diamond, giving “hard” and “soft” directions for a crystal C-atom according to its crystallographic environment. Indications for such a crystalline – amorphous phase transformation have been experimentally obtained. For example, Miyoshi et al. (1998) have found low COFs for tests of fine-/coarse-grain diamond films against a natural/CVD diamond pin in dry N_2 at relative humidities of less than 1 %. Parallel experiments in humid (~ 40 %) air were performed, where the COFs were either slightly lower than in dry N_2 (0.03 compared to 0.04), or ~ 3 times higher (0.08 compared to 0.03). In other words, the increased amount of the active species in the environment, such as O_2 or H-/OH- functional groups, doesn’t help reduce the COFs. On the other hand, an amorphous layer produced on fine-grain diamond film by carbon-ion implantation was found beneficial for reducing the COF in all kinds of environments. Moreover, debris produced by diamond/diamond friction tests in humid air were studied by van Bouwelen et al. (2003). The debris is characterized by a disordered graphite structure, with negligible content of oxygen.

There are diverse set-ups for tribological tests, with options of different counterparts and environment, as well as different tribometer geometries, e.g. pin-on-disk or twin-disk. Experiments carried out as diamond/diamond pairing are of prominent interest to study the wear mechanism of diamond. Some of the reports of such studies (De Barros Bouchet et al., 2012; Miyoshi et al., 1998; van Bouwelen et al., 2003) are summarized in Table 5.1. It can be seen that diamond films frictionally loaded by a diamond pin, show a high COF in UHV on the order of 0.1, and a low COF in the order of 0.01 in humid environment or in H_2, which is indicative of the mechanism of dangling bond passivation regardless of the film grain sizes. It is noteworthy that van Bouwelen et al. (2003) studied the polishing of single crystalline diamond against diamond powder and found a crystalline-amorphous phase transformation in the tribo-debris for a humid testing atmosphere. In an inert N_2 gas atmosphere, where active functional groups are absent, a low COF was also observed, which could be a result of the $sp^3 - sp^2$ phase transformation mechanism (De Barros Bouchet et al., 2012; Miyoshi et al., 1998).

Table 5.1 A brief summary of diamond/diamond pairing tribological studies in literature.

Counterpart I	Counterpart II	Environment	Stationary COF	Reference
Smooth NCD film	Pin coated with the same film	UHV	0.7	(De Barros Bouchet et al., 2012)
		H_20	0.05	
		H_2	0.01	
PECVD diamond film (20-100 nm)	Natural diamond pin	Air $_{\text{40 \% humidity}}$	0.03	(Miyoshi et al., 1998)
		N_2	0.04	
		UHV	1.0	
Diamond film (10 µm)	Pin fabricated out of the same diamond film	Air $_{\text{40 \% humidity}}$	0.08	
		N_2	0.03	
		UHV	0.6	
Single crystalline diamond	Scaife bonded with diamond powder	Air $_{\text{50 \% humidity}}$ (lubricated with silicone oil)	–	(van Bouwelen et al., 2003)

Some other factors have been reported to induce a crystalline – amorphous phase transformation. Tang et al. (2012) carried out tribological experiments on sintered polycrystalline diamond with µm-sized grains by pressing it onto a rotating disk containing Fe, Cr, Ni and Mn. A layer with a thickness of ~ 1 – 5µm containing Fe and Cr was detected on the diamond by FIB-processed cross-sectional secondary electron image and EDXS analysis. In a TEM investigation, an a-C layer with ~ 20 nm thickness was found directly on top of the diamond lattice. They attributed the phase transformation from diamond into amorphous carbon to high temperatures above 1000 °C during polishing combined with possible catalytic activity of transition metal impurities observed in the debris layer. The COF was not given in this study. However in other studies where a material transfer of the metal to the diamond counterpart occurs, the COFs are generally high. For example, Miyoshi and Buckley (1980), conducted pin-on-disk tribological tests on diamond {111} surfaces in the <110> direction (in vacuum, at room temperature) by varying the counterpart materials, including iron and tungsten and carried out EDXS measurements inside the wear tracks. All metals were found to be transferred to the diamond counterpart and the COFs around 0.5 were related to the relative chemical activity of those metals. Skopp and Klaffke (1998) performed sliding tests with a 100Cr6 ball on µm-grain-sized diamond film in air (dry/moist) at room temperature and a transfer layer of α-Fe_2O_3 with a thickness between 0.1 and 1 µm, occasionally 4 µm, was produced on the diamond, where the COF was as high as 0.6. In contrast, metal was not detected to be transferred to the wear track of diamond in work of Sharma et al. (2012) for a diamond (UNCD film)/steel (100Cr6 ball) test pairing (carbon was found to be transferred to the metal ball instead), a low COF was obtained.

Clear experimental evidence for the proposed mechanically driven phase transformation of diamond to amorphous carbon as the origin of wear is still lacking. For instance, Raman spectroscopy provides information about the sp^3/sp^2-ratio of carbon bonds on a micrometer scale and has been used for phase characterization in diamond films (Ferrari & Robertson, 2000; Gogotsi, Kailer, et al., 1998; Hird et al., 2007; Knight & White, 1989). However, previous experimental studies do not allow direct correlations between microstructure and hybridization of C-atoms on the nanometer scale. Efforts have been undertaken to perform TEM and EELS studies to get more insight into the processes which determine the wear resistance. These analytical techniques are the only ones which are suited to resolve the crystal structure and chemical bonding at one and the same position with nanometer resolution. The bonding configuration can often precisely be identified by analyzing the energy loss near-edge structure (ELNES) of ionization edges, i.e., the C-K ELNES for carbon (Egerton, 1996). An example is the work of Erdemir et al. (1997) who investigated debris particles collected from wear tracks formed under different tribological conditions and found sp^2-hybridized carbon by EELS/ELNES studies in a transmission electron microscope. However, firm conclusions would require a comparison of tribologically tested specimens from worn and unworn regions. Due to the high hardness of diamond and diamond-like carbon, TEM sample preparation is unfortunately very difficult, even though focused-ion-beam (FIB) instruments are now available for the preparation of TEM lamellae from such hard coatings at locations which can be selected with sub-micrometer precision (Giannuzzi et al., 2005). Using such site-selective FIB preparation and TEM, Tang et al. (2012) observed an amorphous carbon (a-C) layer containing sp^2-coordinated carbon on top of a polished diamond grain after dynamic friction polishing against a metal disk. These results are very instructive but not conclusive regarding the wear of diamond because of the metal counter surface which produces a chemically intermixed tribo-layer.

5.2 Specimen fabrication and tribological testing

Diamond films were deposited by microwave PECVD. SiC-rings were used as substrates which were first seeded by ultrasonication in an ethanol solution containing diamond powder (particles with sizes up to 300 nm). The diamond film was grown in a gas atmosphere consisting of 1.7 % CH_4 and 98.3 % H_2. The SiC-substrate was heated to 900 °C during the deposition. The hardness and Young's modulus of the resulting film were measured to be 9425 (±5 %) HV and 762 (±2 %) GPa, respectively. Ring-on-ring tribological tests at a speed of 4 m/s were performed in a nitrogen atmosphere under a global pressure of ~ 2 MPa. Both counterparts were coated with the same kind of diamond layer. The wear rate was 0.6 µm/h. Wear was confined to the polishing of the grain asperities. A wear track of 2 mm width with a shiny appearance was formed on the diamond surface. A friction coefficient of 0.15 was measured by the end of the test.

Microscopic studies were performed on the basis of one diamond film. Specimens for the TEM were prepared from regions inside and outside of the wear track.

5.3 Microstructure characterization by SEM, TEM and EELS/ELNES

5.3.1 Microstructure of the as-prepared diamond layer

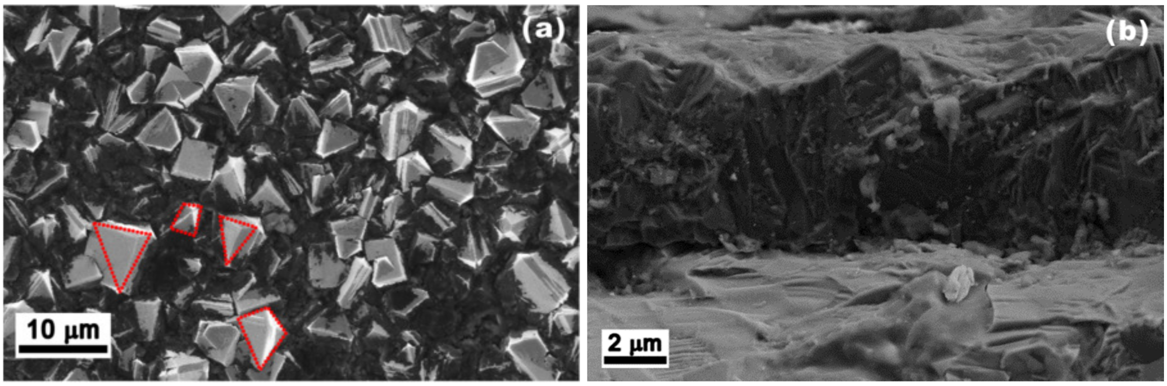

Fig. 5.3.1 SEM images from the unworn diamond layer: (a) plan-view image, (b) cross-section image.

The SEM images in Fig. 5.3.1 were obtained from outside the wear track of a tribologically tested specimen. It displays the unworn surface of the diamond layer. It is characterized by a rough topography with grains, which often exhibit pyramidal shapes with either a triangular base or a quadrangle base (as indicated by red dashed lines in Fig. 5.3.1(a)) and typical grain sizes in the µm-range. The cross-section SEM image (Fig. 5.3.1(b)) yields the thickness of the diamond film which varies between 4 µm and 7 µm due to its coarse-grained structure.

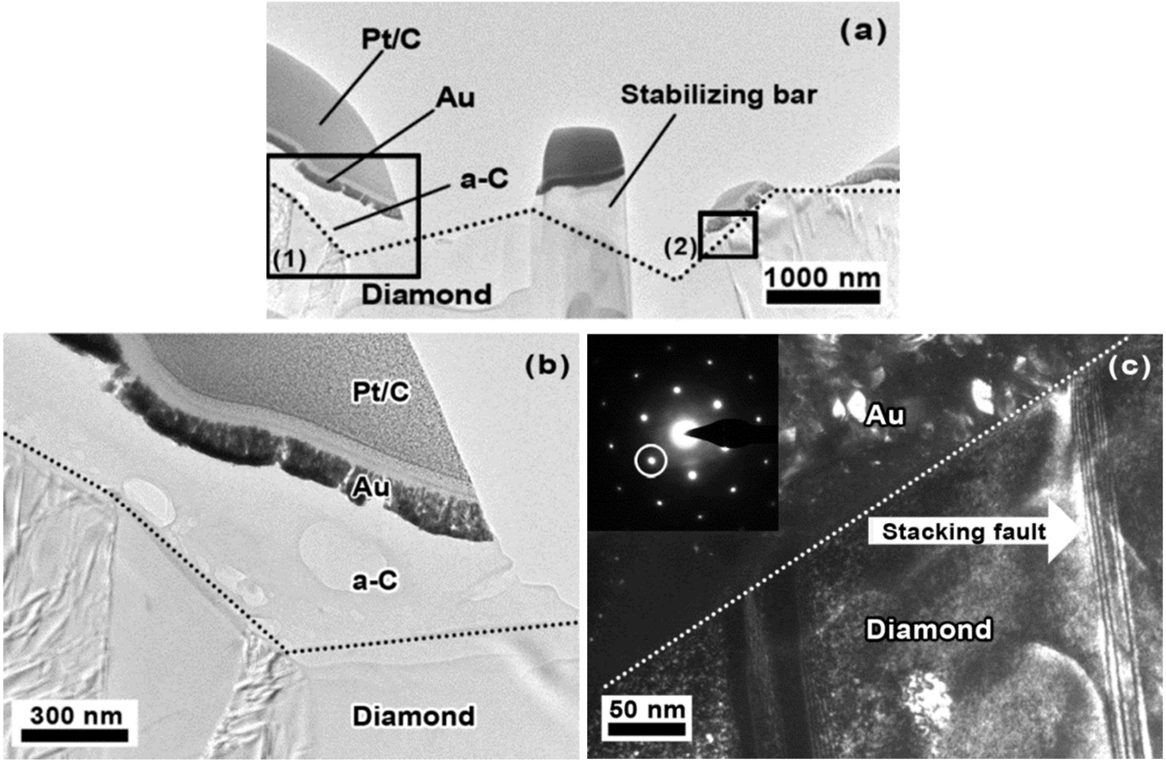

Fig. 5.3.2 Cross-section TEM images of the as-prepared diamond film. (a) overview of the FIB lamella with the original surface of the coating marked by a dashed line, (b) enlarged TEM image of the region marked by (1) in (a), (c) dark-field (DF) TEM image of the region marked by (2) in (a). The TEM DF image was taken with a $\{2\bar{2}0\}$ reflection as indicated by the [111] zone-axis pattern obtained by selected-area electron diffraction. The surface of the diamond layer is marked by a white dashed line.

Cross-section TEM images of a FIB lamella of the as-prepared diamond film are presented in Fig. 5.3.2. Fig. 5.3.2(a) shows an overview image of the lamella. For mechanical stabilization, the FIB lamella contains a bar with larger thickness in the center of Fig. 5.3.2(a). Material was inhomogeneously removed by the Ga^+-ion milling which can be inferred from the partial lack of the Au- and Pt/C-cover layers, which are still present in the regions marked by frames. Nevertheless, the original surface of the as-prepared diamond can be well traced and is indicated by the dashed line. It confirms the rough surface topography showing grains with pyramidal shape and sizes in the μm-range. The height of the pyramids may be actually larger because the cross-section was not necessarily taken through the center of the grains. Fig. 5.3.2(b) shows the region marked by frame (1) in more detail. The layer with the darkest contrast and a thickness of 100 nm is the gold layer, which marks the original surface of the as-prepared diamond film. The Pt/C-layer protection layer on top of the Au-layer exhibits a brighter contrast. The lower part of the image shows crystalline diamond. In addition, an a-C layer with a thickness of up to ~ 500 nm is observed between the Au-layer and the crystalline diamond. The a-C contains pores with a size of up to 300 nm which are attributed to inhomogeneous FIB milling in this thin specimen region. Fig. 5.3.2(c) shows a TEM dark-field (DF) image taken with a $\{2\bar{2}0\}$ reflection from the region marked by frame (2) in Fig. 5.3.2(a). Here, the a-C layer is missing as demonstrated by stacking faults reaching up to the nanocrystalline Au-layer (white arrow in Fig. 5.3.2(c)) which delineates the original surface of the diamond film (marked by a dashed line). The crystallinity of the diamond layer is confirmed by selected-area electron diffraction (SAED) (see SAED pattern in [111] zone-axis inset in Fig. 5.3.2(c)). It can be concluded from Fig. 5.3.2(b,c) that the as-deposited diamond layer is covered by a porous a-C layer with an inhomogeneous thickness. The layer can locally be absent (Fig. 5.3.2(c)) or may be up to ~ 500 nm thick as seen in Fig. 5.3.2(b).

5.3.2 Microstructure of diamond after tribological testing

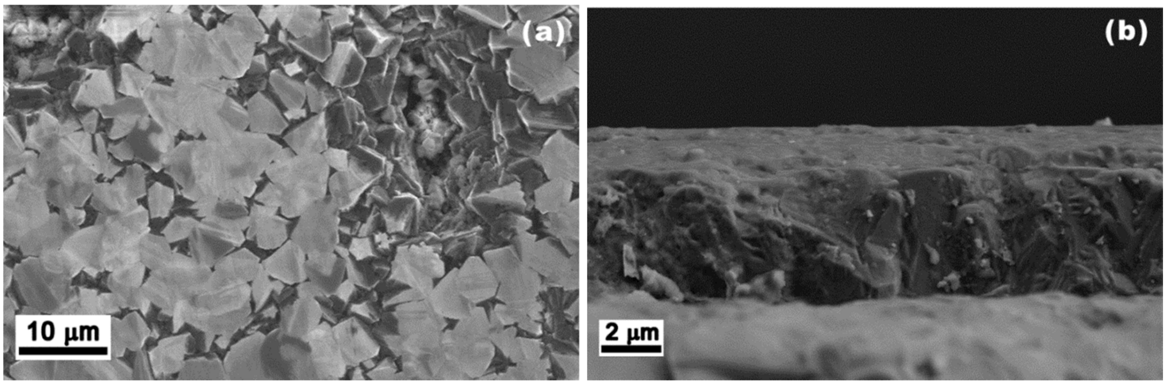

Fig. 5.3.3 SEM images of the diamond layer from the wear track: (a) plan-view image, (b) cross-section image.

Plan-view and cross-section SEM images of the diamond layer from the wear track are presented in Fig. 5.3.3. Comparison with the SEM images in Fig. 5.3.1 shows that tribological testing leads to the flattening of the surface. A significant amount of material was obviously removed. Cross-section SEM image (Fig. 5.3.3(b)) yields a remaining film thickness of ~ 4.5 µm in the wear track, which clearly shows that wear is confined to the grain asperities.

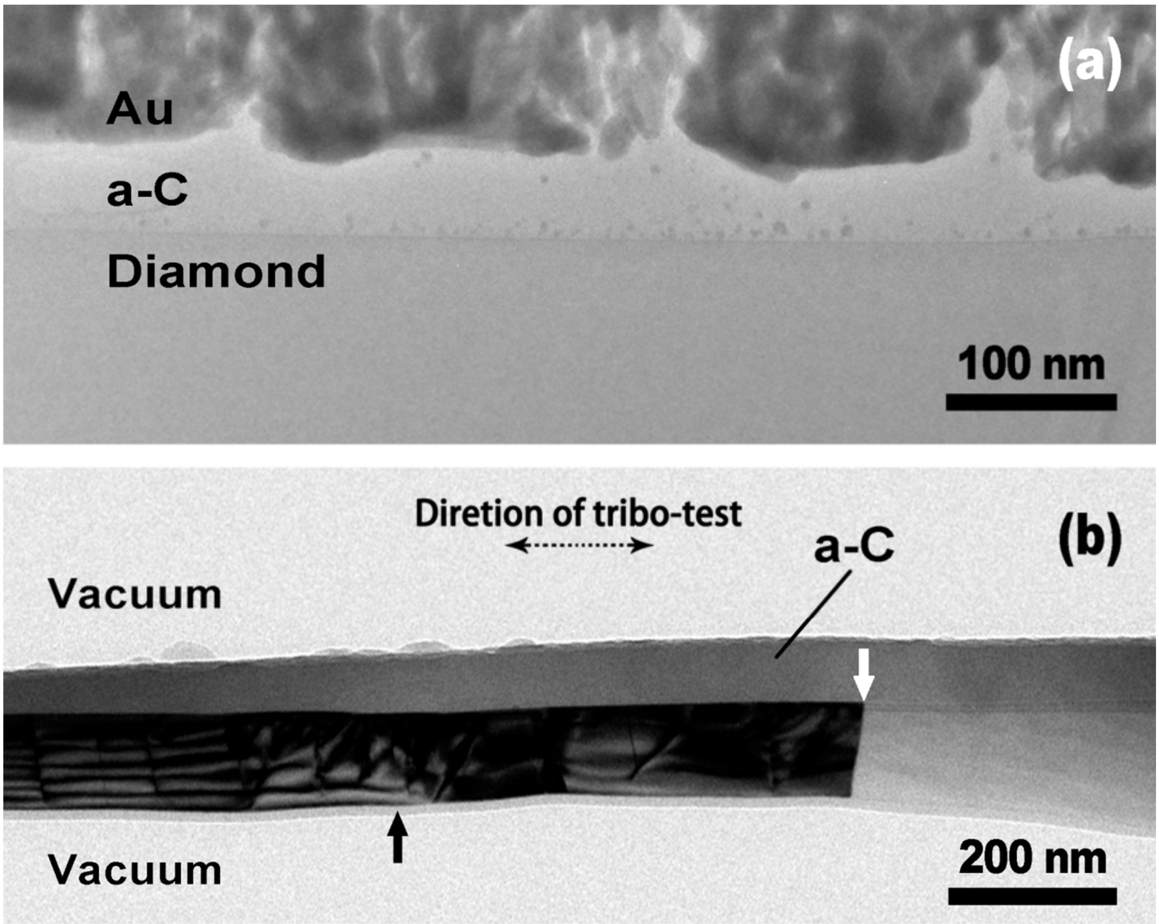

Fig. 5.3.4 Cross-section TEM images taken from the wear-track region. (a) overview TEM image of a FIB lamella, (b) overview TEM image of a conventionally prepared TEM sample.

Fig. 5.3.4 shows cross-section TEM images of the tribologically tested region. A TEM image of the lamella prepared by FIB milling is presented in Fig. 5.3.4(a). The image shows the crystalline diamond film, an a-C layer with a thickness of 30 nm to 50 nm and the Au-protection film with its darker contrast on top. The surface of the diamond film is rather flat as expected from the SEM images Fig. 5.3.4. To check for possible amorphization of the near-surface region of the crystalline diamond due to FIB preparation, a TEM specimen from the wear track could be successfully prepared by conventional techniques (as illustrated in Fig. 3.1.1). Here we claim that the specimen was prepared in a direction nearly along the tribological testing, as indicated in the image. The TEM image in Fig. 5.3.4(b) confirms the findings of the FIB-prepared sample. It shows a well adhering continuous a-C layer with a thickness between 40 nm and 80 nm on top of the crystalline diamond layer. We note that the lower part of the diamond layer was removed during Ar^+-ion milling. The effect of the amorphization by the Ar^+-ion milling can be well assessed at the lower edge of the TEM specimen marked by the black arrow. Only a narrow amorphous region with ~ 15 nm width can be recognized. The thin a-C layer induced by Ar^+-ion clearly demonstrates that the a-C layer on top of the diamond layer is not an artifact of the FIB sample preparation.

Two grains with different contrast are visible in Fig. 5.3.4(b). The grain with dark contrast is oriented close to a zone-axis orientation. Kinematic diffraction conditions without the effect of strong Bragg diffraction yield bright contrast in the other grain indicating a significant orientation difference between the two grains. Close inspection of the interface between the two grains (white arrow in Fig. 5.3.4(b)) reveals a step with a height of ~ 10 nm which effectively changes the thickness of the a-C layer on top.

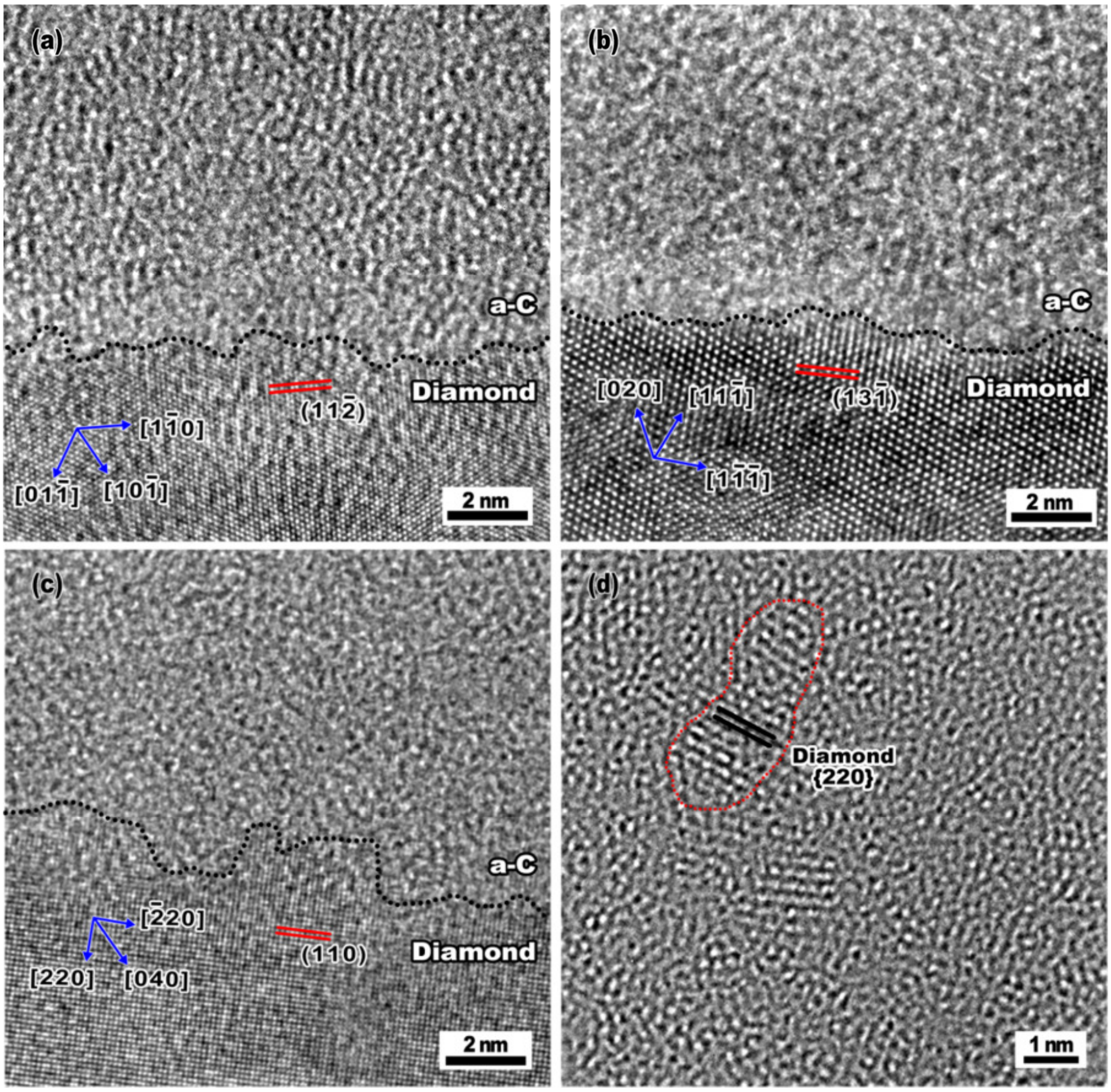

Fig. 5.3.5 HRTEM images of the interface regions between the crystalline diamond and the tribo-induced amorphous carbon layer with three different diamond grains oriented along the (a) [111] ZA, (b) [101] ZA, (c) [001] ZA. The approximate position of the interfaces is marked by dashed lines. (d) Crystalline diamond nanoparticle embedded in the a-C layer.

Fig. 5.3.5(a-c) show HRTEM images of the interface region between crystalline diamond and the a-C layer taken from the FIB-prepared sample. The diamond is oriented along the [111], [101], and [001] zone-axes, respectively. These three images show that the interface (indicated by dotted lines) is not atomically flat but exhibits a small-scale peak-to-peak roughness of ~ 1 nm on a lateral scale of a few 10 nm along the interface. On the lateral scale of typical TEM specimen thicknesses of several 10 nm, the roughness is in the same order (1-2 nm). The interfaces shown in Fig. 5.3.5(a-c) are oriented almost parallel to {121}, {131} and {110} lattice planes. HRTEM images of the a-C layer occasionally reveal crystalline diamond nanoparticles with sizes below 5 nm (Fig. 5.3.5(d)) which are embedded in the tribo-induced a-C layer.

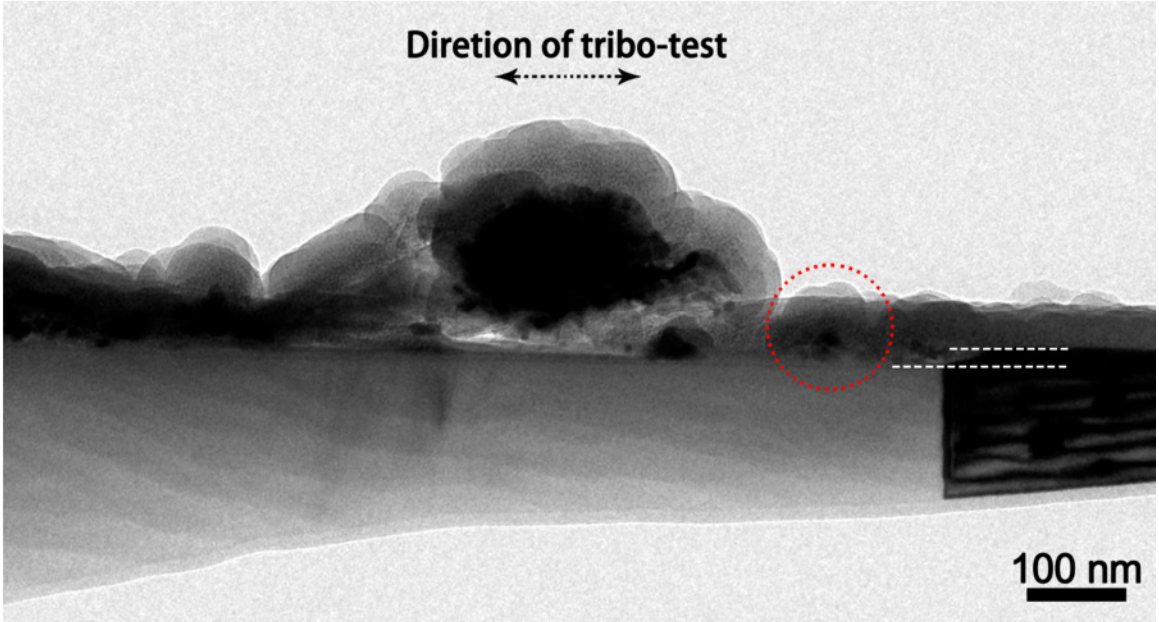

Fig. 5.3.6 Cross-section TEM image showing debris of different sizes formed after tribological testing.

Fig. 5.3.6 shows a cross-section TEM image from a conventionally prepared TEM specimen of the wear track, where a step of a height of ~ 20 nm of the a-C layer is also recognized at the grain boundary between the grains with bright and dark contrast (indicated by the white dashed lines). Similarly as the specimen in Fig. 5.3.4(b), the direction of the tribological testing is indicated in the image. The a-C layer in this region – especially on top of the bright grain – is not homogeneous anymore. In contrast to the other observed regions, the a-C layer shows complex contrast. In addition to the large particle in the middle, a few small and round ones of ~ 100 nm diameter are also recognized. Bumps on the surface of the a-C layer towards the right-hand side are indicative of other small debris particles. The grain of diamond film with dark contrast in this image is a continuation of the one on the left in Fig. 5.3.4(b), and it is noteworthy that such bumps become less towards the right-hand-side in Fig. 5.3.4(b). These particles are probably pieces of tribological debris and are unlikely artifacts of the conventional TEM sample preparation, because that the specimen was finally seen integrity without much disturbance. It is noted that the particles contain cores with dark contrast and are surrounded by layers with brighter contrast, e.g. the one indicated by the red dotted circle. The brighter layers which surround the crystalline cores are indicative of mass-thickness contrast for amorphous material. The dark contrast is an indication of either crystallinity due to Bragg diffraction analogous to dark contrast of the left grain in the diamond layer or amorphous region of a large thickness. The latter is here excluded for that the thickness needs to be extremely large for such a dark contrast.

5.3.3 Bond configuration by quantitative EELS

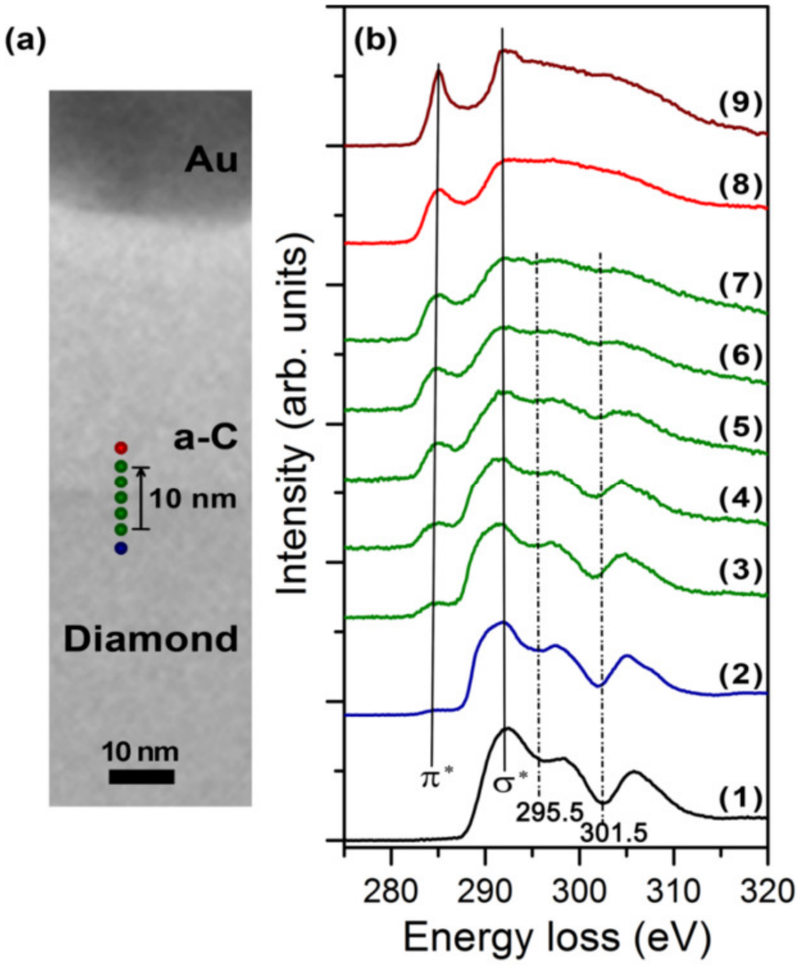

Fig. 5.3.7 (a) Cross-section TEM image of the transition region between crystalline diamond and the a-C layer with the direction of the EELS line-profile indicated. (b) EELS spectra of the C-K edge for (1) natural diamond, (2) – (8) line-profile EELS spectra across the interface between bulk diamond and the tribo-induced a-C layer, (9) reference spectrum recorded from HOPG.

Fig. 5.3.7 presents results of a combined TEM and EELS/ELNES analysis of the microstructure and bonding configuration of the C-atoms close to the interface between crystalline diamond and the tribo-induced a-C layer. Fig. 5.3.7(a) shows a cross-section TEM image with dots indicating the position of the EELS line-profile analysis across the diamond/a-C interface with the corresponding EELS spectra of the C-K ionization edge in Fig. 5.3.7(b). Spectrum (2) in Fig. 5.3.7(b) was taken in the bulk crystalline diamond. This spectrum can be compared with a reference spectrum (1) acquired from natural diamond which contain 100 % sp^3-C. Spectra (1) and (2) show the well-known ELNES signature of sp^3-C which consists of a peak at an energy loss ΔE of ~ 292 eV associated with σ* states and two dips at ~ 295.5 eV and ~ 301.5 eV (Hamon et al., 2004). We note a low-intensity pre-peak at ΔE = 285 eV which can be assigned to a small fraction of sp^2-hybridized C-atoms. This is deduced from a reference spectrum taken from 100 % sp^2-hybridized HOPG (spectrum (9) in Fig. 5.3.7(b)) which shows a pronounced pre-peak at ΔE = 285 eV resulting from π* states. The small π* pre-peak in spectrum (2) is attributed to the disordered surface layer superimposed on crystalline diamond due to TEM sample preparation.

Spectra (2) to (8) in Fig. 5.3.7(b) were taken in ~ 2 nm steps across a 10 nm interval between crystalline diamond and the a-C layer. A continuous rise of the π* pre-peak is observed which is characteristic for an increasing fraction of sp^2-hybridized C-atoms. Smoothing of the dips is another well-known feature of a-C (Berger et al., 1988; Berndt et al., 2004). Considering the effects of the 2.7 nm diameter, 1-2 nm interface roughness and possible slight inclination of the electron beam with respect to the interface, the true width of the transition layer in which the π* peak rises to its bulk value is likely to be below 5 nm. Spectrum (8) was taken in the a-C layer outside of the transition region. The pronounced π* peak indicates a high fraction of sp^2-hybridized C-atoms. The σ* peak is broadened and featureless due to the amorphous structure. The evaluation of the ratio of the π*/σ*-intensities with respect to the reference spectrum (9) yields a fraction of ~ 65 % sp^2-hybridized C-atoms, which is determined by the quantitative ELNES procedure discussed in Chapter 4.

We also note a more rounded onset of the σ* peak in spectrum (2) compared to the reference spectrum (1). The loss intensity between 287 eV and 290 eV could be assigned to the σ* state of C-H bonds. Hydrogen in amorphous carbon has been shown to lead to intensities in this energy-loss range in a study by X-ray absorption near-edge structure (Buijnsters et al., 2009). Hydrogen is indeed expected in diamond deposited by PECVD (Huran et al., 2012). The rounded onset of the σ* peak gradually decreases in spectra (3) to (6) and approaches the shape of the reference HOPG spectrum (9). This shows the reduction of the H-content in the tribo-induced C-layer, indicating a loss of hydrogen to the environment through free surfaces.

5.4 Discussion

The a-C layers observed on as-deposited and tribologically tested diamond differ significantly as far as thickness and morphology are concerned. The a-C layer with a thickness of up to several 100 nm on as-deposited diamond is attributed to the plasma deposition process. According to De Barros Bouchet et al. (2012) an a-C layer can indeed be present on the pristine diamond film as deposit from remnant precursor gas after the termination of the active PECVD process. For the tribologically tested region of the film, the SEM images (Fig. 5.3.3) and TEM images (Fig. 5.3.4 and Fig. 5.3.5) demonstrate that the µm-sized grains at the rough original diamond surface are almost completely flattened indicating that a significant amount of material must have been removed including the residual a-C layer from the deposition process. In contrast to the as-deposited a-C residue, the tribo-induced a-C layer is comparably uniform with a thickness below 100 nm.

Another question concerns the dependence of wear on the crystallographic orientation of the specimen surface. Seen from the topographic SEM images, this diamond film is composed of polycrystalline grains with random orientations: those diamond grains in shape of a triangular based pyramid are indicative of a crystallographic orientation close to <111>, whereas <100> grains are indicated by those square-based pyramids. Due to the large grain sizes of the polycrystalline diamond layer, only few grains and grain boundaries could be observed in the electron-transparent region of the TEM specimens which did not allow a statistically significant determination of the crystallographic orientation of the interface between the a-C layer and crystalline diamond. However, in the few cases, where this analysis was possible, we observe quite different interface orientations close to {112}, {113} or {110} planes. This suggests that different grains in the polycrystalline diamond layer may be characterized by different individual wear rate. With respect to the orientation dependence of wear, a few examples could be observed where the thickness of the a-C layer changes abruptly on grains with different crystallographic orientations (cf. Fig. 5.3.4(b) and Fig. 5.3.6). In one case, debris particles with sizes in the order of 100 nm and above were detected to be embedded in the a-C layer (Fig. 5.3.6). Another hint on the wear mechanism is provided by Fig. 5.3.5 which demonstrates that the interface between the crystalline diamond and the tribo-induced a-C layer is not crystallographically flat but displays a nm-scale roughness. Taking these observations together we can identify characteristics of the wear process of diamond.

Firstly, the wear process clearly involves the generation of a tribo-induced amorphous carbon layer. This carbon layer is softer than diamond with a high fraction of 65 % sp^2-coordinated carbon (cf. Fig. 5.3.7). This layer probably lubricates the contact which in turn correlates well with the rather low friction coefficient of diamond. The actual wear rate is then determined by two processes, the removal of the amorphous carbon layer and, of course, the growth rate of the amorphous carbon layer into the diamond. The removal of the amorphous carbon may proceed mechanically by plowing in front of diamond asperities (Pastewka et al., 2011), which results in the formation of wear debris, or by chemical etching with ambient oxygen (Moras, Pastewka, Gumbsch, et al., 2011; Moras, Pastewka, Walter, et al., 2011; Schade et al., 2006). The most essential process however is the growth of the amorphous phase into the crystalline diamond which must be interpreted as a mechanically driven phase transformation. The nm-scale roughness of the crystal-amorphous interface could also be compatible with the removal of small clusters from the crystal but most likely indicates an atom-by-atom amorphization process. Such an atomistic process in which the shearing of the softer amorphous phase over the interface occasionally removes an atom from the crystal is what is also observed in atomistic simulations (Pastewka et al., 2011; Pastewka et al., 2012).

Another very strong indication of such atom-by-atom phase transformation process is the different height of the amorphous layers above differently oriented grains as seen in Fig. 5.3.4(b). This observation directly suggests that the two crystals underneath the shearing amorphous layer must give in to the amorphization process with different ease. It indicates a crystallographic anisotropy of the rate of amorphization of the crystal at the interface. That wear rate of diamond is anisotropic and depends on the crystallographic orientation which has been known for some time by means of polishing single crystalline diamonds in specific orientations (Casey & Wilks, 1973; Grillo et al., 2000; Hird & Field, 2004) and has also been found in atomistic simulations (Pastewka et al., 2011). Tribological experiments with <100> and <111> fiber-textured diamond films show that the wear rate and COF differ for particular crystal planes with overall polishing orientations (Schade et al., 2006). All the previous observations clearly demonstrate a crystallographic anisotropy of wear in diamond but have to remain unspecific about the origin of this anisotropy. Our observation now directly demonstrates that it is the growth rate of the amorphous-crystalline interface which is different for different crystallographic directions.

In one region, debris particles with sizes of ~ 100 nm and above were observed (Fig. 5.3.6) indicating that another wear mechanism may exist in addition to the previously discussed atom-by-atom process. This is also suggested by Pastewka et al. (2011), who has simulated by molecular dynamics the wear rate of diamond on {111} surface to be extremely low and exceptionally different from the experimental results by 2 order of magnitude. Due to different grain orientations in the polycrystalline diamond layer it is indeed not surprising that grains with high wear resistance are present. Our observation shows that some diamond pieces could be fractured without phase transformation. And the crystalline-amorphous core-shell structure is indicative a phase transformation of the diamond fragments by further friction. Such a mechanism could occur on certain crystallographic diamond surface but resultant debris could be transported by a distance on to other grains during the friction. Another origin of the debris is the tribo-induced a-C layer, which was dynamically removed during the tribological test. Since the formation of the a-C layer has been verified to be predominant in this case, it is highly likely that debris of an amorphous structure could be formed in this way. As a result, the debris could be mixed together with those formed by diamond fragments during the friction.

We exclude that the homogeneous a-C layer is generally formed by the amorphization of fractured diamond pieces for the following reasons. A thickness change of the a-C layer was observed at grain boundaries which is not plausible if wear of fractured diamond pieces would be the origin of this layer. Moreover, the structure of the interface between crystalline diamond and the a-C layer is well compatible with an atom-by-atom process.

Diamond nanoparticles embedded in the a-C layer (Fig. 5.3.5(d)), which are also found in the amorphous layer, could come from an occasional breaking-off of diamond nanocrystals from the interface. However, this is regarded as rather unlikely given the different indications for an atom-by-atom transformation process. The diamond nanocrystals could also be remainders of larger fractured diamond pieces or they could be generated from within the amorphous phase in the tribological experiment. The observation of larger debris particles (Fig. 5.3.6) indeed indicates that nanoparticles could result from the wear of larger particles. Although we cannot clarify precisely the origin of the nanocrystals it is worth noting that such diamond nanoparticles were also observed by van Bouwelen et al. (2003) in the debris produced by polishing diamond.

Erdemir et al. (1997) carried out tribological tests on a smooth diamond surface sliding against a Si_3N_4 ball in a dry N_2-atmosphere, where the friction coefficient decreased from an initially high value of 0.6 to 0.04. This behavior was attributed to the transformation of debris particles into graphitic carbon. Erratic increase of the friction coefficient to high values was proposed to be caused by the removal of graphitic debris from the sliding interface. A similar mechanism was proposed by Hird et al. (2007). Tang et al. (2012) also observed a thin graphitic a-C layer on top of crystalline diamond after dynamic friction polishing against a metal wheel. They attributed the phase transformation from diamond into amorphous carbon to high temperatures above 1000°C during polishing combined with possible catalytic activity of transition metal impurities observed in the debris layer. In the present study, experimental conditions are such that even locally high temperatures above 1000°C are very unlikely and catalytic metallic components are not involved in the tribocontact. Consequently none of these can be responsible for the formation of the a-C layer.

The surrounding gas phase also plays an important role in the friction behavior of carbon (De Barros Bouchet et al., 2012). For example, water vapor, H_2, or other H-/OH-containing molecules in the ambient atmosphere can significantly reduce friction by passivation of the dangling bonds at the diamond surface (De Barros Bouchet et al., 2012). Tribological testing in our study was performed in a N_2-atmosphere, but a trace of O_2 or H_2O vapor cannot be completely excluded. Similarly, a small amount of hydrogen is expected to be released from the PECVD grown diamond as it amorphizes.

The bonding characteristics in the tribo-induced amorphous carbon layer is dominated by a content of 65 % sp^2-C according to our quantitative EELS results. With the high content of sp^2-hybridized C-atoms, it is plausible that the a-C acts as a lubricant layer and is responsible for the low COF of diamond. The amount of 65 % sp^2-C found here agrees well with the 60 % sp^2-C obtained in tribo-simulations (Pastewka et al., 2011). However, a gradual transition of the sp^2-content as found here has never been observed before and is also not seen in simulations. Its origin must therefore be investigated further.

While now the mechanically induced phase transformation of diamond to amorphous carbon is clearly identified as the main origin of wear and is tentatively linked with the low friction coefficient, it remains elusive how the rate of transformation may depend on experimental conditions and on environment or trace amounts of catalytic components. Further studies will have to investigate these rate effects more carefully and to which extent such phase transformations are a general phenomenon of solid lubrication.

6 Summary

This work is concerned with the characterization of microstructure and chemical-bonding phenomena of different carbon materials by means of combined TEM and STEM/EELS investigations. In detail, layers consisting of diamond-like carbon or polycrystalline diamond both deposited on steel substrates by PECVD, were intensely studied. Such studies are of importance to correlate microstructural and microchemical properties of C-materials on one side with their materials properties on the other. The sp^2/sp^3-ratio of carbon-based materials is of particular relevance for their tribological properties. In this context, a polycrystalline diamond layer was studied in this work before and after tribological testing where a phase transformation from crystalline diamond into amorphous carbon was theoretically predicted as main source of low friction coefficients along particular crystallographic directions.

As to diamond-like carbon, two different DLC films with amorphous structure, one hydrogenated sp^2-rich amorphous carbon (a-C:H) and the other tetrahedral amorphous carbon (ta-C) with different fractions of sp^2-C, were investigated. These materials with clearly different sp^2/sp^3-ratios of C-atoms were utilized to test and improve the quantification procedure for the fraction of sp^2-hybridized carbon. STEM/EELS analyses were performed on both DLC films and quantification of the sp^2/sp^3-ratios was performed by evaluating the contributions of the π^* and σ^* signal intensities to the C-K ELNES. Precise sp^2-C quantification could only be carried out by using an HOPG reference specimen, which is needed as a reference for the π^* and σ^* signal intensities and for determination of the magic-angle conditions (MAC) for STEM/EELS at 80 kV in the STEM microprobe mode. The latter, i.e. 80 keV primary energy and microprobe, were experimentally found to be of advantageous for reducing of contamination and electron-beam damage of the carbon materials under investigation. ELNES quantifications based on the C-K edge yielded an sp^2 content of approximately 75 % for the a-C:H sample, whereas sp^2 values between 52 and 70 % were found for the ta-C specimen as a function of specimen thickness. The latter behavior evidently hints to a damaging influence of FIB-based TEM specimen preparation on the quantified sp^2/sp^3-ratios.

It has been shown in this work that it is possible to correct the FIB-induced error in sp^2-quantification and roughly estimate the thickness and bond configuration of the FIB-induced damaged layer. The model itself is credible, which is a benefit of the simple mathematical deduction. However, several assumptions must be made, such as uniformity of the thickness and bond configuration of the FIB-induced damaged layer. Any local structural variation intrinsically contained in the specimen, and specimen drift during the acquisition of the C-K ELNES and low-loss spectra will also cause an error in using this model. The thickness of the damaged layer could be estimated as long as the bond configuration of the damaged C-layer can be derived. Applying this simple mathematic model of correcting the FIB-induced change of the sp^2/sp^3-ratio to the ta-C DLC specimen resulted in a true sp^2 content of 50 %, which is about 22 % lower than that of the a-C:H sample.

In addition, from a methodical point of view EELS processing was optimized to improve the accuracy of sp^2-C quantification. In more detail, to quantify the sp^2 content on the basis of the C-K ELNES the classical two-window method ($I_{\pi*}/I_{\sigma*}$) was used because of its advantages of a flexible signal selection and a more rigorous physical background (compared to the formalism using $I_{\pi*}/I_{\Delta E}$). The best positioning of the σ* energy-loss integration window was determined by fixing one of its boundaries, and varying the other. A range of energy-loss integration windows were identified giving stable quantification results for samples with high and low content of sp^2–hybridized carbon atoms which is valid for thin and thick specimen regions. Hence, the upper and lower boundaries of the σ* integration window should be positioned within this stable range as the first optimization.

The positioning of the π* energy window is a compromise between the lifetime broadening effect, which needs to be largely excluded in order to compare the reference spectrum from crystalline graphite, and the experimental broadening effect, which must be taken into account for instrumental instabilities. The energy window was centered on the maximum of the π* pre-peak with a small width slightly larger than the energy resolution. The quality of the choice of this window was evaluated by considering the standard deviation of the evaluated sp^2 content, and each of the two boundaries was varied over a range of half the energy resolution.

Errors contained in another widely-used formalism also based on the two-window method, which uses an intensity ratio in the form of $I_{\pi*}/I_{\Delta E}$, are now better understood. Although this formalism gives identical results for extreme cases (pure sp^2-hybridized C or pure sp^3-hybridized C), the errors are caused by extra signals in the intermediate energy loss region between the π* and σ* excitations included in the large energy window ΔE. In addition, the dependence of the partial cross-section ratio on the sp^2 content of the sampled material is ignored. The accuracy and precision of the C-K ELNES quantification of sp^2 contents is discussed, which is concluded to be better than 2 % concerning experimental instabilities regarding EELS acquisition and uncertainties in energy-window determination. The MAC applied in this work adds a contribution of ~ 3 % to the inaccuracy.

In the last chapter of the thesis, results are presented on the microstructure of a polycrystalline PECVD-deposited diamond film before and after tribological testing against a diamond film of the same type to analyze the origin of wear and low friction coefficients of diamond. The formation of an amorphous tribo-induced carbon layer with a rather homogenous thickness below 100 nm was clearly identified as the central mechanism of wear. The amorphous layer is formed by a mechanically induced phase transformation occurring at the interface between the diamond and the amorphous carbon layer. An interface roughness of ~ 1 nm indicates a crystalline-amorphous phase transformation that is induced by an atom-by-atom process. The abrupt thickness change of the amorphous carbon layer on top of grains with different crystallographic orientations demonstrates that the phase transformation process is highly anisotropic.

The tribo-induced amorphous carbon layer was found to contain a high fraction of 65 % sp^2-hybridized C-atoms which agrees well with the theoretically predicted value of 60 % sp^2-hybridzed C-atoms. The increase of the fraction of sp^2-hybridized C between crystalline diamond and the amorphous carbon layer occurs within a transition region of less than 5 nm thickness. Although the tribo-induced amorphous carbon layer clearly is one origin of wear in diamond, its general role as a solid lubricant for the measured friction coefficient remains elusive. Further studies are required to elucidate the dependence of the transformation rate on experimental conditions such as environment or trace amounts of catalytic components. The investigations will finally show to which extent such phase transformations are a general phenomenon of solid lubrication.

List of Figures

List of Tables

References

Aisenberg, S. (1971). Ion-beam deposition of thin films of diamondlike carbon. *Journal of Applied Physics, 42*(7), 2953. doi: 10.1063/1.1660654

Alexander, D. T. L., Anderson, J. R., Forró, L., & Crozier, P. A. (2008). The real carbon K-edge. *Microscopy and Microanalysis, 14*(S2). doi: 10.1017/s1431927608086509

Avigal, Y., Glozman, O., Etsion, I., Halperin, G., & Hoffman, A. (1997). [100]-textured diamond films for tribological applications. *Diamond and Related Materials, 6*(2-4), 381-385. doi: 10.1016/S0925-9635(96)00625-5

Banhart, F. (1999). Irradiation effects in carbon nanostructures. *Reports on Progress in Physics, 62*(8), 1181-1221. doi: 10.1088/0034-4885/62/8/201

Batson, P. E. (1993). Carbon 1*s* near-edge-absorption fine structure in graphite. *Physical Review B, 48*(4), 2608-2610. doi: 10.1103/PhysRevB.48.2608

Berger, S. D., Mckenzie, D. R., & Martin, P. J. (1988). EELS analysis of vacuum arc-deposited diamond-like films. *Philosophical Magazine Letters, 57*(6), 285-290. doi: 10.1080/09500838808214715

Berndt, F., Kleebe, H.-J., & Ziegler, G. (2004). Evidence for Structural Changes of Amorphous Carbon Coatings on Silicon Carbide During Tribological Tests. *Journal of the American Ceramic Society, 82*(11), 3161-3166. doi: 10.1111/j.1151-2916.1999.tb02218.x

Bernier, N., Bocquet, F., Allouche, A., Saikaly, W., Brosset, C., Thibault, J., & Charaï, A. (2008). A methodology to optimize the quantification of sp^2 carbon fraction from K edge EELS spectra. *Journal of Electron Spectroscopy and Related Phenomena, 164*(1-3), 34-43. doi: 10.1016/j.elspec.2008.04.006

Bertoni, G., & Verbeeck, J. (2008). Accuracy and precision in model based EELS quantification. *Ultramicroscopy, 108*(8), 782-790. doi: 10.1016/j.ultramic.2008.01.004

Bethge, H., & Heydenreich, J. (1987). *Electron Microscopy in Solid State Physics*. Netherlands: Elsevier.

Bhushan, B., Kellock, A. J., Cho, N. H., & Ager, J. W. (1992). Characterization of chemical bonding and physical characteristics of diamond-like amorphous-carbon and diamond films. *Journal of Materials Research, 7*(2), 404-410. doi: 10.1557/Jmr.1992.0404

Botton, G. A., Boothroyd, C. B., & Stobbs, W. M. (1995). Momentum dependent energy loss near edge structures using a CTEM: the reliability of the methods available. *Ultramicroscopy, 59*(1-4), 93-107. doi: 10.1016/0304-3991(95)00021-r

Bouchet, D., & Colliex, C. (2003). Experimental study of ELNES at grain boundaries in alumina: intergranular radiation damage effects on A1-L_{23} and O-K edges. *Ultramicroscopy, 96*(2), 139-152. doi: 10.1016/S0304-3991(02)00437-0

Bressler, P. R., Lubbe, M., Zahn, D. R. T., & Braun, W. (1997). X-ray absorption spectroscopy study of different solid carbon modifications. *Journal of Vacuum Science & Technology a-Vacuum Surfaces and Films, 15*(4), 2085-2087. doi: 10.1116/1.580613

Browning, N. D., Buban, J. P., Chi, M., Gipson, B., Herrera, M., Masiel, D. J., . . . Stahlberg, H. (2012). The application of scanning transmission electron microscopy (STEM) to the study of nanoscale systems. In T. Vogt, W. Dahmen & P. Binev (Eds.), *Modeling Nanoscale Imaging in Electron Microscopy* (pp. 11-40): Springer US.

Browning, N. D., Wallis, D. J., Nellist, P. D., & Pennycook, S. J. (1997). EELS in the STEM: determination of materials properties on the atomic scale. *Micron, 28*(5), 333-348. doi: 10.1016/s0968-4328(97)00033-4

Browning, N. D., Yuan, J., & Brown, L. M. (1991). Real-space determination of anisotropic electronic structure by electron energy loss spectroscopy. *Ultramicroscopy, 38*(3-4), 291-298. doi: 10.1016/0304-3991(91)90162-y

Bruley, J., Williams, D. B., Cuomo, J. J., & Pappas, D. P. (1995). Quantitative near-edge structure analysis of diamond-like carbon in the electron microscope using a two-window method. *Journal of Microscopy, 180*(1), 22-32. doi: 10.1111/j.1365-2818.1995.tb03653.x

Brydson, R. (2001). *Electron Energy-Loss Spectroscopy*: Garland Science.

Brydson, R., Sauer, H., Engel, W., & Zeitler, E. (1991). EELS as a fingerprint of the chemical coordination of light-elements. *Microscopy Microanalysis Microstructures, 2*(2-3), 159-169. doi: 10.1051/mmm:0199100202-3015900

Buckley, D. H. (1981). *Surface effects in adhesion, friction, wear, and lubrication*: Elsevier Science.

Buijnsters, J. G., Gago, R., Jiménez, I., Camero, M., Agulló-Rueda, F., & Gómez-Aleixandre, C. (2009). Hydrogen quantification in hydrogenated amorphous carbon films by infrared, Raman, and x-ray absorption near edge spectroscopies. *Journal of Applied Physics, 105*(9), 093510. doi: 10.1063/1.3103326

Bundy, F. P., Hall, H. T., Strong, H. M., & Wentorf, R. H. (1955). Man-made diamonds. *Nature, 176*(4471), 51-55. doi: 10.1038/176051a0

Casey, M., & Wilks, J. (1973). The friction of diamond sliding on polished cube faces of diamond. *Journal of Physics D: Applied Physics, 6*(15), 1772-1781. doi: 10.1088/0022-3727/6/15/303

Choudhary, D., & Bellare, J. (2000). Manufacture of gem quality diamonds: a review. *Ceramics International, 26*(1), 73-85. doi: 10.1016/S0272-8842(99)00022-X

Coffman, F. L., Cao, R., Pianetta, P. A., Kapoor, S., Kelly, M., & Terminello, L. J. (1996). Near-edge x-ray absorption of carbon materials for determining bond hybridization in mixed *sp*2/*sp*3 bonded materials. *Applied Physics Letters, 69*(4), 568. doi: 10.1063/1.117789

Cosslett, V. E. (1980). In M. T. (Ed.), *Electron Microscopy and Analysis* (pp. 277). Bristol.

Crewe, A. V., Isaacson, M., & Johnson, D. (1971). High resolution electron spectrometer for use in transmission scanning electron microscopy. *Review of Scientific Instruments, 42*(4), 411-&. doi: 10.1063/1.1685116

Cuomo, J. J., Doyle, J. P., Bruley, J., & Liu, J. C. (1991). Sputter deposition of dense diamond-like carbon films at low temperature. *Applied Physics Letters, 58*(5), 466-468. doi: 10.1063/1.104609

Daniels, H., Brown, A., Scott, A., Nichells, T., Rand, B., & Brydson, R. (2003). Experimental and theoretical evidence for the magic angle in transmission electron energy loss spectroscopy. *Ultramicroscopy, 96*(3-4), 523-534. doi: 10.1016/S0304-3991(03)00113-X

De Barros Bouchet, M. I., Zilibotti, G., Matta, C., Righi, M. C., Vandenbulcke, L., Vacher, B., & Martin, J. M. (2012). Friction of diamond in the presence of water vapor and hydrogen gas. Coupling gas-phase lubrication and first-principles studies. *Journal of Physical Chemistry C, 116*(12), 6966-6972. doi: 10.1021/Jp211322s

De Barros, M. I., & Vandenbulcke, L. (2000). Plasma-assisted chemical vapor deposition process for depositing smooth diamond coatings on titanium alloys at moderate temperature. *Diamond and Related Materials, 9*(11), 1862-1866. doi: 10.1016/S0925-9635(00)00335-6

Dienwiebel, M., Verhoeven, G. S., Pradeep, N., Frenken, J. W. M., Heimberg, J. A., & Zandbergen, H. W. (2004). Superlubricity of graphite. *Physical Review Letters, 92*(12), 4. doi: 10.1103/PhysRevLett.92.126101

Dieterle, L., Butz, B., & Mueller, E. (2011). Optimized Ar^+-ion milling procedure for TEM cross-section sample preparation. *Ultramicroscopy, 111*(11), 1636-1644. doi: 10.1016/j.ultramic.2011.08.014

Diociaiuti, M. (2005). Electron energy loss spectroscopy microanalysis and imaging in the transmission electron microscope: example of biological applications. *Journal of Electron Spectroscopy and Related Phenomena, 143*(2-3), 189-203. doi: 10.1016/j.elspec.2004.07.005

Donnet, C., Fontaine, J., Lefebvre, F., Grill, A., Patel, V., & Jahnes, C. (1999). Solid state ^{13}C and ^{1}H nuclear magnetic resonance investigations of hydrogenated amorphous carbon. *Journal of Applied Physics, 85*(6), 3264-3270. doi: 10.1063/1.369669

Donnet, C., Le Mogne, T., Ponsonnet, L., Belin, M., Grill, A., Patel, V., & Jahnes, C. (1998). The respective role of oxygen and water vapor on the tribology of hydrogenated diamond-like carbon coatings. *Tribology Letters, 4*(3-4), 259-265. doi: 10.1023/A:1019140213257

Egerton, R. F. (1996). *Electron Energy-Loss Spectroscopy in the Electron Microscope, 2nd ed.*. New York: Plenum Press.

Egerton, R. F. (2009). Electron energy-loss spectroscopy in the TEM. *Reports on Progress in Physics, 72*(1), 016502. doi: 10.1088/0034-4885/72/1/016502

Egerton, R. F., & Takeuchi, M. (1999). Radiation damage to fullerite (C_{60}) in the transmission electron microscope. *Applied Physics Letters, 75*(13), 1884. doi: 10.1063/1.124860

Enke, K., Dimigen, H., & Hubsch, H. (1980). Frictional-properties of diamond-like carbon layers. *Applied Physics Letters, 36*(4), 291-292. doi: 10.1063/1.91465

Erdemir, A. (2001). The role of hydrogen in tribological properties of diamond-like carbon films. *Surface & Coatings Technology, 146*, 292-297. doi: 10.1016/s0257-8972(01)01417-7

Erdemir, A., Donnet, C. (2001). Tribology of diamond, diamond-like carbon, and related films *Handbook of Modern Tribology* (pp. 871-899): CRC Press.

Erdemir, A., Eryilmaz, O. L., Nilufer, I. B., & Fenske, G. R. (2000). Synthesis of superlow-friction carbon films from highly hydrogenated methane plasmas. *Surface & Coatings Technology, 133*, 448-454. doi: 10.1016/s0257-8972(00)00968-3

Erdemir, A., Halter, M., Fenske, G. R., Zuiker, C., Csencsits, R., Krauss, A. R., & Gruen, D. M. (1997). Friction and wear mechanisms of smooth diamond films during sliding in air and dry nitrogen. *Tribology Transactions, 40*(4), 667-675. doi: 10.1080/10402009708983707

Erdemir, A., Nilufer, I. B., Eryilmaz, O. L., Beschliesser, M., & Fenske, G. R. (1999). Friction and wear performance of diamond-like carbon films grown in various source gas plasmas. *Surface & Coatings Technology, 120*, 589-593.

doi: 10.1016/s0257-8972(99)00444-2

Fallon, P., Veerasamy, V., Davis, C., Robertson, J., Amaratunga, G., Milne, W., & Koskinen, J. (1993). Properties of filtered-ion-beam-deposited diamondlike carbon as a function of ion energy. *Physical Review B, 48*(7), 4777-4782. doi: 10.1103/PhysRevB.48.4777

FEI-Company. (Version 1.0). *TITAN User's manual.*

Ferrari, A. C., Libassi, A., Tanner, B., Stolojan, V., Yuan, J., Brown, L., . . . Robertson, J. (2000). Density, *sp*^{3} fraction, and cross-sectional structure of amorphous carbon films determined by x-ray reflectivity and electron energy-loss spectroscopy. *Physical Review B, 62*(16), 11089-11103. doi: 10.1103/PhysRevB.62.11089

Ferrari, A. C., & Robertson, J. (2000). Interpretation of Raman spectra of disordered and amorphous carbon. *Physical Review B, 61*(20), 14095-14107. doi: 10.1103/PhysRevB.61.14095

Field, J. E. (1993). *Properties of diamond.* London: Academic Press.

Fink, J., Mullerheinzerling, T., Pfluger, J., Bubenzer, A., Koidl, P., & Crecelius, G. (1983). Structure and bonding of hydrocarbon plasma generated carbon-films - an electron-energy loss study. *Solid State Communications, 47*(9), 687-691. doi: 10.1016/0038-1098(83)90635-X

Gangopadhyay, A. K., Vassell, W. C., Tamor, M. A., & Willermet, P. A. (1994). Tribological behavior of amorphous hydrogenated carbon-films on silicon. *Journal of Tribology-Transactions of the Asme, 116*(3), 454-462. doi: 10.1115/1.2928865

Gass, M. H., Porter, A. E., Bendall, J. S., Muller, K., Skepper, J. N., Midgley, P. A., & Welland, M. (2010). Cs corrected STEM EELS: Analysing beam sensitive carbon nanomaterials in cellular structures. *Ultramicroscopy, 110*(8), 946-951. doi: 10.1016/j.ultramic.2009.11.005

Geim, A. K., & Novoselov, K. S. (2007). The rise of graphene. *Nature Materials, 6*(3), 183-191. doi: 10.1038/nmat1849

Giannuzzi, L. A. (2005). *Introduction to Focused Ion beams. Instrumentation, Theory, Techniques and Practice*: Springer.

Giannuzzi, L. A., Kempshall, B. W., & Schwarz, S. M. (2005). FIB lift-out specimen preparation techniques. In L. A. Giannuzzi & F. A. Stevie (Eds.), *Introduction to Focused Ion Beams* (pp. 201-228).

Gicquel, A., Hassouni, K., Silva, F., & Achard, J. (2001). CVD diamond films: from growth to applications. *Current Applied Physics, 1*(6), 479-496. doi: 10.1016/S1567-1739(01)00061-X

Gogotsi, Y. G., Kraft, T., Nickel, K. G., & Zvanut, M. E. (1998). Hydrothermal behavior of diamond. *Diamond and Related Materials, 7*(10), 1459-1465. doi: 10.1016/s0925-9635(98)00199-x

Gogotsi, Y. G., Kailer, A., & Nickel, K. G. (1998). Pressure-induced phase transformations in diamond. *Journal of Applied Physics, 84*(3), 1299-1304. doi: 10.1063/1.368198

Grillo, S. E., Field, J. E., & van Bouwelen, F. M. (2000). Diamond polishing: the dependency of friction and wear on load and crystal orientation. *Journal of Physics D: Applied Physics, 33*(8), 985-990. doi: 10.1088/0022-3727/33/8/315

Hamon, A. L., Verbeeck, J., Schryvers, D., Benedikt, J., & Van der Sanden, R. M. C. M. (2004). ELNES study of carbon K-edge spectra of plasma deposited carbon films. *Journal of Materials Chemistry, 14*(13), 2030-2035. doi: 10.1039/B406468m

Hauert, R. (2004). An overview on the tribological behavior of diamond-like carbon in technical and medical applications. *Tribology International, 37*(11-12), 991-1003. doi: 10.1016/j.triboint.2004.07.017

Hebert-Souche, C., Louf, P. H., Blaha, P., Nelheibel, M., Luitz, J., Schattschneider, P., . . . Jouffrey, B. (2000). The orientation-dependent simulation of ELNES. *Ultramicroscopy, 83*(1-2), 9-16. doi: 10.1016/s0304-3991(99)00168-0

Hebert, C., Jouffrey, B., & Schattschneider, P. (2004). Comment on "Experimental and theoretical evidence for the magic angle in transmission electron energy loss spectroscopy" by H. Daniels, A. Brown, A. Scott, T. Nichells, B. Rand and R. Brydson. *Ultramicroscopy, 101*(2-4), 271-273. doi: 10.1016/j.ultramic.2004.07.002

Hebert, C., Schattschneider, P., Franco, H., & Jouffrey, B. (2006). ELNES at magic angle conditions. *Ultramicroscopy, 106*(11-12), 1139-1143. doi: 10.1016/j.ultramic.2006.04.030

Hird, J. R., Bloomfield, M., & Hayward, I. P. (2007). Investigating the mechanisms of diamond polishing using Raman spectroscopy. *Philosophical Magazine, 87*(2), 267-280. doi: 10.1080/14786430600953772

Hird, J. R., & Field, J. E. (2004). Diamond polishing. *Proc. R. Soc. Lond. A, 460*(2052), 3547-3568. doi: 10.1098/rspa.2004.1339

Howe, J. M., & Oleshko, V. P. (2004). Application of valence electron energy-loss spectroscopy and plasmon energy mapping for determining material properties at the nanoscale. *Journal of Electron Microscopy, 53*(4), 339-351. doi: 10.1093/jmicro/dfh044

Huran, J., Balalykin, N. I., Shirkov, G. D., Boháček, P., Kobzev, A. P., Valovič, A., . . . Sekáčová, M. (2012). Characterization of nanocrystalline diamond/amorphous composite carbon films prepared by PECVD technology. *Physics Procedia, 32*(0), 875-879. doi: 10.1016/j.phpro.2012.03.650

Joly-Pottuz, L., Matta, C., Bouchet, M. I. D. B., Vacher, B., Martin, J. M., & Sagawa, T. (2007). Superlow friction of ta-C lubricated by glycerol: An electron energy loss spectroscopy study. *Journal of Applied Physics, 102*(6), 064912. doi: 10.1063/1.2779256

Jorissen, K. (2007). *The ab initio calculation of relativistic electron energy loss spectra.* (PhD), University of Antwerp, Belgium.

Jouffrey, B., Schattschneider, P., & Hebert, C. (2004). The magic angle: a solved mystery. *Ultramicroscopy, 102*(1), 61-66. doi: 10.1016/j.ultramic.2004.08.006

Joy, D. C., Romig, J. A. D., & Goldstein, J. I. (1986). *Principles of Analytical Electron Microscopy*. New York and London: Plenum Press.

Kato, N. I., Kohno, Y., & Saka, H. (1999). Side-wall damage in a transmission electron microscopy specimen of crystalline Si prepared by focused ion beam etching. *Journal of Vacuum Science & Technology a-Vacuum Surfaces and Films, 17*(4), 1201-1204. doi: 10.1116/1.581795

Kelly, B. T. (1981). *Physics of graphite*. London: Applied Science Publishers.

Knight, D. S., & White, W. B. (1989). Characterization of diamond films by Raman-spectroscopy. *Journal of Materials Research, 4*(2), 385-393. doi: 10.1557/Jmr.1989.0385

Kobashi, K. (2005). *Diamond Films*. Great Britain: Elsevier.

Koidl, P., Wild, C., Dischler, B., Wagner, J., & Ramsteiner, M. (1990). Plasma deposition, properties and structure of amorphous hydrogenated carbon films. *Materials Science Forum, 52-53*, 41-70. doi: 10.4028/www.scientific.net/MSF.52-53.41

Le Normand, F., Hommet, J., Szörényi, T., Fuchs, C., & Fogarassy, E. (2001). XPS study of pulsed laser deposited CN_x films. *Physical Review B, 64*(23), 235416.

Lebeau, J. M., & Stemmer, S. (2008). Experimental quantification of annular dark-field images in scanning transmission electron microscopy. *Ultramicroscopy, 108*(12), 1653-1658. doi: 10.1016/j.ultramic.2008.07.001

LiBassi, A., Ferrari, A. C., Stolojan, V., Tanner, B. K., Robertson, J., & Brown, L. M. (2000). Density, sp^3 content and internal layering of DLC films by X-ray reflectivity and electron energy loss spectroscopy. *Diamond and Related Materials, 9*(3-6), 771-776. doi: 10.1016/s0925-9635(99)00233-2

Lifshitz, Y. (1996). Hydrogen-free amorphous carbon films: Correlation between growth conditions and properties. *Diamond and Related Materials, 5*(3-5), 388-400. doi: 10.1016/0925-9635(95)00445-9

Manelli, O., Corni, S., & Righi, M. C. (2010). Water adsorption on native and hydrogenated diamond (001) surfaces. *Journal of Physical Chemistry C, 114*(15), 7045-7053. doi: 10.1021/Jp910971e

Mao, Z. Y., Zhu, Y. C., Gan, L., & Xu, F. F. (2014). Identification and quantification of varied valence Eu ions by photoluminescence spectrum and electron energy loss spectrum. *Journal of Luminescence, 148*, 334-337. doi: 10.1016/j.jlumin.2013.12.050

May, P. W. (2000). Diamond thin films: a 21st-century material. *Philosophical Transactions of the Royal Society A: Mathematical, Physical and Engineering Sciences, 358*(1766), 473-495. doi: 10.1098/rsta.2000.0542

McKenzie, D. R. (1996). Tetrahedral bonding in amorphous carbon. *Reports on Progress in Physics, 59*(12), 1611-1664. doi: 10.1088/0034-4885/59/12/002

Meier, S., König, M., & Hormann, C. (2007). Deposition of in situ surface structured DLC-coatings. *Surface and Coatings Technology, 202*(4–7), 1267-1271. doi: 10.1016/j.surfcoat.2007.07.058

Menon, N. K., & Yuan, J. (1998). Quantitative analysis of the effect of probe convergence on electron energy loss spectra of anisotropic materials. *Ultramicroscopy, 74*(1-2), 83-94. doi: 10.1016/S0304-3991(98)00029-1

Miyake, S., Takahashi, S., Watanabe, I., & Yoshihara, H. (1987). Friction and wear behavior of hard carbon-films. *Asle Transactions, 30*(1), 121-127.

Miyoshi, K., & Buckley, D. H. (1980). Adhesion and friction of single-crystal diamond in contact with transition-metals. *Applied Surface Science, 6*(2), 161-172. doi: 10.1016/0378-5963(80)90142-7

Miyoshi, K., Murakawa, M., Watanabe, S., Takeuchi, S., Miyake, S., & Wu, R. L. C. (1998). CVD diamond, DLC, and *c*-BN coatings for solid film lubrication. *Tribology Letters, 5*(2-3), 123-129. doi: 10.1023/A:1019133406413

Moras, G., Pastewka, L., Gumbsch, P., & Moseler, M. (2011). Formation and oxidation of linear carbon chains and their role in the wear of carbon materials. *Tribology Letters, 44*(3), 355-365. doi: 10.1007/s11249-011-9864-9

Moras, G., Pastewka, L., Walter, M., Schnagl, J., Gumbsch, P., & Moseler, M. (2011). Progressive shortening of sp-hybridized carbon chains through oxygen-induced cleavage. *Journal of Physical Chemistry C, 115*(50), 24653-24661. doi: 10.1021/Jp209198g

Muller, D. A., Singh, D. J., & Silcox, J. (1998). Connections between the electron-energy-loss spectra, the local electronic structure, and the physical properties of a material: A study of nickel aluminum alloys. *Physical Review B, 57*(14), 8181-8202. doi: 10.1103/PhysRevB.57.8181

Muller, D. A., Tzou, Y., Raj, R., & Silcox, J. (1993). Mapping sp(2) and sp(3) states of carbon at subnanometer spatial-resolution. *Nature, 366*(6457), 725-727. doi: 10.1038/366725a0

Muranaka, Y., Yamashita, H., Sato, K., & Miyadera, H. (1990). The role of hydrogen in diamond synthesis using a microwave plasma in a CO/H_2 system. *Journal of Applied Physics, 67*(10), 6247-6254. doi: 10.1063/1.345191

Palmer, D. W. (1994). In G. Davies (Ed.), *Growth and Properties of Diamond* (pp. 143). London.

Pappas, D. L., Saenger, K. L., Bruley, J., Krakow, W., Cuomo, J. J., Gu, T., & Collins, R. W. (1992). Pulsed laser deposition of diamond-like carbon-films. *Journal of Applied Physics, 71*(11), 5675-5684. doi: 10.1063/1.350501

Papworth, A., Kiely, C., Burden, A., Silva, S., & Amaratunga, G. (2000). Electron-energy-loss spectroscopy characterization of the sp2 bonding fraction within carbon thin films. *Physical Review B, 62*(19), 12628-12631. doi: 10.1103/PhysRevB.62.12628

Pastewka, L., Moser, S., Gumbsch, P., & Moseler, M. (2011). Anisotropic mechanical amorphization drives wear in diamond. *Nature Materials, 10*(1), 34-38. doi: 10.1038/nmat2902

Pastewka, L., Moser, S., Moseler, M., Blug, B., Meier, S., Hollstein, T., & Gumbsch, P. (2008). The running-in of amorphous hydrocarbon tribocoatings: a comparison between experiment and molecular dynamics simulations. *International Journal of Materials Research, 99*(10), 1136-1143. doi: 10.3139/146.101747

Pastewka, L., Mrovec, M., Moseler, M., & Gumbsch, P. (2012). Bond order potentials for fracture, wear, and plasticity. *MRS Bulletin, 37*(5), 493-503. doi: 10.1557/Mrs.2012.94

Pennycook, S. J., & Jesson, D. E. (1991). High-resolution Z-contrast imaging of crystals. *Ultramicroscopy, 37*(1-4), 14-38. doi: 10.1016/0304-3991(91)90004-P

Pharr, G. M., Callahan, D. L., McAdams, S. D., Tsui, T. Y., Anders, S., Anders, A., . . . Robertson, J. (1996). Hardness, elastic modulus, and structure of very hard carbon films produced by cathodic-arc deposition with substrate pulse biasing. *Applied Physics Letters, 68*(6), 779-781. doi: 10.1063/1.116530

Pickard, C. J., Payne, M. C., Brown, L. M., & Gibbs, M. N. (1995). *Ab initio* EELS with a plane wave basis set. In D. Cherns (Ed.), *Electron Microscopy and Analysis 1995* (Vol. 147, pp. 211-214). Bristol: Iop Publishing Ltd.

Racine, B., Ferrari, A. C., Morrison, N. A., I, H., Milne, W. I., & Robertson, J. (2001). Properties of amorphous carbon-silicon alloys deposited by a high plasma density source. *Journal of Applied Physics, 90*(10), 5002-5012. doi: 10.1063/1.1406966

Robertson, J. (2002). Diamond-like amorphous carbon. *Materials Science & Engineering R-Reports, 37*(4-6), 129-281. doi: 10.1016/S0927-796x(02)00005-0

Robertson, J., & O'Reilly, E. P. (1987). Electronic and atomic structure of amorphous carbon. *Phys Rev B Condens Matter, 35*(6), 2946-2957. doi: 10.1103/PhysRevB.35.2946

Rode, A. V., Gamaly, E. G., Christy, A. G., Gerald, J. G. F., Hyde, S. T., Elliman, R. G., . . . Giapintzakis, J. (2004). Unconventional magnetism in all-carbon nanofoam. *Physical Review B, 70*(5), 9. doi: 10.1103/PhysRevB.70.054407

Rossi, F., Andre, B., Vanveen, A., Mijnarends, P. E., Schut, H., Delplancke, M. P., . . . Abello, L. (1995). Diamond-like coatings - microstructural evolution under ion-beam assistance. *Journal de Physique IV, 5*(C1), 179-191. doi: 10.1051/Jp4:1995121

Saikubo, A., Yamada, N., Kanda, K., Matsui, S., Suzuki, T., Niihara, K., & Saitoh, H. (2008). Comprehensive classification of DLC films formed by various methods using NEXAFS measurement. *Diamond and Related Materials, 17*(7-10), 1743-1745. doi: 10.1016/j.diamond.2008.01.095

Savage, R. H. (1948). Graphite lubrication. *Journal of Applied Physics, 19*(1), 1-10. doi: 10.1063/1.1697867

Schade, A., Rosiwal, S. M., & Singer, R. F. (2006). Tribological behaviour of <100> and <111> fibre textured CVD diamond films under dry planar sliding contact. *Diamond and Related Materials, 15*(10), 1682-1688. doi: 10.1016/j.diamond.2006.02.008

Schlatter, M. (2002). DLC-based wear protection on magnetic storage media. *Diamond and Related Materials, 11*(10), 1781-1787. doi: 10.1016/s0925-9635(02)00166-8

Schmid, H. K. (1995). Phase identification in carbon and BN systems by EELS. *Microscopy Microanalysis Microstructures, 6*(1), 99-111. doi: 10.1051/Mmm:1995110

Schneider, R. (2011). Electron energy-loss spectroscopy (EELS) and energy-filtering transmission electron microscopy (EFTEM). In G. Friedbacher & H. Bubert (Eds.), *Surface and Thin Film Analysis*: Wiley-VCH.

Schwan, J., Ulrich, S., Roth, H., Ehrhardt, H., Silva, S. R. P., Robertson, J., . . . Brenn, R. (1996). Tetrahedral amorphous carbon films prepared by magnetron sputtering and dc ion plating. *Journal of Applied Physics, 79*(3), 1416. doi: 10.1063/1.360979

Schwander, M., & Partes, K. (2011). A review of diamond synthesis by CVD processes. *Diamond and Related Materials, 20*(9), 1287-1301. doi: 10.1016/j.diamond.2011.08.005

Sharma, N., Kumar, N., Dhara, S., Dash, S., Bahuguna, A., Kamruddin, M., . . . Raj, B. (2012). Tribological properties of ultra nanocrystalline diamond film-effect of sliding counterbodies. *Tribology International, 53*, 167-178. doi: 10.1016/j.triboint.2012.05.002

Sheeja, D., Tay, B. K., Shi, X., Lau, S. P., Daniel, C., Krishnan, S. M., & Nung, L. N. (2001). Mechanical and tribological characterization of diamond-like carbon coatings on orthopedic materials. *Diamond and Related Materials, 10*(3-7), 1043-1048. doi: 10.1016/s0925-9635(00)00413-1

Sigle, W. (2005). Analytical transmission electron microscopy. *Annual Review of Materials Research*, 35, 239-314. doi: 10.1146/annurev.matsci.35.102303.091623

Silvaf, S. R. P., Robertson, J., Rusli, Amaratunga, G. A. J., & Schwan, J. (1996). Structure and luminescence properties of an amorphous hydrogenated carbon. *Philosophical Magazine Part B, 74*(4), 369-386. doi: 10.1080/01418639608240341

Skopp, A., & Klaffke, D. (1998). Aspects of tribological testing of diamond coatings. *Surface & Coatings Technology, 98*(1-3), 1027-1037. doi: 10.1016/S0257-8972(97)00224-7

Spencer, E. G., Schmidt, P. H., Joy, D. C., & Sansalone, F. J. (1976). Ion-beam-deposited polycrystalline diamondlike films. *Applied Physics Letters, 29*(2), 118-120. doi: 10.1063/1.88963

Sumant, A. V., Krauss, A. R., Gruen, D. M., Auciello, O., Erdemir, A., Williams, M., . . . Adams, W. (2005). Ultrananocrystalline diamond film as a wear-resistant and protective coating for mechanical seal applications. *Tribology Transactions, 48*(1), 24-31. doi: 10.1080/05698190590893134

Sun, Y., & Yuan, J. (2005). Electron energy loss spectroscopy of core-electron excitation in anisotropic systems: Magic angle, magic orientation, and dichroism. *Physical Review B, 71*(12). doi: 10.1103/Physrevb.71.125109

Tamor, M. A., Vassell, W. C., & Carduner, K. R. (1991). Atomic constraint in hydrogenated diamond-like carbon. *Applied Physics Letters, 58*(6), 592-594. doi: 10.1063/1.104597

Tang, F. Z., Chen, Y. Q., & Zhang, L. C. (2012). Analysis of polished polycrystalline diamond using dual beam focused ion beam microscopy. *Philosophical Magazine, 92*(13), 1680-1690. doi: 10.1080/14786435.2012.657706

Thornton, J. A. (1983). Plasma-assisted deposition processes - theory, mechanisms and applications. *Thin Solid Films, 107*(1), 3-19. doi: 10.1016/0040-6090(83)90003-2

Thrower, P. A., & Mayer, R. M. (1978). Point-Defects and Self-Diffusion in Graphite. *Physica Status Solidi a-Applied Research, 47*(1), 11-37. doi: 10.1002/pssa.2210470102

Titantah, J. T., & Lamoen, D. (2004). Technique for the sp^2/sp^3 characterization of carbon materials: *Ab initio* calculation of near-edge structure in electron-energy-loss spectra. *Physical Review B, 70*(7). doi: 10.1103/PhysRevB.70.075115

Titantah, J. T., & Lamoen, D. (2005). sp^3/sp^2 characterization of carbon materials from first-principles calculations: X-ray photoelectron versus high energy electron energy-loss spectroscopy techniques. *Carbon, 43*(6), 1311-1316. doi: 10.1016/j.carbon.2005.01.002

Urbonaite, S., Wachtmeister, S., Mirguet, C., Coronel, E., Zou, W. Y., Csillag, S., & Svensson, G. (2007). EELS studies of carbide derived carbons. *Carbon, 45*(10), 2047-2053. doi: 10.1016/j.carbon.2007.05.022

Utsunomiya, S., Kogawa, M., Kamiishi, E., & Ewing, R. (2011). Scanning transmission electron microscopy and related techniques for research on actinide and radionuclide nanomaterials. In S. N. Kalmykov & M. A. Denecke (Eds.), *Actinide Nanoparticle Research* (pp. 33-62): Springer Berlin Heidelberg.

van Bouwelen, F. M., Field, J. E., & Brown, L. M. (2003). Electron microscopy analysis of debris produced during diamond polishing. *Philosophical Magazine, 83*(7), 839-855. doi: 10.1080/0141861021000055673

Verbeeck, J., & Bertoni, G. (2008). Model-based quantification of EELS: is standardless quantification possible? *Microchimica Acta, 161*(3-4), 439-443. doi: 10.1007/s00604-008-0948-7

Verbeeck, J., Van Aert, S., & Bertoni, G. (2006). Model-based quantification of EELS spectra: Including the fine structure. *Ultramicroscopy, 106*(11-12), 976-980. doi: 10.1016/j.ultramic.2006.05.006

Voevodin, A. A., Phelps, A. W., Zabinski, J. S., & Donley, M. S. (1996). Friction induced phase transformation of pulsed laser deposited diamond-like carbon. *Diamond and Related Materials, 5*(11), 1264-1269. doi: 10.1016/0925-9635(96)00538-9

Weiler, M., Sattel, S., Giessen, T., Jung, K., Ehrhardt, H., Veerasamy, V. S., & Robertson, J. (1996). Preparation and properties of highly tetrahedral hydrogenated amorphous carbon. *Physical review. B, Condensed matter, 53*(3), 1594-1608. doi: 10.1103/PhysRevB.53.1594

Williams, D. B., & Carter, C. B. (1996). *Transmission Electron Microscopy*. New York: Plenum Press.

Williams, O. A., Nesladek, M., Daenen, M., Michaelson, S., Hoffman, A., Osawa, E., . . . Jackman, R. B. (2008). Growth, electronic properties and applications of nanodiamond. *Diamond and Related Materials, 17*(7-10), 1080-1088.

doi: 10.1016/j.diamond.2008.01.103

Wu, M. H., Dai, J., & Zeng, X. C. (2012). *Ab Initio* computation based design of three-dimensional structures of carbon allotropes. *Progress in Chemistry, 24*(6), 1050-1057.

Xu, S., Tay, B. K., Tan, H. S., Zhong, L., Tu, Y. Q., Silva, S. R. P., & Milne, W. I. (1996). Properties of carbon ion deposited tetrahedral amorphous carbon films as a function of ion energy. *Journal of Applied Physics, 79*(9), 7234-7240. doi: 10.1063/1.361440

Yamamoto, K., Koga, Y., Fujiwara, S., Kokai, F., & Heimann, R. B. (1998). Dependence of the sp^3 bond fraction on the laser wavelength in thin carbon films prepared by pulsed laser deposition. *Applied Physics A: Materials Science & Processing, 66*(1), 115-117. doi: 10.1007/s003390050647

Yuan, J., & Brown, L. M. (2000). Investigation of atomic structures of diamond-like amorphous carbon by electron energy loss spectroscopy. *Micron, 31*(5), 515-525. doi: 10.1016/S0968-4328(99)00132-8

Yun, X. H., Bogy, D. B., & Bhatia, C. S. (1997). Tribochemical study of hydrogenated carbon coatings with different hydrogen content levels in ultra high vacuum. *Journal of Tribology-Transactions of the Asme, 119*(3), 437-442. doi: 10.1115/1.2833514

Zaidi, H., Lehuu, T., & Paulmier, D. (1994). Influence of hydrogen contained in hard carbon coatings on their tribological behavior. *Diamond and Related Materials, 3*(4-6), 787-790. doi: 10.1016/0925-9635(94)90270-4

Zhang, Y. F., Zang, C. Y., Ma, H. G., Zhongzhu, L. Z., Lin, Z., Li, S. S., & Jia, X. P. (2008). HPHT synthesis of large single crystal diamond doped with high nitrogen concentration. *Diamond and Related Materials, 17*(2), 209-211. doi: 10.1016/j.diamond.2007.12.018

Zilibotti, G., Righi, M. C., & Ferrario, M. (2009). *Ab initio* study on the surface chemistry and nanotribological properties of passivated diamond surfaces. *Physical Review B, 79*(7), 075420. doi: 10.1103/Physrevb.79.075420

Acknowledgements

Firstly, I would like to express my deep gratitude and appreciation to Prof. Dr. Dagmar Gerthsen. I have been always impressed for her responsiveness and supportiveness ever since I write to her for the first time searching for a position in LEM. Above all, many thanks for her guidance and advice throughout the work.

I appreciate very much Prof. Dr. Peter Gumbsch for providing the foundations and directions of this research, as well as those valuable discussions and comments, especially his expertise and excellent insight during the work regarding diamond wear.

My sincerest thanks are due to Dr. Reinhard Schneider, for helping me developing many necessary TEM skills and most importantly good research habits throughout the years. I appreciate very much his critical reading of this dissertation and fruitful discussions.

I am grateful to all the present and past Lemminge for a friendly atmosphere, especially Nadejda Firman, Dimitri Litvinov and Mr. Fotouhi, who gave me helpful introductions at the very first stage of my study, Erich Mueller and Simon Hettler for continuously helping me with the sample preparation, and Marina and Roman, extremely nice office neighbors. I am thankful to Sven Meier and Manuel Mee for their help in producing and delivering the samples for my work and fruitful discussions with them.

Many thanks to Mrs. Sauter and Mrs. Doer for helping me with paperwork and other stuff.

I am thankful to Prof. Dong and Mrs. Li, who supervised my master thesis and encouraged me to pursue a PhD. The support and encouragement I have had from them is of great importance to me.

Last but not least, I would like to thank all my friends, for the wonderful time we had. I will bear you in my mind.

最后，衷心感谢我的父母，感谢他们给我的无尽的爱与支持。